HYDROGEN STORAGE BY CARBON NANOTUBES

HYDROGEN STORAGE BY CARBON NANOTUBES

By

JEREMY LAWRENCE, B.ENG.

A Thesis

Submitted to the School of Graduate Studies

In Partial Fulfillment of the Requirements

For the Degree

Master of Applied Science

McMaster University

MASTER OF APPLIED SCIENCE (2002) McMaster University

(Materials Science and Engineering) Hamilton, Ontario

TITLE:	Hydrogen Storage by Carbon Nanotubes
AUTHOR:	Jeremy Lawrence, B. Eng. (McMaster University)
SUPERVISOR:	Professor Gu Xu
NUMBER OF PAGES:	xiii, 153

Abstract

Safe, lightweight, and cost-effective materials are required to practically store hydrogen for use in portable fuel cell applications. Compressed hydrogen and on-board hydrocarbon reforming present certain advantages, but their limitations must ultimately render them insufficient. Storage in hydrides and adsorption systems show promise in modeling and experimentation, but a practical medium remains unavailable.

Since the earliest report of adsorption on single-walled carbon nanotubes (SWNT) in 1997, a number of controversial publications have claimed the hydrogen capacity of these materials to be between 0.1 to 10 wt. %. However, no study has yet demonstrated a plateau of adsorption with pressure that would verify the reported capacity.

A volumetric adsorption measurement instrument was designed and constructed to resolve this controversy. The instrument is capable of degassing samples under high vacuum and offers unprecedented measurements of hydrogen storage up to a pressure of 300 atm and a broad range of temperatures. In addition, an electrical probe within the sample cell was designed to study the mechanism of adsorption *in situ*.

The best hydrogen storage observed on bundles of purified SWNT was 1.6 wt. % at 264 atm and 200 K. At room temperature, a high-pressure plateau was

found corresponding to an adsorption of 0.9 wt. % at a pressure of 300 atm, which equates to an adsorption to surface area ratio of 1.14 wt. %/1000 m^2/g.

Contrary to the claim by the Caltech Group [Ye et al., 1999], resistance measurements of purified SWNT bundles revealed that bundles do not separate under high pressure. Instead, the bundles were found to compress under the action of external pressure, leading to an increase in conductivity with pressure. A simple geometrical model suggests that without this bundle separation the volume displaced by the sample may counteract the benefit gained by adsorption because of the increase in gas density at high pressure.

The isosteric heat of adsorption on SWNT bundles was measured to be between 3.9 and 5.0 kJ/mol at low levels of adsorption, and the activation energy for adsorption determined by the Langmuir model was found to be 1.9 kJ/mol. These low energy parameters are indicative of weak physisorption.

Acknowledgments

I would like to express my gratitude to Professor Gu Xu of McMaster University for his supervision and inspiration over the course of this project. His enthusiasm and enduring patience were invaluable in making this work possible.

I would also like to thank Paul Gatt and Wen-Jun Wang of the Department of Chemical Engineering and Jim Garrett of the Brockhouse Institute for Materials Research for their technical advice and assistance.

Table of Contents

List of Figures

List of Tables

1.0 Introduction

Amid urban smog, contaminated water and an ever increasing endangered species list that have come to characterize contemporary industrialized society, it is clear that the environment has, until recently, been taken for granted. For human civilization to continue it is overwhelmingly clear now more than ever that modern lifestyle and industry must be altered to allow for a sustained environment. Fortunately, the scientific community is responding vigorously to the challenge, and solutions are being developed and discoveries are being made that will allow many familiar conveniences and necessities to be maintained. Principal among these necessities is the continued use and development of the transportation network. Traditionally, transportation has been heavily reliant upon the burning of fossil fuels as the means to generate portable power supplies. However, the burning of fossil fuels is a well known source of a variety of pollutants that are invading our environment by poisoning our air and warming our climate. It is therefore important that the use of fossil fuels be replaced by a more environmentally benign fuel source without impairing the transportation network.

The development of the fuel cell has opened up the possibility of generating the much needed power requirements, whether portable or stationary, with little or no threat to the environment. Furthermore, there exists a possibility

for the fuel cell to be powered entirely by the most abundant element in the universe: hydrogen. Hydrogen storage has therefore become the focal point of fuel cell research in the last 5-6 years. The main problem is the low density of hydrogen, requiring large storage vessels to contain a useful quantity of fuel. A number of alternative methods of improving the storage have been developed in recent years, including liquid hydrogen, metal hydrides, and chemical compounds. A new material referred to as carbon nanotubes has shown promise as a hydrogen adsorbent, but the mechanism and storage capacity is controversial and not well understood.

1.1 Hydrogen as a Fuel

A schematic diagram of a hydrogen-powered fuel cell is depicted in Figure 1-1. A simple fuel cell is composed of an electrolyte material sandwiched between two electrodes. Electrochemists and others familiar with the process of electroplating will recognize the fuel cell as a form of electrochemical cell. The electrolyte is a material that is capable of conducting ionically, such that as ionic charge is transferred from one electrode to the other through the electrolyte it is neutralized by electronic charge passing through an external resistive load. It is this electronic charge transfer that provides useful energy. A variety of fuel cells are possible, operating on a variety of fuels, and conducting a variety of ions. The one that has captured the imagination of environmentalists, and more recently industrialists, however, is the low-temperature hydrogen fuel cell. In this type of

cell, the electrolyte is composed of a solid material that is able to conduct protons. In operation, hydrogen fuel is supplied to the anode, and oxygen or air is supplied to the cathode. The hydrogen molecule splits into two protons, and two electrons- the protons passing through the electrolyte, and the electrons passing through the external circuit. At the anode, the incoming protons combine with oxygen to form harmless water, and thermal losses. The two half-cell reactions

$$\tfrac{1}{2}\, H_{2\,(g)} = 2H^{+} + 2e^{-} \qquad 1.1$$

$$O_{2\,(g)} + 2e^{-} = 2O^{2-} \qquad 1.2$$

combine to form the cell reaction

$$\tfrac{1}{2}\, H_{2\,(g)} + O_{2\,(g)} = H_2O_{(g)\text{ or }(l)} \qquad 1.3$$

The cell reaction describes the thermodynamic driving force for the reaction. The free energy change for the cell reaction for reactants and products in standard states at 25°C and 1 atm pressure is -150 kJ/mol.

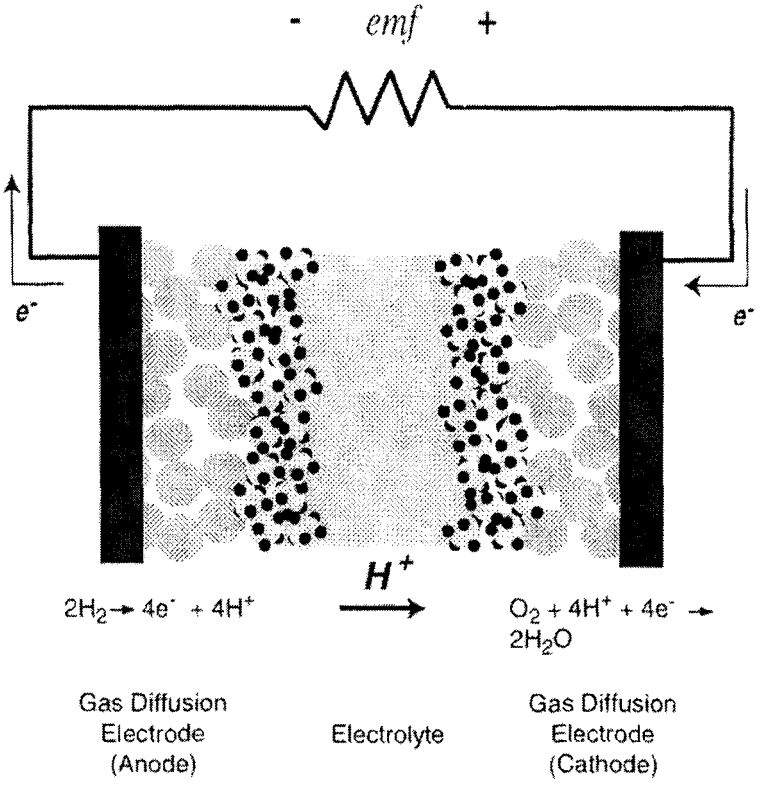

Figure 1-1 Proton Exchange Membrane (PEM) fuel cell.

An alternative to hydrogen fuel cells is the so-called direct methanol fuel cell. Instead of reforming the methanol to supply hydrogen to the fuel cell anode, the methanol molecule is broken down by unique catalysts at the anode surface. A disadvantage of this process is the generation of a waste product of CO_2, and to a lesser extent, CO. The presence of CO at the fuel cell electrode is detrimental to the operation of the fuel cell even in minute quantities, as CO adsorbs strongly to the surface of platinum catalyst. As a result, the direct methanol fuel cell must be operated at a slightly higher temperature than hydrogen fuel cells in a regime in which adsorbed CO is unstable. Higher operating temperatures are not only

inconvenient and inefficient, but also at this temperature, NO_X is produced from nitrogen in the air supplied to the anode. Furthermore, it remains that the waste generated and the fact that methanol is derived from fossil fuels detracts from inherent advantages of the fuel cell. The energy available from the direct methanol fuel cell is only 17 % by mass of that available from hydrogen [Larminie and Dicks, 2000]. Proponents of this system point out that methanol can be stored at densities greater than hydrogen, and a distribution network already exists.

It is possible to supply hydrogen to the fuel cell in a variety of chemical forms. Table 1-1 compares various sources of hydrogen in terms of the potential energy available, the specific energy of each fuel, and the volumetric energy of each fuel. The enormous potential energy stored in hydrogen by mass and the fact that its combustion produces only water, it is clear why hydrogen is the fuel of choice. However, this data also demonstrates hydrogen's shortcoming: volumetric energy storage.

Expressed in another way, the fuel tank of a typical gasoline-powered automobile has a volume of 50 liters, and a mass at full capacity of approximately 48 kg. Assuming a feasible fuel utilization efficiency of 65%, a fuel cell powered vehicle consumes 3.1 kg of hydrogen for a 500 km range. A 50 liter volume of hydrogen, compressed to a pressure of a typical laboratory cylinder or 150 atm would have a mass of only 0.62 kg, thereby providing a range of only 100 km.

This is clearly unacceptable, especially considering the safety hazard associated with carrying highly compressed gas.

Fuel	Hydrogen weight fraction	Ambient state	Mass energy density (MJ/kg)	Liquid vol. energy density (MJ/liter)
Hydrogen	1	Gas	120*	8.4-10.4
Methane	0.25	Gas	50	21
Ethane	0.2	Gas	47.5	23.7
Propane	0.18	Gas	46.4	22.8
Gasoline	0.16	Liquid	44.4	31.1
Ethanol	0.13	Liquid	26.8	21.2
Methanol	0.12	Liquid	19.9	15.8

Table 1-1 Properties of various alternative fuel sources for hydrogen fuel cells. $^{*}\ H_2 + 1/2O_2 \rightarrow H_2O$ *(steam)* $\Delta H = -241$ *kJ/mole*

1.2 Challenges of Hydrogen Storage

For hydrogen to become a competitive fuel, it is clear from the discussion in the preceding section that advances will need to be made in getting more hydrogen into a smaller volume without overly increasing the overall mass of the storage system. There are a variety of methods of quantifying hydrogen storage, several of which are prevalent in the literature. Volume of hydrogen at STP per kilogram of storage is commonly used for comparing a variety of different types of storage systems. A variation of this is a ratio of mass of hydrogen to mass of overall storage system converted to a percent. The latter "weight percent" method is particularly advantageous as it eliminates the need for cumbersome calculations

to provide an adequate evaluation of a storage system. Another method commonly used to quantify hydrogen storage on carbon materials is the hydrogen to carbon (H/C) ratio. However, while providing a graphic image of the amount of hydrogen storage on carbon materials, it is ineffective at comparing other types of storage systems.

Given that weight percent (wt. %) of hydrogen to overall storage system is an effective method of comparing various storage systems, it is necessary to define a benchmark for what is considered to be an acceptable level of storage for commercial application. The United States Department of Energy (D.O.E.) operates an extensive hydrogen storage research program. This program has developed a target of 6.5 wt. % and 62.5 kg/m^3 to be acceptable for use in automotive applications. This target is derived from the range of a typical gasoline-powered automobile, as discussed in the previous section. Figure 1-2 illustrates graphically the D.O.E. targets for hydrogen storage compared to current technologies. The following section describes in more detail the various alternative storage methods compared in Figure 1-2.

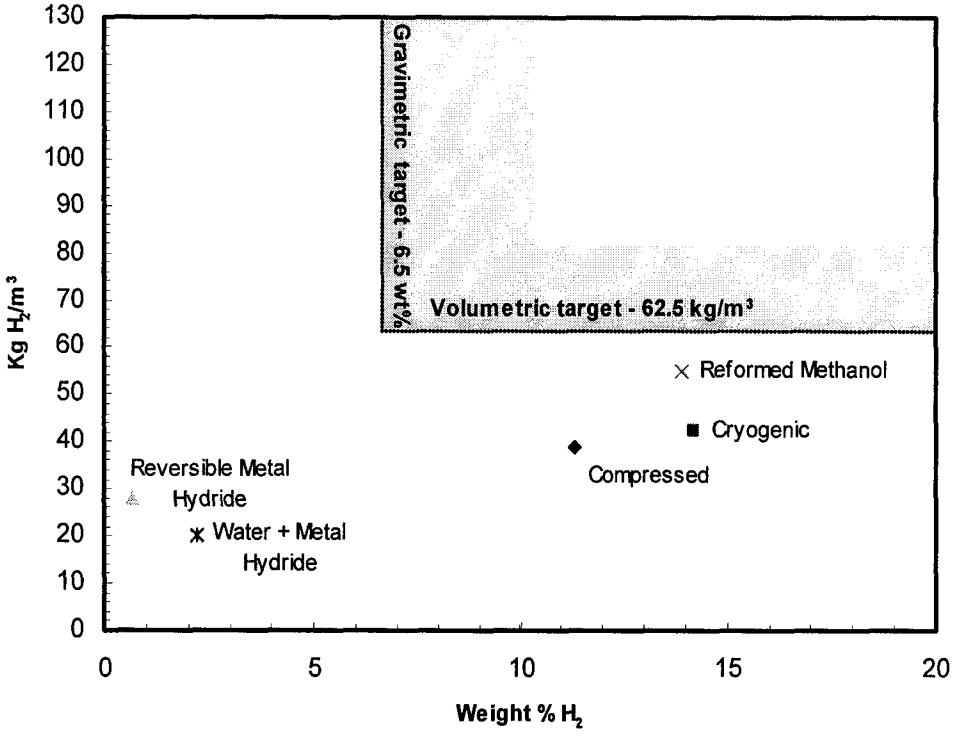

Figure 1-2. DOE hydrogen storage targets compared to state of the art technology. All figures include complete hydrogen delivery systems, not just the materials themselves.

1.3 Existing Hydrogen Storage Technologies

A successful hydrogen storage system must encompass more than simply a unique material or combination of materials- it requires a hydrogen management system made up of tanks, regulators, safety equipment, filling capability and more. At the heart of these parts in many systems lies a unique material such as hydride, nanostructure, or even storage tank structural material. It is important to remember, however, that although the presence of a unique material may be able to hold hydrogen to a level that equates the D.O.E. target of 6.5 wt. %, the system

comprising tank, regulator and safety fittings will be unable to attain this goal. Practically, therefore, the unique material must exceed this target. This fact is often overlooked especially in the reported values for carbon adsorbents found in the literature.

In addition to overall level of hydrogen storage, there are important criteria a hydrogen storage system must pass to be commercially feasible:

1. Easy release of stored hydrogen.
2. Low energy manufacturing process, thereby preserving as much of the potential energy stored in hydrogen as possible.
3. Safety.

The U.S. Department of Energy has further specified that the storage system must be operational below a maximum pressure of 250 atm, and at temperatures between 0 and 100°C to be commercially effective. For the purpose of achieving academic understanding of adsorption storage, however, these limits have been exceeded both in temperature and pressure in the present research.

1.3.1 Compressed Storage

Compressed storage is the most obvious way of storing significant quantities of a gas. Unfortunately, because of the very low density of hydrogen and its very low triple point, excessively high pressures are required to achieve any really useful level of storage. The cylinders typically found in laboratories

are able to store less than 1 wt. %. However, thanks to clever designs by companies such as Quantum Technologies, tanks such as those depicted in Figure 1-3 are reported to be able to store up to 11.3 wt. % at pressures of 5000 psi in laboratory tests. The wall of the tank is made up of an impermeable polymer inner layer, a carbon fiber composite layer for structural strength, and an impact resistant outer layer. In spite of these breakthroughs, the main drawback of a compressed storage system for a portable application is the safety issue.

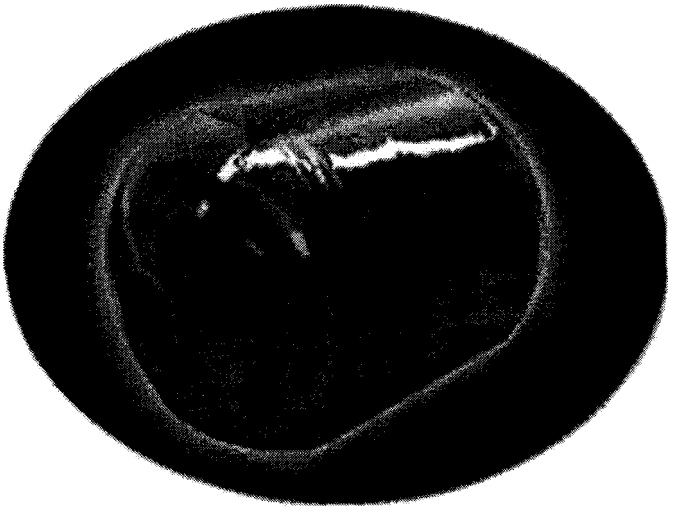

Figure 1-3. Quantum Technologies storage tank capable of storing 11.3wt. % hydrogen. Innovative construction consists of three layers- a permeation resistant polymer liner, a carbon fiber inner layer, and an impact resistant outer shell.

1.3.2 Cryogenic Storage

Liquid hydrogen is currently the highest weight percent storage system available, in part due to advances made by manufacturers of hydrogen internal combustion engines. BMW is one of the forerunners in this technology. At

ambient pressures, liquid hydrogen has a temperature of 22 Kelvin. Cryogenic storage fails the second test of a successful hydrogen storage system, as nearly 40 % of the specific enthalpy of hydrogen is used in the multiple-step procedure required to condense it. Furthermore, liquid hydrogen is impractical for long-term storage. Certain safety issues also stand out as relevant in cryogenic storage- the tanks are typically designed for maximum insulation, and not designed to withstand high-pressure. As a result, cryogenic systems must encompass pressure relief valves that are prone to freezing. In addition, asphalt is flammable at low temperatures so that storage system design must prevent fuel from dripping on to the roadway.

1.3.3 Chemical Storage

Chemical storage of hydrogen has generated a surge of interest recently due to advances in reforming technology. As noted previously, in Section 1.1, the use of a chemical source to power a fuel cell has a disadvantage in that a waste product must be produced. In the case of methanol and other hydrocarbons, this waste typically includes carbon dioxide, and to a lesser extent, carbon monoxide. Aside from being environmentally undesirable, carbon monoxide is also poisonous to the catalyst in a fuel cell electrode, thereby undermining its operation. Nevertheless, chemical storage continues to be explored, and the reason for this is two-fold: hydrocarbons that offer a potential source for hydrogen are produced by oil companies. These companies stand to lose a great deal if

fossil fuels are replaced as a portable fuel source, and therefore are willing to finance proposals that benefit their continued business success. The other reason chemical storage continues to be explored is the fact that a distribution network already exits for many candidate chemicals (esp. methanol).

Some other chemicals that store significant gravimetric quantities of hydrogen include ammonia (17.76 wt. %), diborane (21.86 wt. %), methane (25.13 wt. %), and hydrazine (12.58 wt. %). Unfortunately, in some cases, these materials are too energetically costly to produce, others are too toxic for practical purposes, and others require too much energy to release the hydrogen.

1.3.4 Metal Hydride Storage

A storage method that has, and still does generate a lot of research interest is reversible metal hydrides. In this system, the hydrogen is stored by reacting with a metal or alloy to form a metal hydride. The atomic hydrogen is stored interstitially within the lattice and surprisingly, the separation of individual hydrogen atoms is actually smaller than in the case of liquid hydrogen. Unfortunately, with notable exceptions, especially among magnesium-containing compounds, metal hydrides are composed of heavy elements. As a result, a significant weight penalty is imposed in achieving the high volumetric density. Metal hydrides are generally limited to 1-3 wt. % adsorption. Magnesium-containing hydrides are able to achieve gravimetric storage as high as 7.5 wt. %, but are limited kinetically by the low diffusion rate of hydrogen in these metals.

Many otherwise promising metal hydride materials are also extremely sensitive to impurity and often require vigorous thermal activation procedures.

In addition to volumetric storage, one of the principal attractions of reversible metal hydrides is the predictable thermodynamic equilibrium that governs the storage and release of hydrogen. For the generic exothermic storage reaction,

$$M + x/2\,H_2 \rightarrow MH_x \qquad 1.4$$

where M is a metal or alloy and x is a stoichiometric constant, the behaviour is described by the van't Hoff equation,

$$\ln(P) = -\Delta H / RT \qquad 1.5$$

where P is the partial pressure of hydrogen in atm, R is the universal gas constant 0.082057 atm·L/mole·K, and T is the temperature in Kelvin. From this relation it is clear that the storage reaction occurs when the pressure is raised and/or when the system is cooled. Alternatively, the release of the hydrogen is achieved by increasing the temperature, or by lowering the pressure. The latter is achieved dynamically in practice by consuming the hydrogen in a fuel cell or combustion reaction. Because of the delicate equilibrium, safety is an inherent feature of metal hydrides. Should a puncture occur in a tank containing metal hydrides, the release reaction must occur slowly since the release reaction is endothermic. The initial burst will lower the pressure and evolve hydrogen. However, the release of hydrogen will consume heat, and lower the temperature of the system. The

lowered temperature will, in turn, favour the storage reaction and as a result, the hydrogen will evolve far more slowly than in the case of compressed hydrogen.

An abundance of metal hydrides exist, and the properties of many are in the Hydride Database, maintained by the Sandia National Laboratory in conjunction with the D.O.E. and available for public viewing at http://www.hydpark.ca.sandia.gov. Some of the most favorable reversible metal hydrides in terms of storage and release at near-ambient conditions include lanthanum nickel ($LaNi_5H_7$ – 1.5 wt. %), titanium iron hydride ($TiFeH_2$ – 1.87 wt. %). Magnesium nickel hydride is an example of a hydride with enormous potential ($MgNi_2H_{12}$ – 7.9 wt. %) but suffers from poor kinetics.

1.4 Hydrogen Storage by Adsorption

For the last decade, technologies described until now have been commercially available for use in portable generators, demonstration units, and fuel cell powered vehicles. However, there is a need to develop a better and, in some cases, safer method of storage. Storage by adsorption may be able to achieve these goals.

Despite the well- established understanding of adsorption reactions, there are a number of reasons for adsorptive hydrogen storage failing to find application to date. As will be discussed further in later sections, foremost among these reasons is discrepancy among published researchers concerning the overall level of storage that can be achieved from a given adsorbent. Another important

limitation to date has been the development of a powder suitable for attracting hydrogen to its surface.

The concept behind the use of an adsorbent as a gas-storage medium is that the gas becomes bonded to the surface and condenses. Important issues concerning the effectiveness of a surface include the affinity of the gas to the adsorbent, the overall surface area of the adsorbent, and the presence of any unique structural features that may enhance the bonding of hydrogen to the surface. Concerning the latter, if the surface is constructed of pores or channels that are narrow enough that the attractive force for the gas overlap, it may be possible to increase the overall level of gas adsorbed. To illustrate, nanotubes and slit-pores, shown in Figure 1-4 are possible structures with an increased level of storage. Also shown are the hydrogen density variations expected within pores of different sizes, as calculated by computer simulation. In this study, the authors determined that overlap of attraction was maximized at a pore diameter of 7 Å; however, the accompanying increased density of hydrogen was not enough to overcome the reduced volume of the smaller pores [Rzepka, 1998].

The discovery of carbon nanotubes in 1991 has led to a belief that the inside of the tubes may possess an enormous surface area in a suitable geometry for the hydrogen molecule, and resulted in an enormous volume of research being devoted to determining if this is the case. There is strong evidence both for and against this possibility, and additionally, there is strong evidence to suggest that

further processing of the nanotubes including tube-cutting, purification, and metal doping may increase the effectiveness.

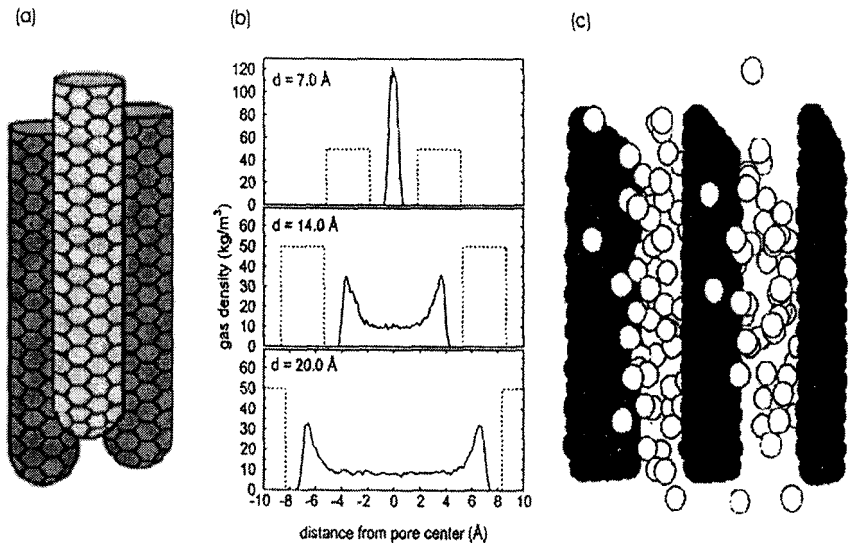

Figure 1-4. (a) Nanotubes, and (c) slit-pores may be more effective adsorbents than planar structures. (b) Density profile of hydrogen within small pores [Rzepka, 1998].

1.4.1 Historical Development of Carbon Nanotubes

Carbon nanotubes are a form of carbon molecules referred to as fullerenes. The first fullerene observed was the C_{60} molecule known as the "buckyball". This form of carbon is composed of symmetrically adjoining pentagon and hexagon rings of carbon such that the otherwise familiar two-dimensional sheet structure of carbon is distorted into a sphere. The C_{60} molecule was initially obtained in the soot created by the use of laser to vaporize a graphite target in an inert atmosphere. The local heating at the surface of the target generated a dense

plasma of carbon that condensed into energetically favorable clusters in the expanding, cooling plasma. The discovery of the C_{60} molecule by Kroto, Heath and Smalley in 1985 initiated a field of study referred to as fullerene science, and was awarded the 1996 Nobel Prize in Chemistry.

Optimization of the synthesis of fullerenes revealed that the temperature and pressure of the inert gas atmosphere were important in controlling the condensation rate of the plasma, and therefore the annealing of the newly formed carbon structures. At temperatures between 1000°C to 1200°C, the yield of fullerenes in the soot increased to 40%. In 1990, an equally effective, yet cheaper method of generating fullerenes was found to be evaporation of a graphite rod by resistive heating [Krätschmer et al., 1990]. AC or DC arc discharge using a graphite electrode generates a carbon plasma similar to that of laser vaporization and similarly produces a high yield of fullerenes when simultaneously annealed in an inert atmosphere.

In 1991, Sumio Iijima of NEC Corporation employed an arc-discharge fullerene production method using a graphite cathode interspersed with transition metals to produce long "microtubules of graphitic carbon". Careful examination using high-resolution microscopy revealed that these were long concentric cylinders of graphite, later dubbed "multi-wall carbon nanotubes". It has long been known that certain transition metals are able to catalyze the production of long thin carbon fibers from hydrocarbon vapour and this method is used to commercially produce structural carbon fibers [Smalley and Colbert, 1995].

Therefore, it is likely that nanotubes were produced prior to 1991, but were not examined with sufficient resolution to reveal their nanotubule structure.

Smalley et al. propose that transition metals including iron, cobalt and nickel that are known to have a high solubility for carbon at elevated temperatures become supersaturated in the carbon plasma. The solution precipitates on the surface of the metal and, under the high annealing temperature, atomically arrange to form pentagons and hexagons within a sheet that conforms to the surface of the metal particle. At the edges of the sheet, only hexagon carbon rings form and the metal particle is lifted off from the graphite electrode. The hexagons continue to be fed from the carbon plasma close to the surface of the electrode, thereby feeding the tube as it grows out from the surface. This mechanism explains why it is rare to observe open-ended nanotubes without post-synthesis treatment, and also why metal particles are often observed enclosed within the hemispherical ends of nanotubes.

Both Iijima of Japan, and Bethune et al. at IBM in the United States later found that when certain carbide forming transition metals were used in the composite graphite electrode, a different morphology of nanotube was produced [Iijima and Ichihasi, 1993; Bethune and Kiang, 1993]. These new tubes were composed of only one atomic layer of graphite, as opposed to the multiple concentric layers of multi-wall nanotubes.

Single-wall nanotubes can be imagined as single-graphite sheets that have been rolled into a seamless cylinder. As shown in Figure 1-5, depending on the

orientation of the graphite sheet, the tubes can have slightly different atomic arrangements. The discovery of these tubes has led to a decade of extensive research into a variety of intriguing mechanical, electrical and chemical properties that theory suggests they may possess [Collins and Avouris, 2000]. Aside from electric arc discharge, other methods of synthesis have been found including laser-vaporization, and chemical vapor deposition.

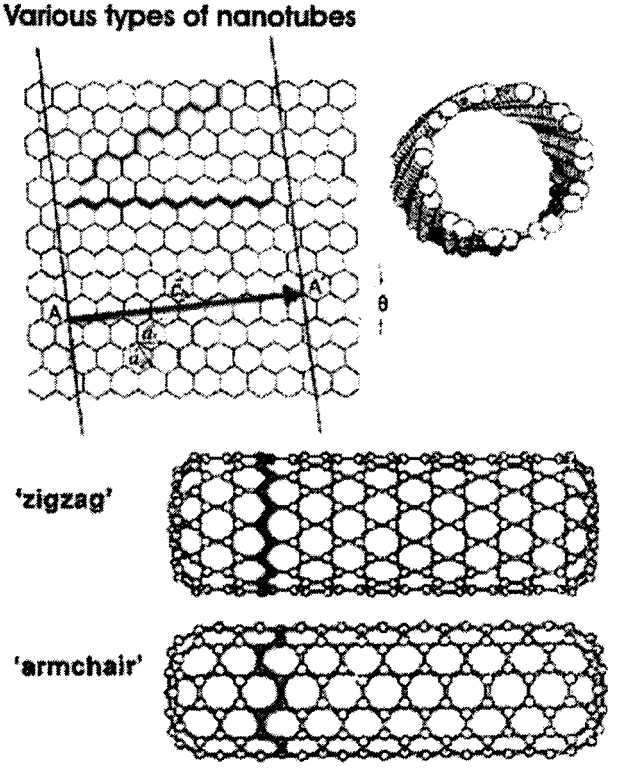

Figure 1-5. Nanotube orientations relative to a graphite plane.

The original nanotubes possessed a seemingly consistent diameter of 1.2 nm, although the development of new synthesis methods has revealed subtle

differences, and they are now known to have diameters varying between 0.9 nm, and 1.8 nm. Furthermore, it is unusual for lone single-wall nanotubes to be produced. They are more often found in a close packed triangular lattice, referred to as a bundle. Each bundle has a diameter of 10-100 nm, and is composed of 10-100 tubes.

1.4.2 Unresolved Controversy

Since the discovery of carbon nanotubes in 1991 (Iijima, 1991), and the pioneering report that they may be able to store significantly higher amounts of hydrogen than planar carbon (Dillon et al., 1997), an enormous volume of research has been generated into this intriguing property. The published works examine the interaction of hydrogen with a variety of carbon structures in theory, modeling and experiment. The works are often contradictory, sometimes to the point of animosity amongst zealous proponents of differing experimental results (Zandonella, 2001). Much of the discrepancy arises because of the absence of a plateau of adsorption with increasing pressure in the published reports. Instead, adsorption appears to increase uninterrupted to the pressure limit of the instruments used. Such a feature would lend credence to the reported adsorption capacity. The differing results present a confused picture, and highlight a need for a fresh approach.

1.5 Research Objectives

The purpose of this work is to measure the level of adsorption on carbon nanotubes and thereby resolve the controversy within literature data. Furthermore, the goals of this research are to address the following points.

1) Achieve a plateau of adsorption of hydrogen under high pressure, thereby clarifying the capacity of carbon nanotubes.
2) Determine whether bundles of nanotubes separate under the influence of high pressure hydrogen by *in situ* measurement of changes in resistivity of bulk single-walled carbon nanotubes.
3) Investigate the effect of the presence of metals on the level of adsorption of hydrogen on carbon nanotubes and carbon nanotube bundles.

1.6 Thesis Overview

The remainder of this thesis is broken down into four chapters. Chapter 2.0 provides background information relevant to the thesis including basic adsorption theory and previous work done on the topic of adsorption on carbon nanotubes, including experiments and computer modeling. Chapter 3.0 details the experimental method and instrument construction. A new high pressure volumetric adsorption measurement system was designed and built to investigate hydrogen storage on carbon nanotubes in a previously unexplored regime. Several published findings on the topic of hydrogen storage by adsorption have

been questioned on the basis of experimental flaws, and as a result, careful instrument construction and extensive calibration comprised a significant portion of the research work conducted. In addition, a novel method of evaluating previous reports [Ye et al., 1999] of nanotube bundle separation under high pressure using electrical resistance measurement was devised. Chapter 4.0 provides the experimental results, analysis and discussion, including a new model of adsorption on nanotube bundles employing simple geometrical considerations. Chapter 5.0 gives the conclusions.

2.0 Literature Review

Relevant published research includes that which contributes to an expectation of how hydrogen will behave in the proximity of carbon nanotubes and other similar nanostructures, as well as the expectation of how these nanostructures will behave in the presence of hydrogen. Although the study of adsorbents and related works on catalysis is old and well established, nanotubes as adsorbents have been studied for only 5 – 6 years. In this time worldwide attention to the topic has led to many important models and experimental findings being developed. Following an overview of relevant theories on adsorption, these findings will be reviewed in this section.

2.1 Adsorption Theory

Adsorption of a gas on a solid surface is a special case of a broad field of study, referred to as adsorption theory. Two common applications of adsorption are the determination of surface area of powders and the separation of chemicals using selective adsorption by specially modified surface features of a liquid or solid adsorbent. Adsorption on a solid or liquid surface arises due to the presence of an overall short-range attractive force at a surface. Depending on the nature of the chemical species making up the adsorbent and adsorbate, this attraction may

result from several different forces. The types of forces, and the characteristic adsorption that result from them are reviewed in this section. In addition, the forces significant to the interaction of hydrogen with carbon are examined.

Adsorption involves a mixture of direct adsorbate surface binding and pore condensation. Pore condensation occurs because, due to surface tension, a small drop of fluid has a larger vapour pressure than a bulk fluid. If the drop has a radius R_{drop}, then the vapour pressure of the drop, P_{drop}, can be calculated by

$$kT \ln\left(\frac{P_{drop}}{P_{vapour}}\right) = \frac{2\gamma_{drop} V_{drop}}{R_{drop}} \qquad 2.1$$

where P_{vapour} is the vapour pressure of the bulk fluid, γ_{drop} is the surface tension of the drop, V_{drop} is the molar volume of the drop, k is the Boltzmann's constant, and T is temperature. This equation is referred to as the Kelvin equation. Note that this equation applies to the condensation of a fluid in a narrow capillary, as shown in Figure 2-1. As indicated in the figure, when a fluid condenses in a capillary, the radius of curvature is negative. Therefore, the vapour pressure of the fluid in the pore is less than the bulk vapour pressure. Unfortunately, evidence exists to show that the Kelvin equation does not work when the pore size gets below 10 molecular diameters, and as a result is inappropriate for nanostructured materials like carbon nanotubes [Masel, 1996]. Pore condensation is most important for fluids near or below their boiling point, while direct adsorbate/surface binding dominates at higher temperatures [Masel, 1996].

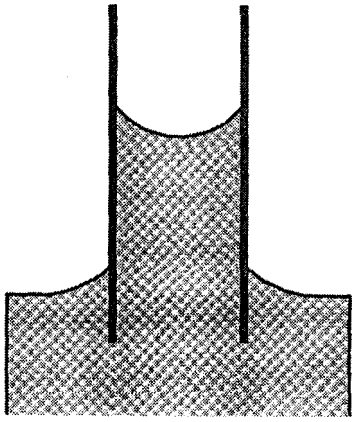

Figure 2-1. A fluid inside a small capillary.

Typically gases adsorb on surfaces with one layer adjacent the surface, and possibly several layers condensed onto the first layer. The first layer interacts strongly with the surface and therefore forms a physical or chemical bond to the surface. Subsequent layers, however, will have progressively weaker interaction with the surface and instead will interact with the adsorbed layers. As a result, multilayer adsorption is likened to a condensation reaction where a liquid-like film forms over the first layer. In the same way that a liquid will not condense far above its boiling point, it is unlikely to form multilayers of a pure adsorbent except at or near the boiling point. Generally, for multilayers to form, adsorbate/adsorbate interactions must be strong relative to kT [Masel, 1996].

2.1.1 Physical Adsorption

Adsorption is typically classified into two broad categories, physical adsorption and chemical adsorption, abbreviated physisorption and chemisorption, respectively. Due to the action of different types of forces, there are usually elements of both in any given system. Physisorption is the weaker of the two, and is the result of the action of electronic dispersion forces otherwise known as van der Waals forces. On the other hand, chemisorption is the result of chemical bond formation between the adsorbate and the adsorbent. The distinction between physisorption and chemisorption is often made by a measure of the binding energy with which the adsorbate is held to the adsorbent.

Briefly, the physical attractive forces referred to as dispersion forces arise from the rapid fluctuation in electron density within atoms. The fluctuation in one atom induces an electrical moment in a neighboring atom, thereby leading to mutual attraction [Gregg and Sing, 1982]. The potential energy, ε_D, of this dipole-dipole attraction varies as the distance between the two atomic centers, r, according to

$$\varepsilon_D(r) = -Cr^{-6} \qquad 2.2$$

In this expression, C is referred to as a dispersion constant and depends on the specific atoms involved. A more rigorous evaluation of the attractive force includes higher order terms representing dipole-quadrupole, and quadrupole-quadrupole attraction, but these are generally omitted as the uncertainty that exists

in applying the expression to numerical calculations is large relative to these higher order terms [Gregg and Sing, 1982].

In addition to the attractive force, there is a repulsive force that arises due to the overlap of the electron clouds of the adjacent atoms. This repulsive force generally decays exponentially as the distance between the atom centers and as a result is short-range compared to the attractive force according to

$$\varepsilon_R(r) = Br^{-m} \qquad 2.3$$

where B and m are empirical constants. The constant m is typically considered to be independent of the particular species involved, and is assigned a value of 12. Figure 2-2 sums the combination of the two forces, commonly referred to as the well-known Lennard-Jones potential,

$$\varepsilon(r) = -Cr^{-6} + Br^{-12} \qquad 2.4$$

Figure 2-2 depicts the minimum that occurs in the potential at a unique separation distance, r_o. The depth of the minimum is referred to as the potential well, and is a measure of the strength of attraction between the two adjacent atoms. An interaction of the form in Equation 2.4 is typical of two atoms in the gas-phase.

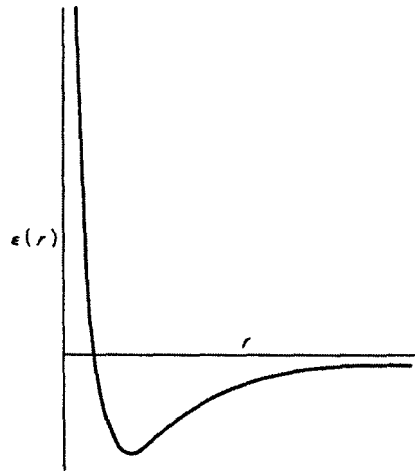

Figure 2-2. Lennard Jones potential adjacent a surface. [Gregg and Sing, 1982].

For an atom in proximity to a surface composed of numerous atoms, the overall attraction $\phi(z)$ is a summation of the pair-wise (i.e. the gaseous atom paired with individual atoms in the surface) interactions [Gregg and Sing, 1982],

$$\phi(z) = C_{ij}\sum_{j} r_{ij}^{-6} + B_{ij}\sum_{j} r_{ij}^{-12} \qquad 2.5$$

where r_{ij} is the distance between the atom i in the gas phase and the center of atom j in the solid. In the special case of an atom or molecule adjacent a flat surface, as in the case of a particular face of a crystalline solid, or in the case of a graphite sheet, the distances r_{ij} become one value, z. z is the distance between the center of the gaseous species, and the plane through the center of the atoms making up the outermost layer of the solid. For practical calculation, the number of pair-wise summations can be limited by specifying a cut-off distance. This approximation does little to degrade the accuracy of the model as the potential

depicted in Figure 2-2 falls off rapidly with distance. For adsorption on a close-packed surface, Equation 2.5 is often simplified by integration. The assumption in doing so is that the surface behaves as a continuum in the presence of adsorbing species, rather than an array of isolated adsorption sites. However, the basal plane of the graphite lattice is not densely packed and is more often treated as a summation in computer models [Gregg and Sing, 1982].

An atom or molecule in the proximity of a surface will experience forces of the form of Equation 2.4 due to other gaseous atoms in addition to forces of the form of Equation 2.5 due to surfaces. Even within the relatively short distances over which van der Waals forces act, there are therefore an enormous number of summations required to effectively model the state of an adsorbent atom. As a result, computer methods are often employed including density functional simulations, and Monte Carlo statistical techniques (see Sections 2.2.1.2 and 2.2.1.3).

2.1.2 Chemical Adsorption

While physisorption is generally characterized by intact molecules held to a surface by polarization, chemical adsorption (chemisorption) is characterized by chemical bond formation between the adsorbate and the adsorbent. Chemisorption is sometimes defined as a system in which the electronic structure of the chemisorbed species is significantly altered [Masel, 1996]. This definition is somewhat flimsy, and as a result, it is useful to distinguish between the

adsorbed states using the strength of attraction, or heat of adsorption. The heat of adsorption is species specific, but is typically 8 – 40 kJ/mol for physisorption, and 40 – 400 kJ/mol for chemisorption.

In some cases, as is frequently the case with hydrogen, the adsorbing molecule will dissociate, and the atoms or smaller components of the molecule will react independently with the surface atoms. Hydrogen is a simple case since if it adsorbs as a molecule it is physisorbed, and if it dissociates and adsorbs atomically, it is chemisorbed. The Lennard-Jones model, described in the last section can be adapted to describe possible interactions between hydrogen and a given adsorbent. Since energy is required for hydrogen to dissociate into two hydrogen atoms, the energy for free atoms is larger than that for the molecule at large distances from a surface, as shown in Figure 2-3 [Masel, 1996]. If a surface favours adsorption of hydrogen chemically, however, then the dissociated state will be more stable adjacent the surface. This is shown by a deeper well closer to the surface for the dissociated state than the molecular state. As is often the case for hydrogen on transition metals, it may be possible for the adsorbed hydrogen to move from a molecular state to a dissociated one, and for it to do so requires it to surmount the energy barrier given by the crossing of the two lines.

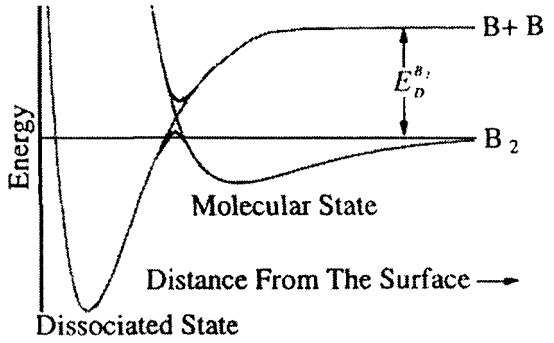

Figure 2-3. Relative energies of molecular adsorption and dissociated adsorption.

This presents three possibilities, shown by the three graphs in Figure 2-4 [Masel, 1996]. The first possibility is that the physisorbed state is preferred, in which case, the molecular potential well is deeper, though further removed from the surface, than the dissociated curve. In this case, there is little probability of the molecule surmounting the energy barrier for dissociation, and physisorption is expected. The second possibility, shown in Figure 2-4b, is similar to that shown in Figure 2-3. In this case, the dissociated (chemisorbed) state has a deeper potential well, but the molecule must surmount an activation energy barrier to achieve this state. The third case, shown in Figure 2-4c, occurs when the activation energy for dissociation lies below the energy of the free molecule, away from the surface. As a result, the molecule should be able to chemisorb directly without activation. However, through collisions with other molecules close to the surface, the molecule may lose energy and fall into the physisorbed state. A mixture of molecular and atomic states would likely be found on the surface as a result of this type of interaction.

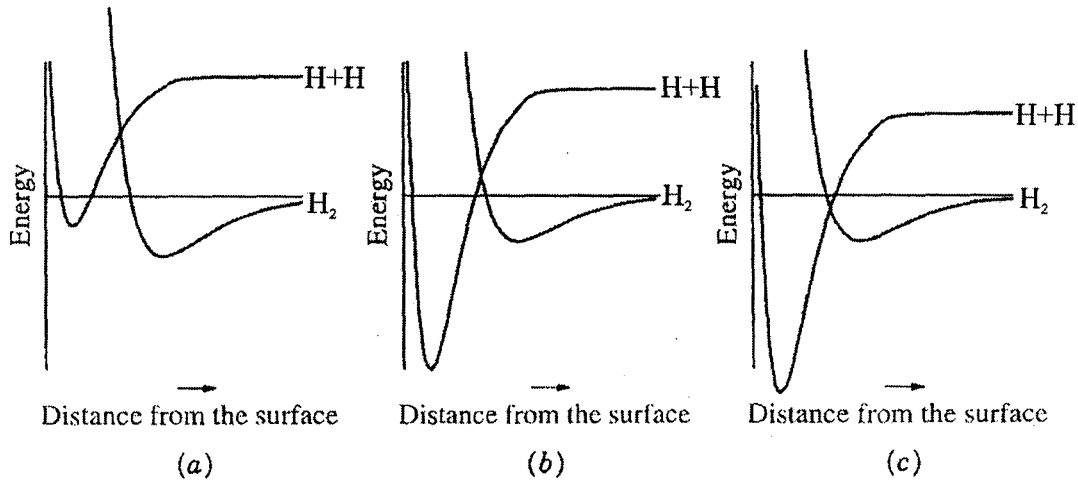

Figure 2-4. In the Lennard-Jones model, possible energy configurations include (a) the system favours molecular adsorption, (b) the system favours atomic adsorption, and (c) the system favours atomic adsorption, but the energy barrier between the molecular adsorption and atomic adsorption is below that of the free diatomic molecule.

Potentially, every carbon atom in a carbon nanotube could be a site for chemisorption of one hydrogen atom, as the bonding between carbon atoms is unsaturated. Experimental evidence exists to suggest that some chemisorption occurs on exposure of carbon nanotubes to pressure [Liu et al., 1999].

2.1.3 Langmuir, BET

The experimental observation of adsorption is usually expressed by the isotherm, which gives the composition (or amount adsorbed) versus pressure at a fixed temperature. Many models have been developed to explain experimental isotherms in terms of energy, pore size, surface area, and species specific interaction. The most fundamental model is the Langmuir model, depicted in

Figure 2-5. Langmuir's theory is derived on the assumption that full coverage has occurred when a monolayer has adsorbed on the surface and there is no interaction between adsorbed molecules. Furthermore, Langmuir assumes that the energy of adsorption is constant, independent of adsorption. If θ is the fraction of surface coverage, and at equilibrium the rate of molecules adsorbing to the surface is equal to the rate of molecules leaving the surface, then

$$k_d\theta = k_aP(1-\theta) \qquad 2.6$$

where k_d is the desorption rate constant, k_a is the adsorption rate constant, and P is an expression of the rate at which molecules are striking the surface- the pressure. The rate constants of Equation 2.6 are dependent on temperature according to

$$k_{d,a} \propto e^{\frac{-E_{d,a}}{RT}} \qquad 2.7$$

In this case, E is the activation energy for adsorption or desorption, T is the temperature in Kelvin, and R is the universal gas constant. Rearranging Equation 2.7 and substituting expressions of the form 2.6 for the rate constants yields the most common expression of the Langmuir adsorption isotherm,

$$\theta = \frac{bP}{1+bP} \qquad 2.8$$

where

$$b = \frac{k_a}{k_d} \propto e^{\frac{-(E_a-E_d)}{RT}} \qquad 2.9$$

is the rate constant for adsorption, and $E_a - E_d = \Delta H_a$ is the enthalpy of adsorption, assumed independent of coverage.

The Langmuir isotherm has the profile shown in Figure 2-5, where the level of coverage increases with pressure and eventually saturates at full coverage. Figure 2-5 also shows that as the temperature decreases, a higher level of coverage will be attained at a given pressure. Ye et al. used the Langmuir isotherm to model hydrogen adsorption on carbon nanotube bundles at liquid nitrogen temperature and at room temperature [Ye et al., 1999]. At low pressures (<40 bar), the isotherm was found to follow a Langmuir profile, but a deviation occurs at higher pressures. There appears to be an increase in coverage above a monolayer. The authors suggested that this deviation may be due to separation of the nanotube bundles, resulting in higher surface area available for coverage.

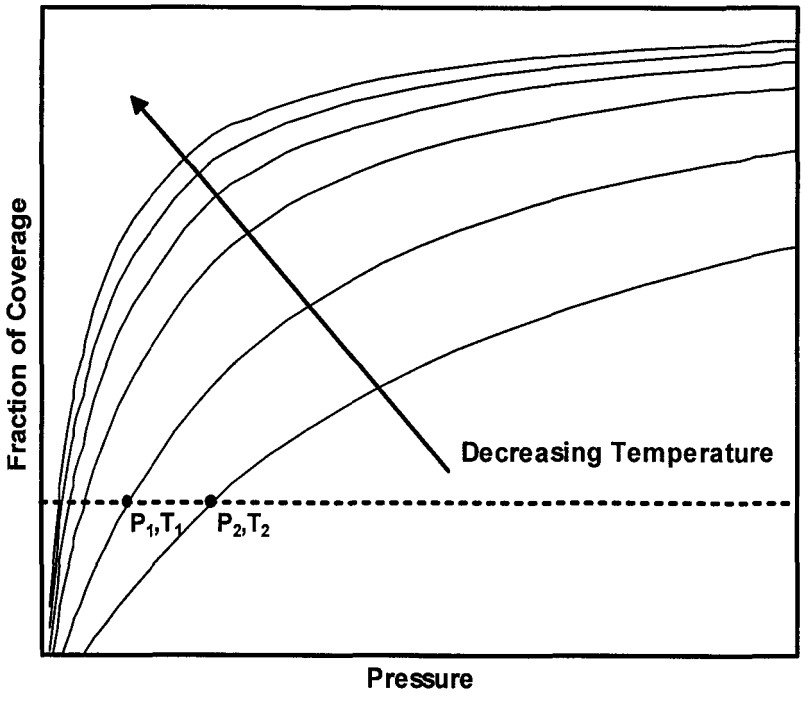

Figure 2-5. A given level of coverage is attained at lower pressure when the system is cooled. $P_2>P_1$ *and* $T_1<T_2$.

The example of Ye et al. illustrates a convenient feature of the Langmuir model, that is, it provides a simple way of quantifying the adsorption energy, and hence a way of quantifying the strength of the adsorption bond. If the isotherm for a particular adsorbent-adsorbate system can be measured at two or more temperatures, the pressure required to achieve a certain level of surface coverage can be used in the Clausius-Clapeyron equation,

$$\left(\frac{\partial \ln P}{\partial 1/T}\right)_{\theta} = \frac{\Delta H_{ads}}{R} \qquad 2.10$$

A plot of lnP versus 1/T should therefore give a straight line with a slope of $\Delta H/R$ for a reversible adsorption process.

An alternative model of adsorption developed by Brunauer, Emmett, and Teller (BET) builds upon the monolayer adsorption equation to explain alternative isotherm profiles. Since the adsorbent species making up the second layer are shielded from the adsorbent by the first adsorbed layer, the formation of the second and subsequent layers is similar to a condensation reaction. The forces driving the second layer to arrange to form a layer upon itself are the same as if the pure species were arranging to form a liquid. If experimental conditions of pressure and temperature are above the boiling point of the gas, multilayers are not expected to form unless the geometry of the adsorbent is made up of pores or valleys that allow adjacent surface potentials to overlap. As a result, the BET theory is widely used to characterize the porosity of solid materials by the shape of the isotherm. There are five classifications of that cover the majority of isotherm shapes, labeled I through V, as depicted in Figure 2-6.

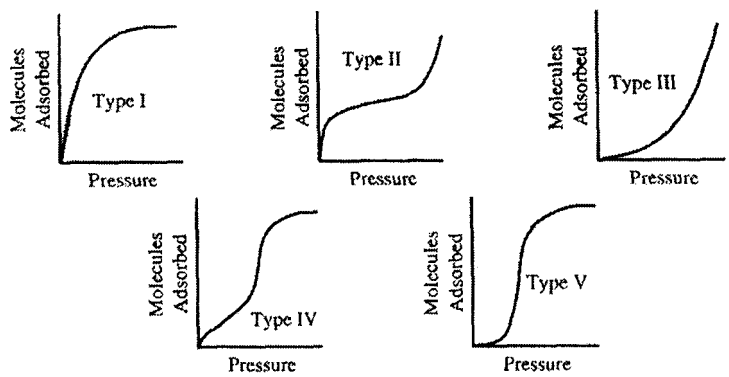

Figure 2-6. The five types of adsorption isotherms [Masel, 1996].

The Type I isotherm is similar to the Langmuir isotherm, where the amount of adsorbed gas increases with pressure and saturates at a monolayer of coverage. This type of isotherm is also observed in cases where the adsorbent contains many small pores that fill up all at once [Masel, 1996]. Type II isotherms are characteristic of multilayer adsorption whereby the adsorbed amount reaches a steady state at a monolayer of coverage, and then rapidly increases as the pressure of the gas approaches its saturation vapour pressure. In this part of the curve, the adsorption increases rapidly because the gas condenses to form a thick liquid layer on any surface in the same way that dew forms on the ground. This type of behaviour is typically observed in BET surface area measurements at 77 K, where the adsorption of nitrogen is measured as the pressure is increased from vacuum to the saturation vapour pressure. Type III isotherms are observed when the adsorbate does not interact strongly with the adsorbent. Initially, patches of adsorbed species develop and grow due to adsorbate-adsorbate interaction. The adsorption rapidly increases as the patches grow together and cover the surface. Type IV and Type V are less commonly observed, and may indicate that multilayers forming within pores become so thick as to fill up the pores, after which no more adsorption can occur.

Hydrogen is a very small, energetic molecule having a boiling point of only 20 K. It is therefore expected that at temperatures close to ambient, condensation is unlikely to occur and adsorption will be limited to no more than a

monolayer. The isotherm of hydrogen on activated carbon is Type I, and is well described by the Langmuir model [Darkrim et al., 1999, Bénard and Chahine, 2001].

2.2 Hydrogen adsorption on carbon

The initial report of high room temperature storage on single-walled carbon nanotubes by the U.S. National Renewable Energy Laboratory in 1997 proposed that nanotubes had a geometry ideally suited for holding large amounts of hydrogen within [Dillon et al., 1997]. This report initiated extensive study into this intriguing possibility through modeling and further experimentation. Unfortunately, the results of these subsequent investigations are inconsistent and neglect to offer a plateau of adsorption with pressure. This would demonstrate a storage capacity, and thereby confirm the findings. A review of the relevant work will show that the understanding of this system is not yet complete and highlight the need for further research.

2.2.1 Models

2.2.1.1 Geometrical Calculation

The simplest method of calculating the amount of hydrogen adsorption on carbon nanotubes is to take a purely geometrical approach, similar to Dresselhaus et al. [Desselhaus et al., 1999] and Züttel et al. [Züttel, 2002]. A graphite sheet

has a planar hexagon structure with a C-C bond length of 0.142 nm. The hexagon unit cell is has an area of 0.05239 nm^2 and contains two carbon atoms. The theoretical surface area of a single graphite sheet if both sides are considered is therefore 2627 m^2/g. This is also the surface area of a lone single wall carbon nanotube if both the inside and outside are exposed. If the adsorbing gas is unable to access the interior of the nanotube, however, then the surface area of a lone nanotube is 2627/2 = 1313 m^2/g.

One of the principle assumptions in a B.E.T. surface area measurement is that an adsorbed layer of nitrogen has a density similar to that of liquid. As a first approximation, the same assumption can then made for hydrogen. Within a bulk of liquid hydrogen, if the atoms are assumed to be spherical and close-packed, then the equivalent diameter of a single hydrogen molecule can be calculated using a packing factor of 0.7405,

$$V = \frac{4}{3}\pi r^3 = 0.7405\frac{M}{\rho N_A} \qquad 2.11$$

where V is the volume occupied by a hydrogen molecule, N_A is Avogadro's number = 6.022×10^{23} mol^{-1}, M is the molar mass of hydrogen = 2.016 g/mol, and ρ is the density of liquid hydrogen = 71 kg/m^3. From this calculation, r = 0.2028 nm, and the surface area occupied by a hydrogen molecule, A_{H2} is 0.129 nm^2.

One side of an isolated graphite sheet with a surface area, S_C, of 1313 m^2/g should therefore have a monolayer hydrogen storage capacity of

$$wt\% = \frac{S_C \cdot M_{H_2}}{A_{H_2} \cdot N_A} \cdot 100 = 3.4\% \qquad 2.12$$

For a graphite sheet rolled into a tube, the surface area of the adsorbed hydrogen layer will be larger than the surface area of the tube due to the distance between the tube surface and the adsorbed layer. Dresselhaus et al. estimate the adsorption distance as 3.4 Å for physisorption, and a typical nanotube has a diameter of 13.8 Å [Dresselhaus et al., 1999]. Therefore, the monolayer hydrogen storage of the exterior of an isolated nanotube is 4.8 wt. %.

As illustrated by Figure 2-7, within a close-packed bundle of nanotubes, the exposed surface area is much lower, but the adsorption potential of adjacent surfaces within the bundle may overlap leading to higher adsorption. These concepts are explored further in Section 4.4 of the Results section, where a model of bundle adsorption is presented.

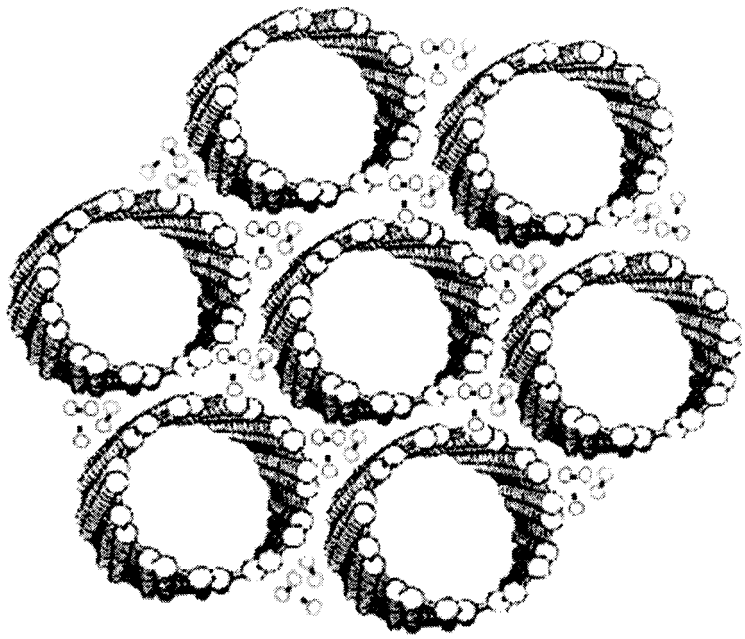

Figure 2-7. Channels between nanotubes within a nanotube bundle may have overlapping attraction potential for hydrogen, as in the interior of the tube.

2.2.1.2 Grand Canonical Monte Carlo (GCMC)

A geometrical model provides only an estimate of the storage level of one complete monolayer. The fraction of the monolayer increases with pressure due to its dependence on chemical potential, as described in Section 2.1.3. The fraction of a monolayer, and whether or not additional layers form requires more complicated accounting of the adsorbent-adsorbate and adsorbate-adsorbate interactions. Several authors have used computer modeling to investigate this behaviour, as summarized in these next two sections.

Monte Carlo molecular simulation is a technique whereby a computer chooses random motion events of atoms or molecules within a simulation cell.

Following each random event, the interaction potentials experienced by the particle are summed and a probability map gives a likely distribution at thermodynamic equilibrium. The complexity of the simulation cell, the range of the interaction potential and the number of particles selected depend on the power of the computing system and the time to complete the test. Furthermore, variations of the simulation are possible depending on which thermodynamic parameters are held constant. The simulation most suited to the hydrogen adsorption system is the so-called Grand Canonical (GC) method, often represented by μVT. This means that equilibrium is evaluated at constant chemical potential (μ), volume (V) and temperature (T). Constant chemical potential under these conditions and in the case of a pure adsorbent like hydrogen is equivalent to constant gas pressure. Since no attempt is made to model electronic interaction, the GC method models only physisorption.

A number of studies were done in recent years to attempt to account for the extremely high gravimetric storage density observed in carbon nanofibers [Chambers et al., 1998], and enhanced storage in carbon nanotubes [Dillon et al., 1997].

Wang and Johnson attempted to vary the strength of the Lennard-Jones interaction potential, Equation 2.5 in a GCMC model to obtain an adsorption consistent with the observations of Chambers et al. [Wang and Johnson, 1999]. They concluded that the depth of the well must be increased by 150 times and thereby ruled out any known physical explanation for the observations.

Rzepka et al. used GCMC to compare carbon nanofibers and nanotubes, and provided a correlation between the findings of their model, and their own experimental findings at room temperature and 100 atm [Rzepka, 1998]. Through simulation methods, they are able to clearly show the increase in density of hydrogen that will occur as a result of overlap of adjacent pore walls. However, as seen in their graphs, reproduced in Figure 1-4b, they found that at the minimum wall spacing of 7 Å, in which one hydrogen molecule can fit, the pore is too narrow for the increased potential to provide an appreciable increase in storage. At larger pore sizes, the potential is too short-ranged to overlap, and the adsorption is similar to that of a single carbon surface. As a result, the amount of adsorption varies with the surface area of the carbon sample according to 0.35 wt. %/1000m^2/g. The minimum pore spacing they observed for adsorption to occur implies a hydrogen-carbon distance of 3.5 Å.

A GCMC model undertaken by Gu et al., took a similar approach to that of the geometrical model presented in Section 2.2.1.1. This model goes beyond that simplistic approach by including a summation of the interaction potentials between adsorbing molecules, and between adsorbing molecules and the surface to obtain a prediction of the amount of adsorption over a range of pressures rather than the upper bounds. The study also examined tubes of different sizes, and different inter-tube spacing within the bundle. Overall, the findings are similar to those of Rzepka et al., in that a pore size of 7 Å allows one adsorbed layer, and the potential overlap gives an appreciable increase in density. An interesting

finding of this study concerns the variation of storage with separation of the tubes within a bundle. A maximum occurs at a separation in which one layer can form between the tubes. As the tube separation increases, the inter-tube adsorption decreases as adjacent surface potentials no longer overlap. At a separation that allows two layers to form, another maximum occurs, but lower than the first because the extent to which each layer is filled is less. The study also found that the size of the tubes making up the bundle has little effect on the adsorption.

The isotherm calculated by Gu et al. fails to show a plateau consistent with the formation of a complete monolayer up to a pressure of 100 atm at room temperature. The maximum adsorption at this pressure was found to be 1.1 wt. % and presumes that the interior surface of the nanotubes is accessible.

Simonyan and Johnson also examined the effect of bundle spacing on adsorption by computer simulation [Simonyan and Johnson, 2002]. Their findings are consistent with the report by Ye et al. that separation of bundles at 80 K to expose new surface area occurs under high-pressure [Ye et al., 1999] When the tube separation within the bundle was allowed to increase to 11 Å, which corresponds to 2 or 3 adsorbed layers of hydrogen, the predicted adsorption increase with pressure is very close to the experimental observation. This finding does not necessarily contradict that of Gu et al, because their model was done at a temperature of 293 K, while this one was done at 80 K. It is very likely that multilayers will form easier at lower temperature.

2.2.1.3 Density Functional Theory

Density functional theory takes a quantum mechanical approach to modeling chemisorption phenomena by calculating wavefunctions as a function of atomic core positions, and uses the wavefunctions to calculate bond energies.

Lee and Lee observed a distortion of the tube wall when hydrogen chemisorbed on the exterior of the tube wall with the average C-C bond length increasing from 1.44 Å to 1.54 Å [Lee and Lee, 2000]. Similarly, chemisorption on the interior draws the tube wall inward. However, the authors find that on the interior of the tube molecular hydrogen has a lower energy than chemisorbed hydrogen. Hydrogen molecules on the interior tend to repel each other, and also the tube wall, again resulting in tube expansion. The formation of a chemisorbed ring on the interior and exterior top of the nanotube, in addition to the molecular hydrogen within the tubes results in an expected maximum storage capacity of 14.3 wt. % for a (10,10) nanotube. In this instance, the hydrogen is proposed to be introduced to the nanotube using electrochemical methods, not using pressure.

Alternatively, a study in which the hydrogen is proposed to be introduced by very high pressures was done by Chan et al. [Chan et al., 2001]. These authors found it was unlikely that hydrogen would chemically adsorb on a single nanotube because the energy of two chemisorbed hydrogen atoms (2.54 eV) is unable to compensate for the energy required to break the hydrogen-hydrogen bond (4.52 eV). Furthermore, the van der Waals repulsion between the nanotube and the hydrogen molecule at a distance of less than 1.8 Å is greater than the

binding energy of the molecule, making it unlikely for the molecule to approach close enough to form the expected chemisorbed bond of length 1.1 Å. Between nanotubes in a bundle or a solid array, however, the van der Waals repulsion is reduced by the proximity of two nanotube walls on which one each of the hydrogen atoms in the molecule could be chemisorbed. In this case, extremely high external pressure (30 kiloBar, 29600 atm) is required to sufficiently reduce the equilibrium separation of the nanotubes making this adsorption morphology impractical, at best.

2.2.2 Previous Experiment Results

2.2.2.1 Carbon Nanotubes and other Carbon Nanostructures

A number of relevant studies have been done since the first report of hydrogen adsorption in carbon nanotubes by Dillon et al. [Dillon et al., 1997]. This first publication is the subject of controversy as the authors used an estimated nanotube purity of only 0.1 wt. % and assumed the remaining fraction consisting of amorphous carbon, other carbon species, and residual catalyst did not adsorb at all. By extrapolation, the authors predicted pure nanotubes would adsorb 5-10 wt. % hydrogen. However, it is known that other forms of carbon are able to store hydrogen in limited amounts [Nijkamp et al., 2001].

A great deal of excitement was generated the following year by Chambers et al., who reported that a uniquely structured carbon nanofiber was able to store

67 wt. % hydrogen at room temperature and a pressure action of 100 atm. The fibers are only 5 nm in diameter, composed of parallel slit pores oriented perpendicular, parallel, and at an angle to the fiber axis. This geometry is proposed to be effective by the authors because of the large number of edge sites containing dangling bonds. Furthermore, the authors proposed that once adsorbed on the edge sites, hydrogen could move within the slitpores and cause the pores to expand, enabling more hydrogen to adsorb. A GCMC model published in the same year by other researchers indicated that the energy potential depth required to achieve such a level of adsorption was 150 times that expected from van der Waals forces [Wang and Johnson, 1999]. Furthermore, Wang and Johnson point out that hydrogen forms a physisorbed monolayer on graphite at a distance of 3.51 Å. Therefore it is surprising that hydrogen was even able to penetrate within the dimensions of the narrow pores (3.37 Å) of the nanofibers. Other experimenters were unable to reproduce such high levels of adsorption on nanofibers produced by a variety of methods [Ahn et al., 1998]. These authors further found that the measured heat of adsorption on these nanofibers was very similar to that found on activated carbon, indicating that hydrogen is held no more strongly on nanofibers than any high surface area carbon. Together with the results of Wang and Johnson this finding indicates that it may be appropriate to dismiss the findings of Chambers at al., until new information suggests otherwise. For their part, the latter authors maintain that their findings are valid, but due to the proprietary

interests of financial supporters, they are unable to divulge the nature of this catalyst [Zandonella, 2001].

A similar structure that offers a large number of edges and dangling bonds is described by its discoverers as a carbon nitride "nanobell" [Bai et al., 2001]. These fibers contain stacks of rounded cones, again having a large number of edges, and also as proposed by the authors, a cavity at the tip of each cone within which hydrogen may be stored, once accessed through the interlayer spacing. Their results are promising at 8 wt. %, though not to the extent of Chambers et al.

Early work on the measurement of hydrogen adsorption of single-walled carbon nanotubes includes the work of Liu et al. who examined samples having an estimated purity of 50 wt. %. They observed a maximum hydrogen uptake of 4.2 wt. % at room temperature and 120 atm if the samples were first treated with hydrochloric acid and heat-treated under vacuum at 773 K for purposes of purification. Some significant observations of this work include an apparent weight increase following testing at high pressures that was subsequently removed by heating. This suggested to the authors that up to 25 % of the adsorbed hydrogen was in a chemisorbed state due to the high temperature required to degass the sample. Another important observation was that the hydrogen uptake was less than 1 wt. % if the pressure was less than 50 atm, indicating that elevated hydrogen pressure is a requirement to obtain significant hydrogen storage. However, other workers believe that this observation may be

related to thermal fluctuation caused by adiabatic expansion of the gas (see below, Figure 2-9).

Studies on the hydrogen storage amounts of carbon nanotubes have recently taken on two strategies – internal and external adsorption. Work by Dillon et al. indicates that for the potentially attractive interiors of nanotubes to be accessed by hydrogen, the hemispherical caps on the nanotubes must first be removed [Dillon et al., 2000]. They found that sonication was an effective method of carrying out the tube-cutting, but this method also introduced metal impurity to the nanotubes as a result of decay of the sonication tip. This work is further discussed in the following section on Nanotubes with Metals.

Alternatively, Pradhan et al. employed strong acid that they believe induced reconstruction of the tube walls to form mixtures of pentagons and hexagons, the effect of which is to damage to the nanotube walls, providing another path for hydrogen to access interior adsorption sites [Pradhan et al., 2001]. The effect was to increase the level of storage at 77 K from 1 wt. % to 6.5 wt. %. Interestingly, Kuznetsova et al. observed by TPD that removal of residual C-O-H groups left at edge sites following the formation of defect sites by acid treatment enhances the adsorption of xenon within the nanotubes [Kuznetsova, 2000]. It may be inferred then that internal hydrogen adsorption may also be so enhanced, although no work has examined this possibility to date.

External adsorption studies, including this one, have focused on the possibility of potentially attractive sites existing between nanotubes within

bundles. These works generally found that effective storage levels could only be obtained at low temperature and high pressure, a regime where pure physisorption is expected [Ye et al., 1999; Pradhan et al, 2001]. Ye et al. was the first to suggest that hydrogen adsorbing between the tubes within a bundle explained the observed kink in the isotherm, shown in Figure 2-8. At lower pressures, the hydrogen is insufficiently active to penetrate the tube bundles, but the high chemical potential of the hydrogen at higher pressures is able to overcome the cohesive energy of the bundles and expose new surface area to adsorption. The possibility of chemical potential induced alteration of adsorbent morphology to enable penetration of adsorbed molecules into interlamellar, or in this case, intertube spaces is not new. This phenomenon has been observed for methane adsorption on coal with the use of electrical resistance strain gauges attached to blocks of coal [Menon, 1968].

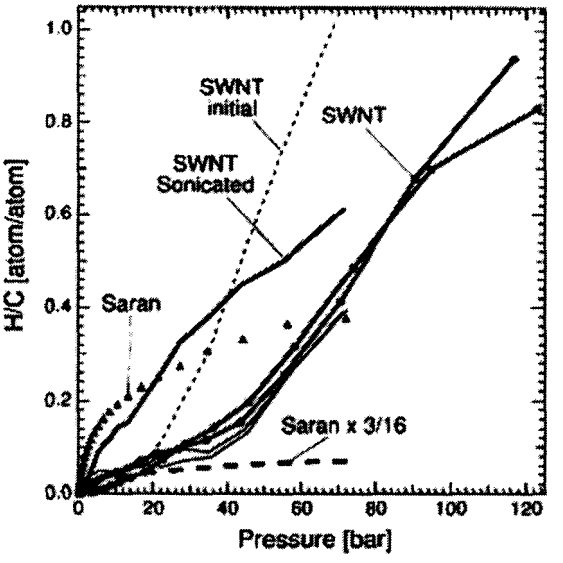

Figure 2-8. Hydrogen adsorption isotherms of single-walled nanotubes (SWNT) and unstructured high surface area carbon [Saran] at 80 Kelvin [Ye et al., 1999].

A more recent study by Cao et al. on blocks of aligned multi-wall nanotube bundles lends support to the idea that nanostructure morphology may be altered by the effects of high pressure [Cao et al., 2001]. In this instance, the authors observed by pore size measurement a decrease in the inter-tube spacing of aligned multiwall nanotubes upon testing to high pressure. They theorize that initially the intertube spacing of 3 to 100 nm are too large to effectively enhance adsorption, and not until the action of high pressure forces the adjacent tubes together are the high adsorption channels formed. Interestingly, the same group found that squeezing of the multiwall blocks is an irreversible process by noting that the pore size distribution following initial pressurization was shifted to smaller pores, whereas subsequent pressurization cycles had no effect [Zhu et al.,

2001]. The work of Chen et al. seems to support this result as by TDS, they found that hydrogen adsorbed by their blocks of aligned multiwall nanotubes was not released until the temperature was raised to 300°C [Chen et al., 2001]. The latter authors stress that the morphology of their samples is unique, however, in that the samples are not strictly concentric tubes, but instead are stacks of high-aspect ratio cones having an angle of 5°. As a result, their samples have numerous edges exposing thin channels of 3.4 Å through which hydrogen may be able to access the interior of the tubes/cones. Furthermore, they found that using concentrated acid to open the ends of the multiwall cones exposes the interiors and more than doubles the observed hydrogen adsorption from 5-7 wt. % up to 13 wt. %.

An important omission made by many studies on hydrogen storage of carbon materials is the behaviour under hydrogen loading as well as hydrogen discharge. Published results from volumetric tests either report *adsorption* results [Chambers et al., 1998], or *desorption* results [Ahn et al., 1998], while others claim that both were done, and yet fail to include these results that would lend strong support to their findings [Liu et al., 1999]. Similarly, TDS results give only desorption behaviour, whereas a variation, TGA is able to give both adsorption and desorption. An exception in volumetric studies is the work of Tibbetts et al. who did a survey of a number of carbon fibers and nanotubes [Tibbetts et al., 2001]. Unfortunately, their findings were among the more pessimistic results and found that for the most part, carbon samples adsorbed less than 0.1 wt. % at room temperature and pressures up to 35 atm. Although they

found some hysteresis, they attribute it to miscalibration of their experimental apparatus. Pradhan et al. also found no hysteresis whatsoever, on single-walled nanotubes tested to 15 atm at 77 K.

Several studies have attempted to quantify the amount of adsorption with the measured B.E.T. surface area [Nijkamp et al., 2001; Züttel et al., 2002]. Nijkamp et al. found that the relationship is not straightforward as it depends on whether the surface area exists as micropores (<2 nm) or as mesopores (>2 nm), presumably because the potential overlap within the smaller pores results in much larger adsorption. As a result, they found better correlation of hydrogen adsorption with the micropore volume than with the surface area. For carbon materials, the amount of hydrogen adsorbed at 77 K and pressures up to 1 atm amounts to between 215 and 515 ml (STP)/ml of micropore. For typical activated carbons reported by the authors as having an average micropore volume of 0.41 ml/g, this equates to between 1.8 wt. % and 4.2 wt. %.

Züttel et al. employed a novel electrochemical method of evaluating hydrogen adsorption by carbon nanostructures including single-walled carbon nanotubes and found good correlation between hydrogen storage and B.E.T. surface area [Züttel et al., 2002]. This value they report is 1.5 wt. %/1000 m^2/g.

A subtle discrepancy that exists among report findings in adsorbent systems is the time required to equilibrate at a given pressure. Yang and Yang point out that in reports reviewed by them, at both ambient and cryogenic temperatures, the hydrogen uptake is slow, and equilibrates after time spans of the

order of hours [Yang and Yang, 2002]. The authors suggest this is due to chemisorption since in all cases small amounts of residual metals are present in the samples that catalyze the dissociation of hydrogen and subsequent atomic adsorption. In contrast, Hwang et al. report saturation of carbon nanofiber samples after only 45 minutes at 120 atm. Tibbetts et al. dispute results that indicate significant amounts of adsorption after short periods of time due to the significant temperature changes that occur upon adiabatic expansion of a gas into an evacuate sample volume [Tibbetts et al., 2001]. As the latter authors demonstrate in their figure reproduced in Figure 2-9, what qualitatively they attribute to establishment of thermal equilibrium, other authors have attributed to adsorption events. Unfortunately, the results of Tibbetts et al. must also be viewed with some skepticism because they use samples of less than 1 gram in two different apparatuses having calibrated volumes of 307 ml and 1049 ml. Their reportedly observed adsorption of 0.05 wt. % on single-walled carbon nanotubes therefore is associated with a pressure drop of 1998 Pa, and 585 Pa in each apparatus, respectively. Although sensitive pressure transducers are available with this degree of accuracy (0.018 % full scale minimum and 0.016 % full scale minimum, respectively), with their reported room temperature fluctuations of 2-3°, and leak rates exceeding 0.002 MPa/hr, it is likely that what they are reporting is noise. Tibbetts et al. are critical of other's work for using sample sizes of less than 1 gram and yet they do the same with calibrated volumes far exceeding those

of others including that of the present work. Furthermore, although they carry out their tests for greater than 300 hours, they fail to report a saturation time.

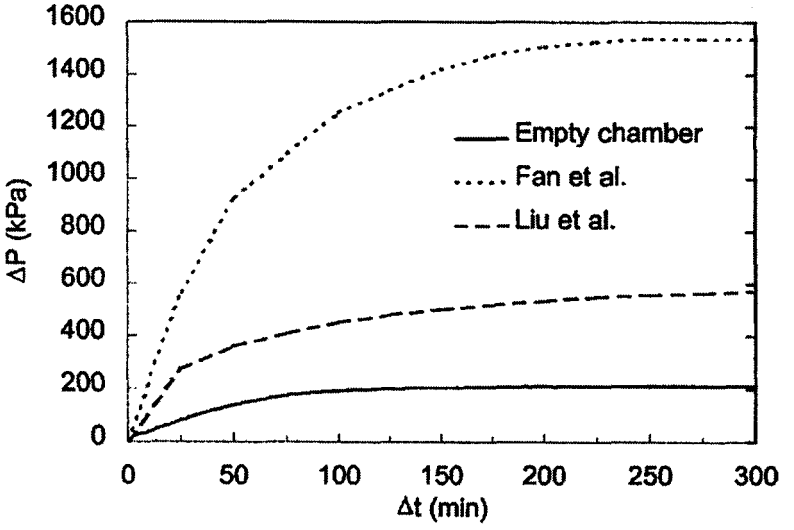

Figure 2-9. [Reproduced from Tibbetts et al., 2001]. The authors Tibbetts et al., show that the pressure change due to thermal equilibration following expansion of gas into an evacuated sample cell qualitatively appears to be the same as other authors attribute to adsorption.

2.2.2.2 Nanotubes with Metals

Recent studies have found that an increased level of hydrogen storage is achieved when the interaction of hydrogen with a nanostructure and the interaction of hydrogen with metals are combined [Chen et al., 1999; Hirscher et al., 2001; Dillon et al., 2000]. In some cases, repeated studies by different researchers found conflicting results which are attributed to the purity of the samples [Zandonella, 2001].

The new interface in these systems may impart a thermodynamic advantage to the adsorption properties of the nanostructure as suggested by the modeling work of Lueking and Yang on metal oxides and multiwall carbon nanotubes [Lueking and Yang, 2002]. Alternatively, the metal may significantly contribute to the overall level of storage, thereby creating a composite that stores hydrogen through more than one mechanism. Other studies have employed the use of transition metals to improve the performance of adsorption systems like alanates [Jensen et al., 1999], and nanocrystalline hydrides [Zaluska et al., 1999] although the mechanism is almost certainly different than that in physisorption systems. The electronic structure of transition metals in particular, consisting of unfilled d-orbitals, is expected to reveal an interaction of these elements with hydrogen that increases the amount of adsorption observed on nanostructures once a better understanding of the metal-nanostructure interaction is obtained.

The findings of Hirscher et al. suggest that it is difficult to distinguish between the effectiveness of a catalyst in adsorption systems due to the potential for composite behaviour [Hirscher et al., 2001]. As discussed in the section on metal hydrides, numerous transition metals have been observed to have varying degrees of hydrogen storage. These same metals are also used as catalyst particles in the production of carbon nanotubes. Hirscher et al. attempted to repeat an experiment done by Dillon et al. [Dillon et al., 2000] where single-walled carbon nanotubes were dispersed in a 5 M nitric acid bath using an ultrasonic probe. What the latter authors found was that the probe itself, which

was composed of a Ti-Al-V alloy, broke down thereby incorporating particles of alloy into the nanotubes. Upon filtration and exposing the sample to 1 atm of H_2, followed by testing using thermal desorption spectroscopy they found the sample had retained 6.5 wt. % of hydrogen. Hirscher et al., on the other hand, employed deuterium to increase the sensitivity of the TDS measurement, and observed that if a stainless steel probe was used instead of a titanium alloy probe, the sample retained less than 0.005 wt. %. Furthermore, they observed a hydrogen uptake of the pure titanium alloy alone of 3.5 wt. %, which corresponds to the uptake they observed on the combined nanotube-alloy sample.

An increase in adsorption of multi-walled nanotubes in the presence of metals was observed by Chen et al [Chen et al., 1999]. In this instance, the authors employed a chemical method of doping multi-walled nanotubes with lithium and potassium. They observed a very large hydrogen adsorption by the modified samples of 14 wt. % and 20 wt. % for lithium and potassium doping, respectively. Unfortunately, the method used to measure the hydrogen adsorption and release was thermogravimetric analysis (TGA), and as Yang later demonstrated, the amount adsorbed was likely closer to 2 wt. %, with the additional weight being due to water impurity present in the gas [Yang, 1999]. Even a small amount of water would strongly affect the measurement because the water molecule is much heavier than the hydrogen molecule.

2.3 Summary

Experimental Results	Material	Maximum Observed Storage	Experimental Conditions	Reference
	SWNT	0.1 wt. %	35 atm, 298 K	Tibbetts et al., 2001
	SWNT	0.1 wt. %	< 1 atm, 525 K	Hirscher et al., 2002
	SWNT	0.17 wt. %	100 atm, 333 K	Kiyobayashi et al., 2002
	SWNT & nanofibers	0.6 wt. %	60 atm, 300 K	Rzepka et al., 1998
	SWNT	0.6 wt. %	< 1 atm, 298 K	Züttel et al., 2002
	Carbon nanofibers	0.6 wt. %	100 atm, 77 K	Ahn et al., 1998
	SWNT	0.9 wt. %	298 K	Züttel et al., 2002
	Carbon nanofibers	1.0 wt. %	100 atm, 77 K	Ahn et al., 1998
	Carbon nanofibers	1.4 wt. %	120 atm, 298 K	Hwang et al., 2002
	Carbon nanofibers	1.96 wt. %	< 1 atm, 77 K	Nijkamp et al., 2001
	Aligned MWNT	13 wt. %	10 atm, 298K	Chen et al., 2001
	SWNT + Li & K	14 – 20 wt. %	< 1 atm, 400 K	Chen et al., 1999
	SWNT + Li & K	2 wt. %	< 1 atm, 298 K	Yang, 1999
	Aligned MWNT	2.4 wt. %	100 atm, 290 K	Cao et al., 2001
	Activated carbon	2.4 wt. %	100 atm, 77 K	Ahn et al., 1998
	MW carbon nano-barrels	2.9 wt. %	100 atm, 298 K	Johansson et al., 2002
	Aligned MWNT	3.4 wt. %	100 atm, 290 K	Zhu et al., 2001
	MW carbon nano-barrels	4.1 wt. %	100 atm, 77 K	Johansson et al., 2002
	SWNT	4.2 wt. %	100 atm, 300 K	Liu et al., 1999
	Nanoporous carbon	5.0 wt. %	60 atm, 77 K	Bénard et al., 2001
	SWNT	5.5 wt. %	< 1 atm, 77 K	Züttel et al., 2002
	SWNT	5-10 wt. %	< 1 atm, 290 K	Dillon et al., 1997
	MWNT	6.3 wt. %	146 atm, 298 K	Hou et al., 2002
	SWNT	6.5 wt. %	< 1 atm, 77 K	Pradhan et al., 2001
	Carbon nanofibers	65 wt. %	100 atm, 298 K	Chambers et al., 1998
	Carbon Nitride nanobells	8 wt. %	1 atm, 438 K	Bai et al., 2001
	SWNT	8.25 wt. %	70 atm, 80 K	Ye et al., 1999

Table 2-1. Summary of previous experimental findings on hydrogen storage by adsorption systems.

Table 2-1 is a summary of reported experimental findings on nanotubes and other adsorbents from the last five years. To highlight the discrepancy, the groups of Tibbetts, Rzepka, Liu and Dillon have all reported room temperature storage on SWNT. Within these cases the results are sometimes quite promising, and in others, they are quite discouraging. In none of these cases did the authors

demonstrate a plateau of adsorption versus pressure that would verify the storage capacity of the sample had been attained. Moreover, contrary to conventional understanding of adsorption systems, measurements done at higher pressures are, in some cases, less than those made in vacuum by 1-2 orders of magnitude. These seemingly inconsistent findings exemplify the confusion within published literature at this time.

3.0 Experimental Design

3.1 Isotherm measurement instrument

Several alternative experimental procedures can be used to evaluate the overall level of adsorption by a potential hydrogen storage material. Some of these methods, including Temperature Programmed Desorption (TPD), and Temperature Desorption Spectroscopy (TDS) generate information about the amount of desorption as the temperature is raised from a presumably very low temperature under high vacuum. More comprehensive methods of evaluation are able to measure both adsorption and desorption. These include Thermal Gravimetric Analysis (TGA), gravimetric analysis, and volumetric analysis. The latter two methods differ from the others by quantifying adsorption versus pressure and therefore evaluate hydrogen storage effectiveness in a way that mimics the likely operation of a successful hydrogen storage system. TGA, and other methods that measure adsorption by sample weight change alone are subject to error introduced by impurity more so than volumetric methods by themselves or gravimetric methods that use mass spectroscopy to complement the results. The adsorptive action of an impurity will increase the apparent overall level of adsorption in the case of a gravimetric measurement, but will decrease the

apparent level of adsorption in the case of the volumetric method. The reason is that the impurity will take surface sites on the adsorbent that would otherwise be available to hydrogen.

Two principal techniques for the measurement of gas adsorption by a solid sample at conditions of elevated pressure and moderate temperature were considered. These techniques include gravimetric and volumetric, and the relative merits have each have been previously reviewed [Robens et al., 1980].

There are numerous variations of the gravimetric technique, but in general, the adsorbent is suspended from a mass balance and the weight before, during, and after exposure to the gas is recorded. In alternative setups, the entire adsorbent chamber rather than the adsorbent is suspended from a mass balance. In both cases, compensation must be made for the buoyancy force experienced by the apparatus components, the sample, and the volume of the adsorbed molecules in the high-pressure fluid. Commercial balances are available that eliminate the error due to buoyancy via counterbalance, but none are currently available for pressures required in the current study without extensive, costly modification.

The volumetric apparatus measures the amount of gas adsorbed by a specimen contained in the sample chamber by recording the pressure drop that occurs on opening of the sample chamber valve. This permits a dose of gas at a known pressure and temperature to be exposed to the sample within the sample chamber. Accurate measurement of the volume of the dosing chamber and the

sample chamber permit the pressure drop to be related to the extent of adsorption of hydrogen by the sample using gas laws.

The main advantage of the volumetric method over the gravimetric method is that buoyancy does not affect the measurement. This advantage is particularly significant at high pressures due to the fact that the error in the buoyancy increases as the density of the gas increases. In spite of this, there are numerous examples of each method being employed over wide ranges of pressure and temperature.

A volumetric adsorption measurement apparatus was chosen for the present work due to its cost-effective flexibility in pressure and temperature.

A high-pressure volumetric adsorption measurement instrument was designed and constructed as shown in schematic in Figure 3-1. A volumetric apparatus is comprised of two calibrated volumes that are separated by a valve, one of which contains the sample. In its simplest operation, the first calibrated volume, referred to as the reference cell, is pressurized to a known pressure and temperature. The sample cell valve (SCV) is then opened, and the sample is exposed to the pressurized hydrogen. By recording the initial pressure drop and the pressure drop over time, the number of moles adsorbed by the sample can be calculated using gas-laws.

The sample cell is made up of all components exposed to the hydrogen gas up to the seat of the SCV. Two alternative designs of the removable sample cell were employed. The original sample cell, depicted in Figure 3-2, was machined

from 316 stainless steel bar stock. The seal is formed using a Viton o-ring, compressed by six radially symmetrical 3/8-inch high strength steel bolts. The sample cell is attached to the system using a Swagelok fitting on the integrally machined nipple. The drawback of this design is that it is limited to a temperature range suitable to the Viton o-ring. Other o-ring materials are available, but ultimately limited to between –20 and 350°C.

The second sample cell design, depicted in Figure 3-3, is more flexible in that all components are composed of 316 stainless steel. The sample is loaded via a resealable Swagelok VCR type fitting, which employs a silver plated stainless steel metal gasket seal. A seal is formed by tightening the large stainless steel nut and compressing the metal gasket between protrusions on either side of the sealing surface. Stock stainless steel tubing with an outer diameter of 0.25 inches, and a wall thickness of 0.034 inches connects the VCR sealed volume to the SCV. Gas-tight joints are formed using the standard double ferrule design manufactured by Swagelok. The reference cell is similarly composed of stainless steel tubing, but has a section of larger diameter tubing, giving a larger volume, thereby enabling higher pressure increments in a single step. In addition, the reference cell volume includes the internal volume of the pressure transducer, and dial pressure gauge.

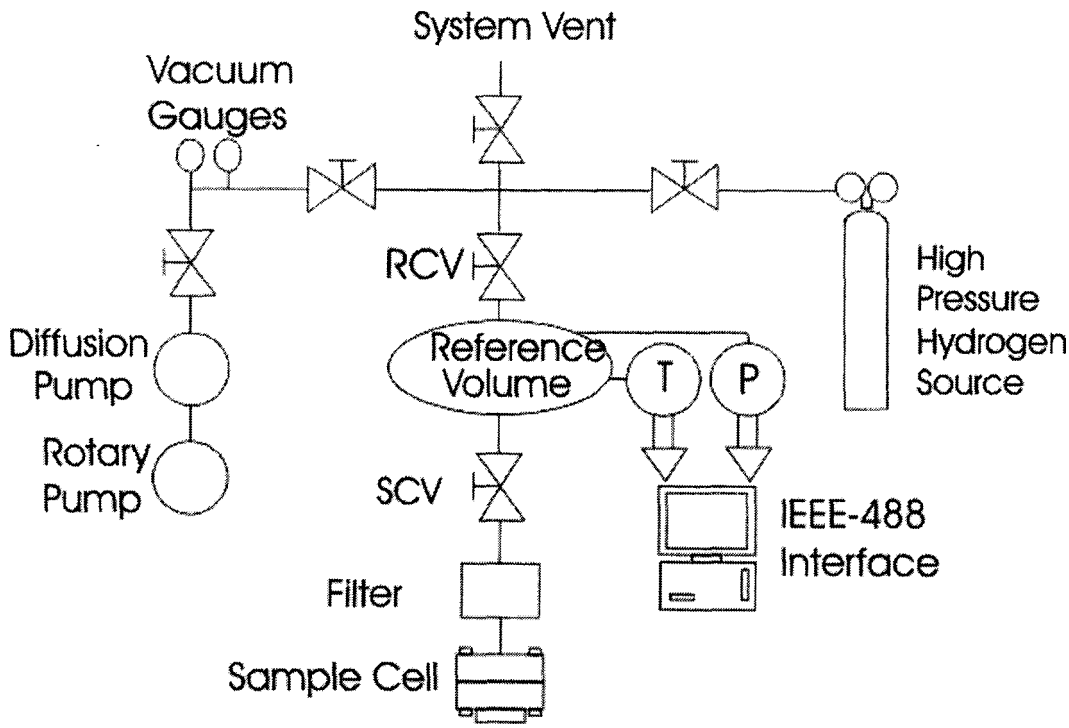

Figure 3-1. Schematic diagram of adsorption measurement apparatus.

The pressure transducer, manufactured by Druck, has a pressure range from 0-5000 psig (0-340 atm) and a rated accuracy of 0.08% full scale, including hysteresis. All wetted parts are composed of 316 stainless steel. A BK Precision 1635 DC Power Supply provides excitation voltage of 11.0 Volts with a measured fluctuation of less than 0.04% over a period of 24 hours. Pressure data is sampled using a Keithley 177 Microvolt Digital Multi-Meter connected to PC using an IEEE-488 interface.

A disadvantage of adsorption measurement methods that have high flow rates is the potential for sample loss during degassing. Care must be taken, therefore, in the design of the apparatus to ensure that pressurization and de-pressurization of the sample chamber is done at a slow, controlled rate. This can

be achieved with the use of a regulating valve at the inlet to the sample cell. Such a valve is employed in the apparatus depicted in the schematic diagram in Figure 3-1.

Furthermore, the leak-rate of the valves separating the reference cell from the sample cell (SCV), and the reference cell from the gas-line (RCV) are particularly critical. As a result, high quality valves manufactured by Whitey (HN Series Severe Service Needle Valves) with soft seats are used. The soft seats are made of Teflon, and were found to have a negligible leak-rate compared to stainless steel seats.

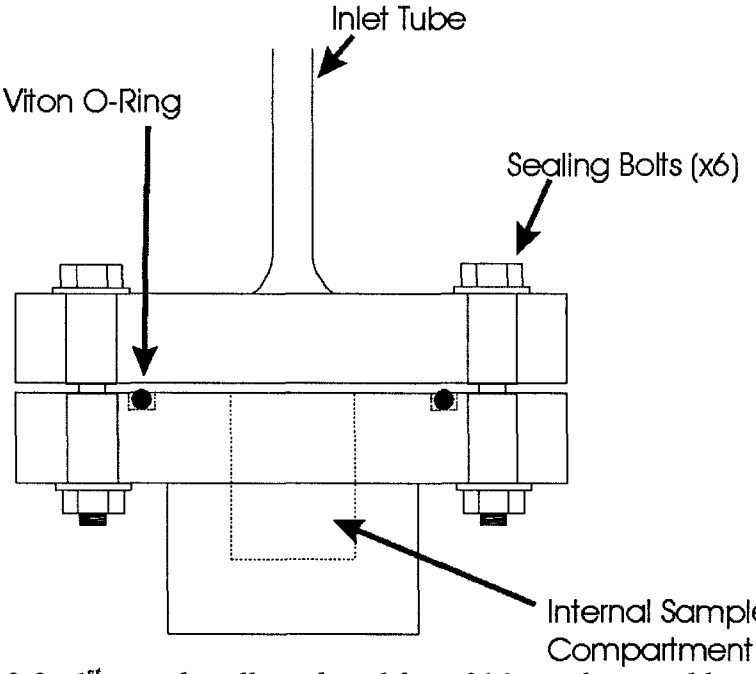

Figure 3-2. 1st sample cell machined from 316 stainless steel bar stock and sealed with a Viton o-ring.

The use of a filter at the entrance of the sample cell further minimizes possible sample loss, and two embodiments were tested in the present work. The overall surface area and volume of the filter must be minimized to avoid possible introduction of uncontrolled error into the experimental results. The original design employed the use of a fixed filter composed of two layers of fine iron-nickel alloy mesh (75μm) compressed within a Swagelok joint in the sample cell. Following the testing of various samples, the SCV was disassembled, and found to contain residuals of escaped sample. In addition, the hydride forming characteristics of these metals are unknown, and consequently may lead to inconsistent adsorption error. As a result, the alternative design depicted in Figure 3-3, uses a glass fiber filter material. The glass fiber filter performed better in sample retention, and published work by Nijkamp et al., shows that hydrogen is not strongly attracted to oxalic surfaces such as silica [Nijkamp et al., 2001].

The gas-line connecting the reference cell, hydrogen source, and vacuum apparatus is composed of stock 0.25 inch diameter 316 stainless steel tubing. A higher leak rate through valves and fittings may be tolerated in the gas-line. Valves used to isolate the gas-line from the high-pressure source, system vent, and vacuum system are manufactured by Autoclave Engineers (SW4071).

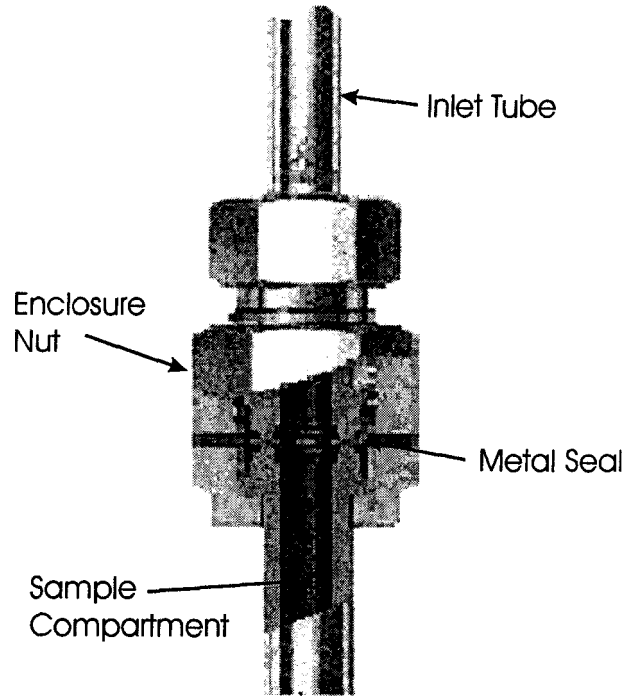

Figure 3-3. Stainless steel sample cell with metal seal.

Although the apparatus was originally designed for testing at room temperature, whereby the reference cell and the sample cell would be at the same temperature, it is possible to use the empty-cell calibration to test samples at other than room temperature. Figure 3-4 shows how the apparatus is used in the present work to test samples at sub ambient temperature. Similarly, Figure 3-5 shows how heat is applied to the sample cell, as used for sample degassing. The stems and seats of the valves used in the reference cell and sample cell are sealed using Teflon, which becomes hard at low temperature. For this reason, and because of size limitations of the sub-ambient bath, only a portion of the sample cell may be immersed in the bath.

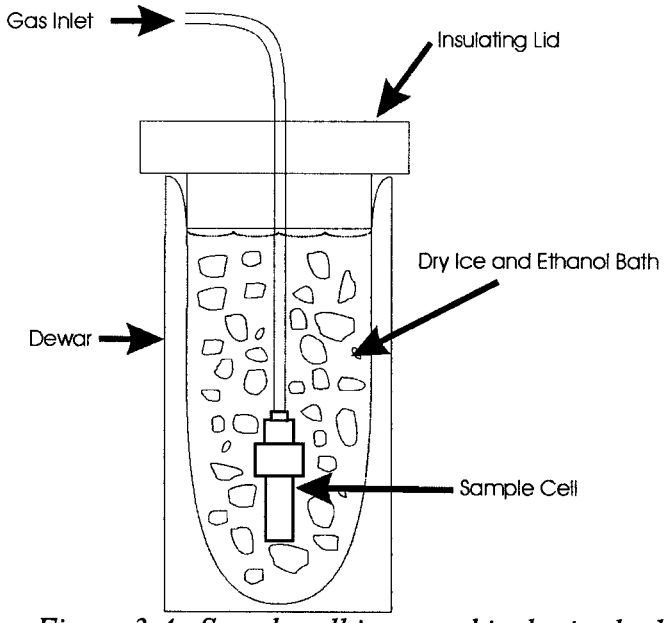

Figure 3-4. Sample cell immersed in dry ice bath.

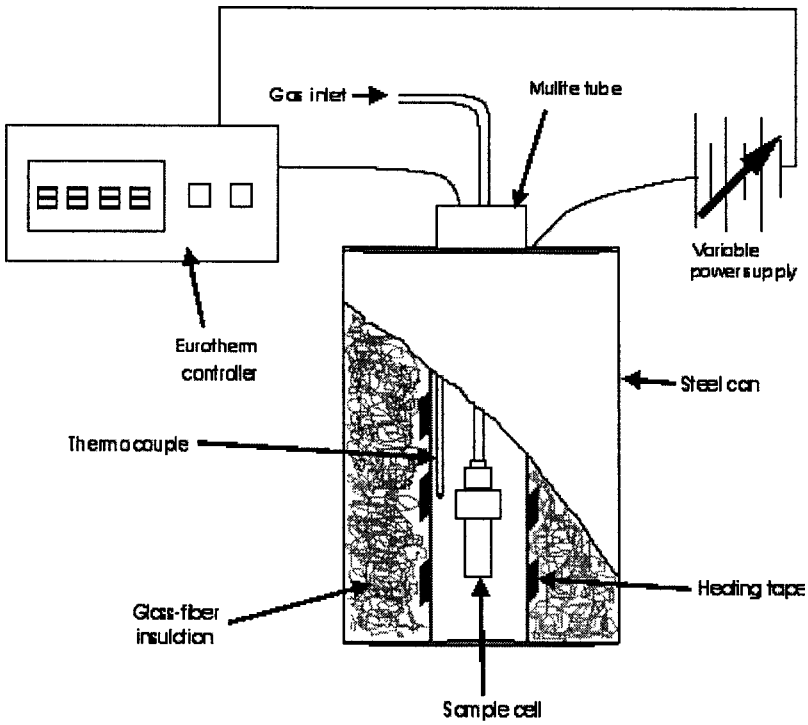

Figure 3-5. Heating system used for sample degassing.

Two alternative methods of evaluating volumetric data are possible. In the first method, pressure versus time data is obtained on the principle that when a dose of gas of known volume, pressure and temperature is admitted to a volume calibrated sample cell and the pressure drop is measured against time, gas laws may be used to convert the pressure drop to absolute adsorption. The second method is similar to the first, with the exception that the obtained pressure versus time data accumulated is compared to calibration data that was obtained without the presence of the sample.

In principle, the first method should give the correct isotherm and level of adsorption. However, the magnitude of the adsorption given by this analysis is quite different than if the data points are calibrated with an empty sample cell. This phenomenon has been attributed by Kiyobayashi et al. to systematic error which they were unable to identify. These authors propose compensating for this error by incorporating the sample cell volume as a function of pressure [Kiyobayashi, 2002]. A more effective way of compensating for this systematic error is to use the empty-cell calibration method. By repeating each pressure-step using an empty cell, the systematic error is the same and it is therefore possible to identify the adsorption by the sample separate from instrument effects.

For a series of pressure measurements, the following steps were applied to analyze the data using the empty-cell calibration method, as summarized in the flow chart of Figure 3-9. Sample analyzed data can be found in Table 3-1 and Figure 3-8.

Using the empty-cell calibration method,

1. *Pressure Measurement.* Pressures in mA are obtained from the pressure transducer. These are converted to pressure in psi according to:

$$P(psi) = \left[P(Amps) - 0.004(Amps)\right] \cdot \frac{F.S.(psi)}{F.S.(Amps)} + 14.69595 psia$$

$$P(psi) = \left[P(Amps) - 0.004(Amps)\right] \cdot \frac{5000 - 0}{0.020 - 0.004} + 14.69595 psia$$

The pressure transducer has a full-scale (F.S.) range of 0-5000 psi, corresponding to an output potential of 0.004 A to 0.020 A. The addition of 14.69595 psia is required to convert the measured gauge pressure to absolute pressure. Although the barometric pressure varies by typically 1%, this equates to a corresponding F.S. fluctuation of only 0.0003% and is insignificant relative to the rated accuracy of the pressure transducer (0.01% F.S.).

The accuracy of the pressure transducer was improved by quantifying the non-linearity in the gauge using a deadweight tester, as discussed in Section 4.1.2. The results of this calibration were used to adjust the milliamp output of the transducer prior to conversion to pressure units using the above equation.

2. *Temperature Compensation.* A picoammeter was used to record the ambient temperature from a K-type thermocouple. The output was calibrated to three

fixed temperatures, and found to vary linearly. For pressure measurements recorded with the SCV closed, for instance during setting of the reference cell pressure, the raw pressure readings from step 1 were normalized to the average room temperature of 294 K using the following expression, employing the use of the ideal gas law,

$$P_{294} = P_{RT} \cdot \frac{T_{294}}{T_{RT}} \qquad 3.1$$

In this expression, P_{RT} and T_{RT} are the recorded values of pressure and temperature, respectively. T_{294} is the normalized temperature of 294 K, and P_{294} is the equivalent pressure at the normalized temperature.

Although strictly valid only for an ideal gas, the room temperature varies by no more than 1.7%, and hydrogen varies from ideal gas behaviour by 25% at a pressure of 400 atm. As a result, this simplification to account for room temperature fluctuation introduces a relative error of 0.4% at the maximum pressure of the apparatus.

As mentioned previously, Equation 3.1 can be used to normalize pressure readings in which the SCV is closed. In addition, it may be used to normalize pressure data recorded when the sample is exposed to room temperature. In compensating pressure measurements taken with the SCV open in tests where the sample is exposed to 200 K, Equation 3.1 cannot be used as only the portion of the reference cell and sample cell that are exposed to ambient temperature will be

affected by fluctuations in room temperature. These pressure readings are normalized using the following consideration that takes into account the volume exposed to ambient conditions, and the volume exposed to test temperature.

If the sample cell is divided into *n* volumes to account for the transitional zone temperature gradient, then the overall number of moles in the system can be approximated using the ideal gas law as

$$n_{RT} = \frac{P_1 V_{SC}}{RT_{SC}} + \frac{P_1 V_{t1}}{RT_{t1}} + \frac{P_1 V_{t2}}{RT_{t2}} + \cdots + \frac{P_1 V_{tn}}{RT_{tn}} + \frac{P_1 V_{ref}}{RT_{ref}} \qquad 3.2$$

T_{SC} is the temperature of the sample test, and V_{SC} is the volume of the section of sample cell immersed in the temperature bath. V_{ref} is the volume of the reference cell which is exposed to ambient temperature fluctuations. V_{tn} are volumes obtained by approximating the smoothly varying transition temperature region between the sample test temperature and room temperature with a series of volumes and average temperatures. Figure 3-6 illustrates graphically how this approximation was made by measuring the external temperature of the apparatus at selected positions from the surface of the bath. Sections of the apparatus that are exposed entirely to room temperature must be fully corrected for fluctuations in room temperature whereas the section immersed in the fixed temperature bath are unaffected by these fluctuations. Sections in between will be affected to a less extent. This variation is accounted for by generating a curve as shown on the secondary axis in Figure 3-6 that is normalized to give a value of 1.0 at sections in

ambient temperature, and 0 at sections in the fixed temperature bath. Intermediate values provide a fraction with which in the sections in between may be modified. This fraction, denoted by f_{Tn}, is incorporated into the following equation for the moles at the corrected pressure. In other words, if the temperature of the room fluctuates higher than 294 by an amount ΔT, then an intermediate section of the transition zone will also fluctuate up, but only a fraction of the room temperature fluctuation, $\Delta T \cdot f_{Tn}$. If the new fixed room temperature is represented by $T_{294}=T_{ref}-\Delta T$, then the number of moles at the corrected temperature will be given by

$$n_{294} = \frac{P_2 V_{SC}}{R T_{SC}} + \frac{P_2 V_{t1}}{R\left(T_{t1} - \Delta T \cdot f_{T1}\right)} + \cdots + \frac{P_2 V_{tn}}{R\left(T_{tn} - \Delta T \cdot f_{Tn}\right)} + \frac{P_2 V_{ref}}{R(T_{ref} - \Delta T)} \qquad 3.3$$

An equivalent pressure at an arbitrarily selected fixed room temperature of 294 K is required that will represent the same overall number of moles as before. This can be calculated by equating 3.2 and 3.3, converting each volume to a volume fraction by dividing by $(V_1+V_2+V_3+V_4+V_5)$ and simplifying to yield

$$P_1\left(\frac{V_{fSC}}{T_{SC}} + \frac{V_{ft1}}{T_{t1}} + \frac{V_{ft2}}{T_{t2}} + \cdots + \frac{V_{ftn}}{T_{tn}} + \frac{V_{fref}}{T_{ref}}\right)$$

$$= P_2\left(\frac{V_{fSC}}{T_{SC}} + \frac{V_{ft1}}{\left(T_{t1} - \Delta T \cdot f_{T1}\right)} + \cdots + \frac{V_{ftn}}{\left(T_{tn} - \Delta T \cdot f_{Tn}\right)} + \frac{V_{fref}}{\left(T_{ref} - \Delta T\right)}\right)$$

where P_1 is the measured pressure at room temperature, and P_2 is the equivalent pressure when the reference cell is at a temperature of 294 K.

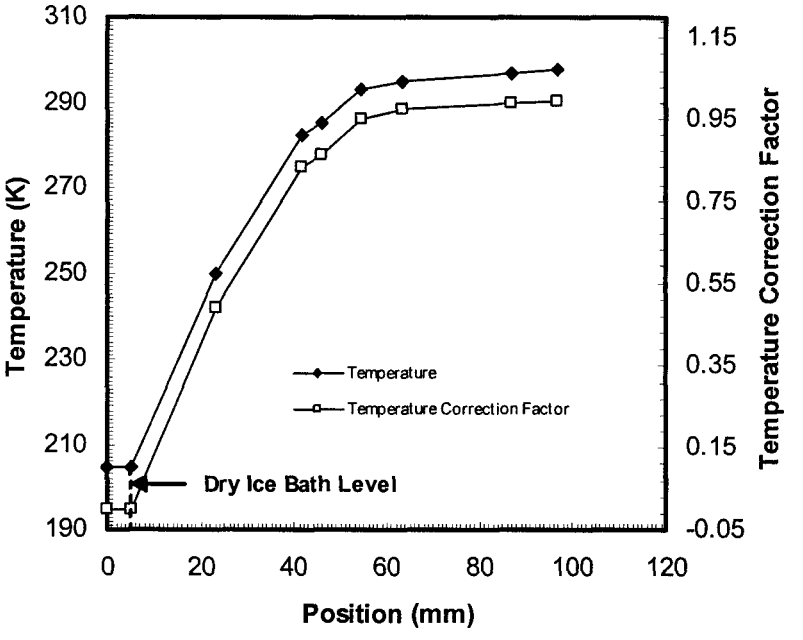

Figure 3-6. External temperature profile of the temperature transition above the dry ice bath.

3. *Calibration compensation.* Figure 3-7 depicts a plot of empty cell calibration data plotted with sample test data. The upper portion of the curve illustrates that because the calibration data is typically recorded after the sample test data is recorded, it is experimentally not possible to precisely match the calibration reference pressure to that of the sample reference pressure. Though not illustrated, when cumulative type measurements are taken, such that adsorption measured at each pressure step is added to that measured in the previous step, a similar difference exists between the pressure in the sample cells of the calibration run and the sample test run. Therefore when the SCV is opened, the final

pressure recorded will not only reflect the adsorption of the sample, but also the differences between the set points of the sample cell and reference cell for the two runs.

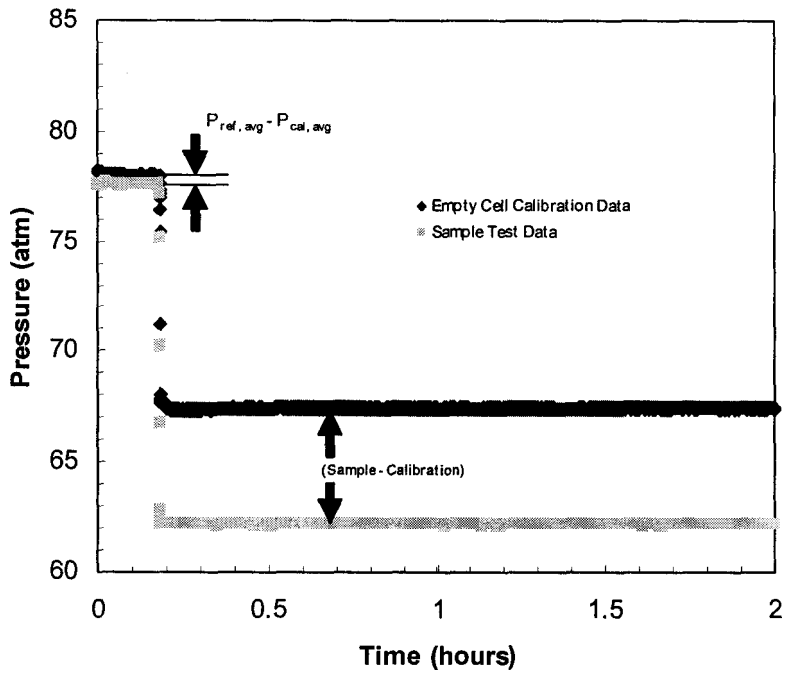

Figure 3-7. Illustrative example of pressure set-point compensation in evaluating empty-cell calibrated data.

These differences are eliminated in calculation as follows: the average of the last ten data points (corresponding to 100 seconds) prior to a pressure-step is converted to moles of gas using the van der Waals gas law. Each data point of the final pressure recording of each step is also converted to moles using van der Waals gas law, and from this is subtracted the difference in number of moles calculated previously. In the case of a cumulative-type measurement, this

correction is made for both the initial reference cell pressure and the sample cell pressure.

The use of the van der Waals gas law in calculating the number of moles, n, requires solving the following triatic equation,

$$\left(P+\frac{n^2a}{V^2}\right)(V-nb)=nRT \qquad 3.4$$

where P is the pressure in atmospheres, V is the volume in litres, R is the universal gas constant = 0.082057 $\left(\frac{litre\cdot atm}{mole\cdot Kelvin}\right)$, and T is the temperature in Kelvin. Symbols a, and b are van der Waals corrective terms for particle-particle interactions, and the finite volume of molecules in the gas phase, respectively. For hydrogen, a = 0.2461 $\left(\frac{litre^2\cdot atm}{mole^2}\right)$, and b = 0.0267 $\left(\frac{litres}{mole}\right)$ [Gaskell, 1981]. A value of n that satisfies Equation 3.4 can be found using Newton-Raphson iteration method. An initial estimate was found using the ideal gas law,

$$n=\frac{PV}{RT} \qquad 3.5$$

This was substituted into the Newton-Raphson equation,

$$n_{n+1}=n-\frac{F(n)}{F'(n)}$$

and iterated until the error function,

$$error=abs\left(\frac{n_n-n_{n+1}}{n_{n+1}}\right)<0.000001$$

where

$$F(n) = \frac{n^3 \cdot a \cdot b}{V^2} - \frac{n^2 \cdot a}{V} + n \cdot (R \cdot T + b \cdot P) - P \cdot V$$

and

$$F'(n) = \frac{n^2 \cdot 3 \cdot a \cdot b}{V^2} - \frac{2 \cdot n \cdot a}{V} + R \cdot T + b \cdot P$$

A Visual Basic code was written to perform the calculations described at each data point and assemble the data in a spreadsheet format, a sample of which is shown in Table 3-1.

4. *Visual Inspection.* It is not uncommon for inconsistencies in the sample or calibration data. These inconsistencies may include

i) rapid room temperature fluctuations due to passersby or sun-heating of the room,

ii) fluctuations in the level of the dry ice bath,

iii) slow leaks at elevated pressures.

To eliminate these potential sources of error, visual inspection is used as the last step to identify the level of adsorption or desorption attained at each pressure. A typical plot by which this is done is shown in Figure 3-8. The three curves plotted in this figure are taken from the spreadsheet output of the Data Analysis Code. On the primary y-axis, calibration pressures and sample pressures are plotted

versus time, and on the secondary y-axis is the wt. % adsorption calculated at each data point. The data in Figure 3-8 is from a test done at 200 K, and as a result, one of the inconsistencies present is the change in the level of the dry ice bath. In all cases, the bath was topped-up every 2 hours (+/- 5 minutes). The dashed line on the figure is a construction line denoting the level of adsorption taken from this plot. Note that although the level of the dry ice was set to precisely the same level every two hours, it appears that in both the calibration data, and the sample data that the pressure is falling. This may be due in part to a small leak, but in addition, it may take several hours for the dry ice bath to become consistent. As a result, note from the figure, that the pressure following the final two dry ice top-ups in both the sample and calibration data is very similar. Greater weight is given, therefore, to the position of the later data points, and calculated adsorption.

The data point taken from Figure 3-8 is 1775 psi and 1.23 wt. %. Depending on the visual interpretation of the data, these values may be different, but by no more than 0.5 % for the pressure or 5-10 % for the adsorption.

Occasionally a small leak appears in either the sample run or the calibration run at pressures of 225 atm and above. A simple correction is made prior to visual inspection in these cases. It is assumed in these instances that the majority of the adsorption occurred in the first several hours of the test. Therefore, a negative slope in either the sample or calibration runs in the final one or two hours of the test is indicative of a leak, and not due to adsorption events.

The slope of the pressure versus time in the final portion of the test is then calculated and the entire curve is corrected by adding an amount $m \cdot t$ to each data point where m is the calculated slope, and t is the time of each data point. Strictly, a leak would be expected to follow an exponential model, however because the leaks are relatively minor, and the test pressure is much higher than atmospheric pressure, a linear pressure drop is assumed.

The data analysis procedure is summarized by the flow chart in Figure 3-9.

50	0.0136689	0.011811	2455.83345	0.003032	292.6465285	2486.990596																
60	0.0166667	0.011803	2453.13345	0.003021	292.5884691	2485.128151																
70	0.0194444	0.011798	2451.57095	0.003024	292.5904853	2483.361059																
...	...	...	...	...	...	...																
Time (seconds)	Time (hours)	Pressure (V)	Uncorrected Reference Cell Pressure (psi)	Temperature (A)	Temperature (K)	Reference Pressure - Sample Run	Reference Pressure - Calibration Run	Prior Sample Cell Pressure - Calibration Run	Prior Sample Cell Pressure - Sample Run													
620	0.1722222	0.011782	2446.57095	0.003005	292.4573626	2459.475814	2449.536378	906.8079829	916.0569202													
630	0.175	0.011783	2446.86345	0.003003	292.44337 18	2459.90781	2449.107358	906.5481225	916.1043253													
640	0.1777778	0.011783	2446.86345	0.002987	292.4013384	2460.281419	2449.419702	906.5481225	915.9118792													
650	0.1805556	0.011782	2446.57095	0.00301	292.4924096	2459.181283	2449.361387	906.4882735	915.8270163													
660	0.1833333	0.011782	2446.57095	0.003011	292.499415	2459.122386	2449.457375	906.3965216	916.0027126													
670	0.1861111	0.011781	2446.25845	0.003013	292.5134259	2458.89051	2449.165686	906.3965216	916.1236644	Average Sample Reference Cell	Average Calibration Reference Cell	Reference Cell Difference	Average Sample-Sample Cell	Average Calibration Sample Cell	Sample Cell Difference							
680	0.1888889	0.011782	2446.57095	0.003012	292.5064205	2459.063491	2449.185686	906.4882735	915.7799516													
690	0.1916667	0.011782	2446.57095	0.003015	292.5274367	2458.868823	2449.399032	906.4433943	916.0935721													
700	0.1944444	0.011782	2446.57095	0.003007	292.4713934	2459.357903	2448.874086	906.4733131	916.1996078													
710	0.1972222	0.011781	2446.25845	0.003017	292.5414475	2458.455	2448.81575	906.3965216	915.9724319	2459.240253	2449.23024	-10.0100131	916.017428	906.479305	-9.5361235							
								Moles (ideal gas) →		0.171514787	0.170618658		0.03327898	0.03505073								
Discarded Arbitrary Data - Collected During Valve Opening								Moles (van der Waals) →		0.157807483	0.157223918	-0.00058357	0.03235597	0.03409202	0.00173605							
720	0.2	0.010053	1906.25845	0.003021	292.5884691	1815.579182																
						Corrected Pressure - Sample Run	Corrected Pressure - Calibration Run		vdW Moles - Calibration	vdW Moles - Sample Data	Moles Adsorbed	Wt % Adsorbed										
730	0.2027778	0.010043	1903.13345	0.003021	292.5884691	1908.546147	1937.143462		0.187633783	0.18617894	-0.00145485	0.32978217										
740	0.2055556	0.010041	1902.50845	0.003016	292.5344421	1909.076793	1936.634776		0.187587536	0.186136483	-0.00145105	0.32892071										
750	0.2083333	0.010041	1902.50845	0.003012	292.5064205	1909.203021	1936.824513		0.187804789	0.186147901	-0.00145689	0.3302433										
760	0.2111111	0.010042	1902.82095	0.003009	292.4854042	1908.811324	1937.078886		0.187627919	0.186184835	-0.00144308	0.32711433										
770	0.2138889	0.010042	1902.82095	0.00302	292.5624837	1909.264147	1936.962868		0.18761917	0.186153431	-0.00146574	0.33224864										
780	0.2166667	0.010043	1903.13345	0.003024	292.5904853	1908.451483	1937.363613		0.187953809	0.186170377	-0.00148343	0.33626042										
790	0.2194444	0.010042	1902.82095	0.003009	292.4854042	1909.811324	1936.761261		0.187599037	0.186184835	-0.0014142	0.32056744										
800	0.2222222	0.010042	1902.82095	0.003024	292.5904853	1908.137846	1936.919401		0.187813417	0.186142015	-0.0014714	0.33353354										
810	0.225	0.010043	1903.13345	0.003033	292.6535339	1908.167573	1937.269891		0.187645178	0.186144695	-0.00150048	0.34012548										
820	0.2277778	0.010042	1902.82095	0.003032	292.6485285	1908.885616	1937.237053		0.187642301	0.186119189	-0.00152311	0.34525486										
830	0.2305556	0.010043	1903.13345	0.003025	292.5974907	1908.419831	1937.395257		0.187656686	0.186167523	-0.00148916	0.33755959										
840	0.2333333	0.010044	1903.44595	0.003021	292.5884691	1909.8587	1936.761261		0.187599037	0.186207302	-0.00139173	0.31547472										
...	...	...	...	...	...	...	...	...	...	...	...	...										
21580	5.9944444	0.010074	1912.82085	0.003117	293.2418675	1916.228386	1929.975516		0.186981817	0.186783218	-0.0001986	0.04501796										
21590	5.9972222	0.010074	1912.82085	0.003105	293.1579228	1916.807362	1929.85812		0.186952939	0.186817479	-0.00013546	0.03070578										
21600	6	0.010074	1912.82085	0.003103	293.143812	1916.670546	1929.597958		0.186947468	0.186823191	-0.00012428	0.02817081										

Table 3-1. Sample output from Visual Basic Data Analysis Code for an empty-cell calibrated test to 1900 psi. "Reference" refers to pressure measurements taken with the Sample Cell Valve (SCV) closed. "Calibration" refers to measurements taken with an empty sample cell.

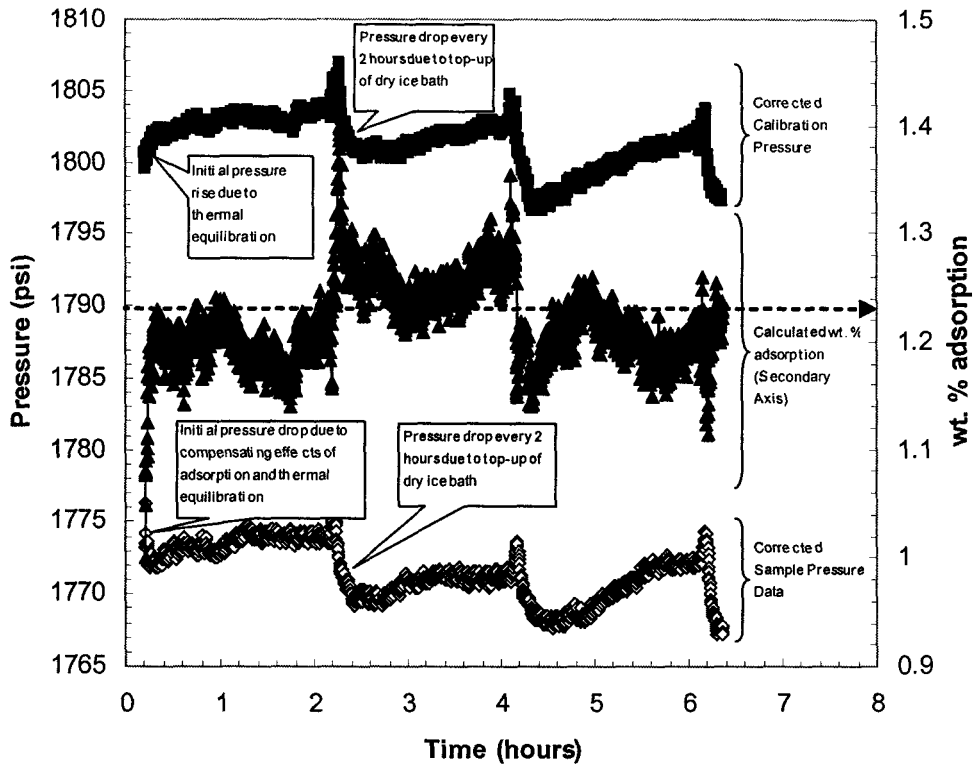

Figure 3-8. Illustrative example of the visual inspection process used to determine the wt. % adsorption at each pressure. Data used is from a test at 200 K and 1770 psi, in which a dry ice bath was used to cool the sample. Dashed line indicates the adsorption level taken from the plot.

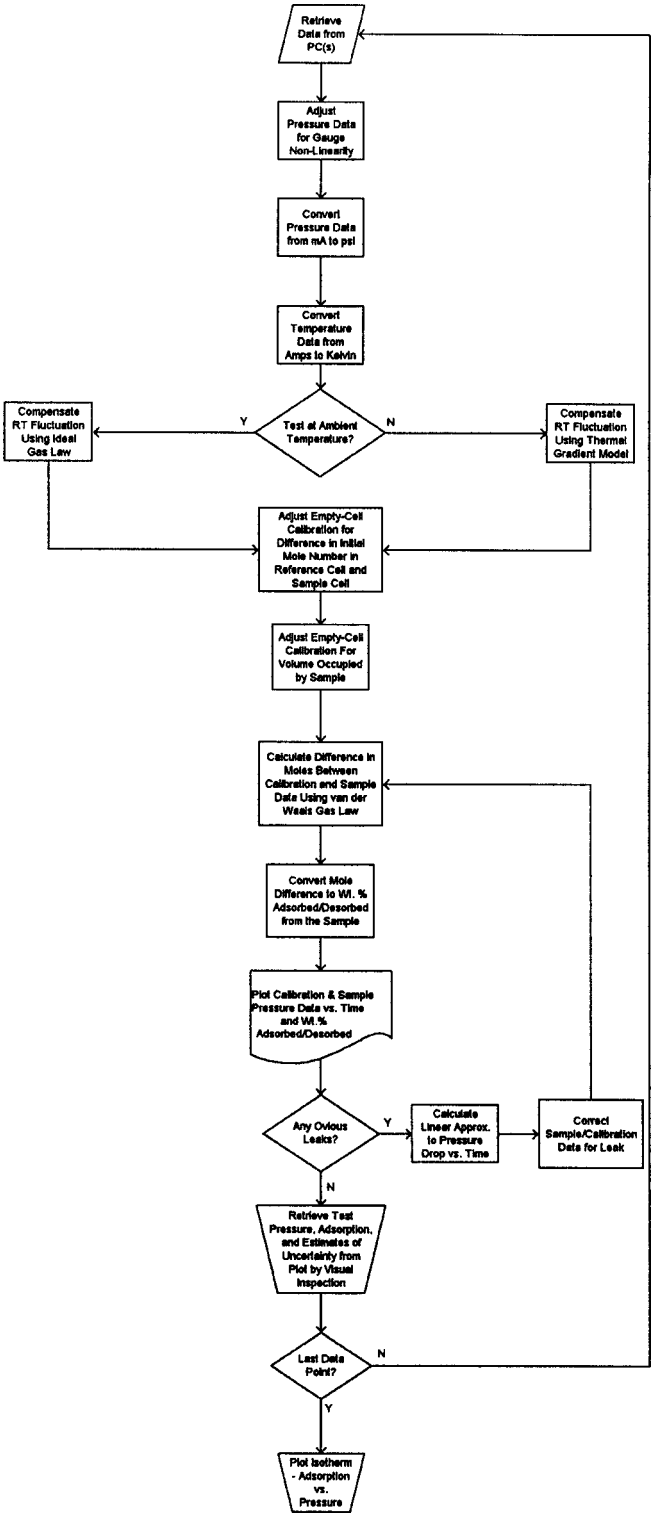

Figure 3-9. Data analysis summary.

3.2 RF Sputtering

Vanadium was deposited on samples of SWNT using RF-sputtering. A Randex model 3140 sputtering system was used, and deposition rate and thickness were monitored using an Inficon thickness monitor. In addition, a new glass slide was partially masked and placed adjacent the powder substrate for each test to verify the deposition thickness reported by the monitor. Thickness measurements were made on the glass slide using a profilometer. However, because the powdered sample will experience different coverage than the planar glass surface, the glass surface gives only an arbitrary measure of the amount of material deposited. Therefore, low magnification SEM and EDX were used to attempt to quantify the metal presence.

A schematic diagram of the deposition process is shown in Figure 3-10. In this sputtering system, the vanadium target is situated above the sample which is contained in a glass or aluminum dish and placed on the substrate table. The target is connected to a negative radio-frequency (RF) voltage supply. A large diameter diffusion pump is used to evacuate the deposition chamber to 2-5 x 10^{-6} Torr, after which high-purity argon gas is introduced to the system to provide a medium in which a glow discharge can be initiated and maintained.

When the glow discharge is started, positive ions strike the target plate and remove mainly neutral atoms by momentum transfer, and these condense into thin films. In addition, other particles and radiation, including secondary electrons and ions, desorbed gases, x-rays, and photons are produced at the target, though not in

significant quantities. The electrons and negative ions are accelerated toward the substrate platform and bombard the sample and the growing film. It is possible to apply a bias potential to the substrate table to divert some of the positive argon ions to the sample table. The effect of this is to redistribute and thereby improve the uniformity of the deposited material. The impact of energetic particles involves loss of energy as heat, so the target, substrate table, and thickness monitor are water cooled.

It is possible to sputter using a DC voltage, but the use of RF voltage has certain advantages. At an applied AC voltage having a frequency above 50 kHz, (RF sputtering is generally done at 5-30 Mhz) electrons oscillating in the glow space acquire sufficient energy to cause ionizing collisions, thereby reducing the dependence of the discharge on secondary electrons. In addition, the electrodes are not required to be electrical conductors because RF voltage can be coupled through any impedance. Therefore, using RF, it is possible to sputter any material, including metals, ceramics and polymers.

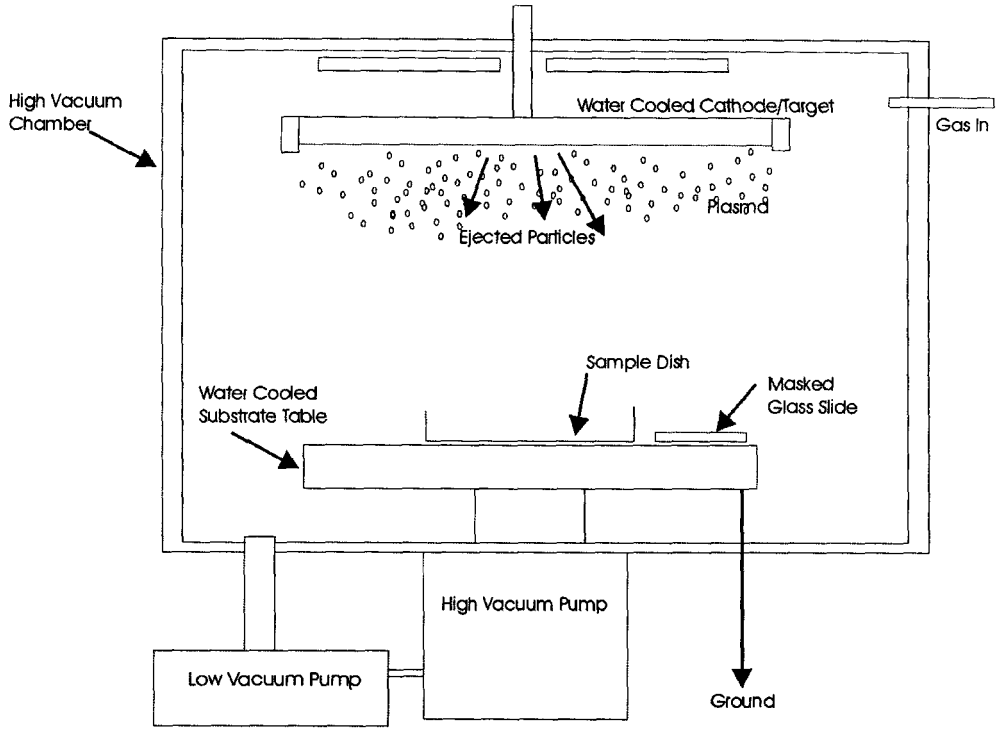

Figure 3-10. Schematic diagram of sputter deposition process.

3.3 *In situ* Resistance Measurement

High pressure electrical feedthroughs manufactured by Conax-Buffalo were used in a modification of the adsorption measurement apparatus to allow measurement of resistance and temperature while adsorption was taking place at high pressure. Resistance data was taken using a Hewlett-Packard 3478A multimeter and sampled at the same time as pressure and room temperature data through the PC shown in Figure 3-1. Simultaneous measurement of sample temperature was taken using a K-type thermocouple embedded within the sample and recorded using a Gamry Instruments CMS 100 electrochemical analyzer on a second PC.

The modified sample cell is shown in Figure 3-11. For clarity the sample cell is depicted removed from the system and therefore the sealing surface where the sample cell joins the instrument is the top surface on the diagram. The electrodes are 0.25 mm strips of copper having dimensions of 9 mm x 27 mm and are separated by a distance of 3 mm by a Teflon bar extending the length of the electrodes. The electrodes and Teflon spacer are buried within the loosely packed sample, and therefore electrically contact the sample on either side of the spacer and on the outside surface of the electrodes. The sample and electrodes are electrically insulated from the sample cell by a glass test tube having an outside diameter almost the same as the inside diameter of the sample cell. The sample is covered by loosely packed Teflon tape to reduce disturbance and loss through gas turbulence and vacuum application.

Teflon coated wires are soldered to the outside surface of the electrodes and to the electrical feedthroughs. Though not shown in the Figure, the wires are individually shielded by braided copper wire in contact with the inside of the tubing and fittings making up the remainder of the stainless steel sample cell. Also not shown is a thermocouple which is inserted into glass capillary tubing open at both ends, and buried within the sample.

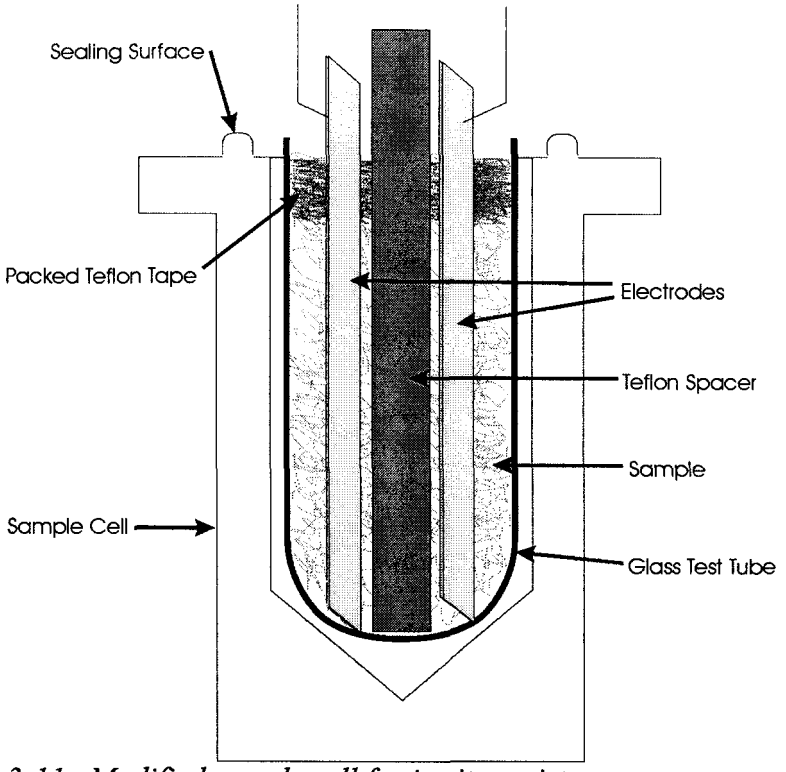

Figure 3-11. Modified sample cell for in situ resistance measurements.

3.4 Additional Characterization Techniques

3.4.1 Electron Microscopy

Sample structure and impurities were evaluated using electron microscopy in the Brockhouse Institute for Materials Research. High resolution TEM (JEOL 2010E) with EDX mapping were used to examine the bundle morphology as well as the size and distribution of impurities. Low resolution SEM (Philips 515) with EDX mapping was used to evaluate the distribution of deposited vanadium over the sample.

3.4.2 Surface Area Analysis

Brunauer, Emmett, and Teller (BET) surface area and pore size analysis was performed on the samples before and after exposure to high pressure to look for irreversible changes to the sample morphology. Measurements were taken using nitrogen at 77 K using a Quantachrome Autosorb-1 analyzer.

The BET method of surface area analysis estimates the surface area based on the number of adsorbed nitrogen molecules required to cover the adsorbent surface with one monolayer. Continued addition of gas molecules beyond the formation of a monolayer leads to gradual stacking of multiple layers on top of each other. At the same time, capillary condensation occurs according to the Kelvin equation (Equation 2.1). Measurement of the adsorbed volume of gas at a number of equilibrium pressures allows the determination of the pore size distribution via computational methods applied to this equation.

Unlike the hydrogen adsorption measurements done on samples at temperatures close to ambient in this study, the temperature of the BET measurement is close to that of the boiling point of the gas used. Therefore the formation of a complete monolayer and even multilayers in a BET test is virtually guaranteed because the saturation vapour pressure of the gas is only 1 atm. Beyond this point, the gas condenses with or without the sample presence.

4.0 Results and Discussion

4.1 Instrument Calibration

One of the principle objectives of this study is to solve the standing problem of uncertainty in hydrogen adsorption on single-walled nanotubes. To achieve this requires careful calibration of the measurement apparatus, and familiarity with the behaviour of the system in various measurement conditions. As a result, a number of calibration procedures were performed on the system prior to testing.

4.1.1 Volume Measurement

Of foremost importance for use of the adsorption measurement instrument for quantitative evaluation of hydrogen storage is the measurement of the volume of the sample and reference cells. The volume of the sample cell was measured by weighing the mass of water required to fill it. The dry disassembled fittings were first weighed, after which the sample cell was assembled, filled with water and evacuated to eliminate air-pockets, as shown in Figure 4-1, and then weighed again. In the figure, the sample cell is connected by vacuum hose to the lower outlet of a 3-way glass laboratory manifold. The other two junctions are

separated by valves and vacuum hose from a reservoir of distilled water and a mechanical vacuum pump. As the vacuum is applied, air is drawn out of the sample cell, and is subsequently replaced by water from the reservoir. The vacuum expands small bubbles that are trapped in small corners within the joints of the sample cell, allowing them to escape to the surface. The glass of the manifold allows observation of the evolution of air bubbles from the sample cell inlet. The water filling of the sample cell was allowed to proceed for approximately 30 minutes after which time the evolution of bubbles decreased substantially. The sample cell was then disconnected from the vacuum tube and exposed to atmosphere prior to closing the sample cell valve. The atmospheric pressure and temperature at time of closure was recorded and the outside of the sample cell volume was carefully dried prior to weighing. The density of the water was taken from tables published in the ASTM standard test E542-94, Standard Practice for Calibration of Laboratory Volumetric Apparatus. The entire procedure was repeated, resulting in values of 9.994 ml, and 9.978 ml. Since great care was taken to remove the water from the outside of the sample cell, the difference in the two measurements was taken to be due to air bubbles trapped inside the sample cell. As a result, the higher measurement was taken to be the true volume.

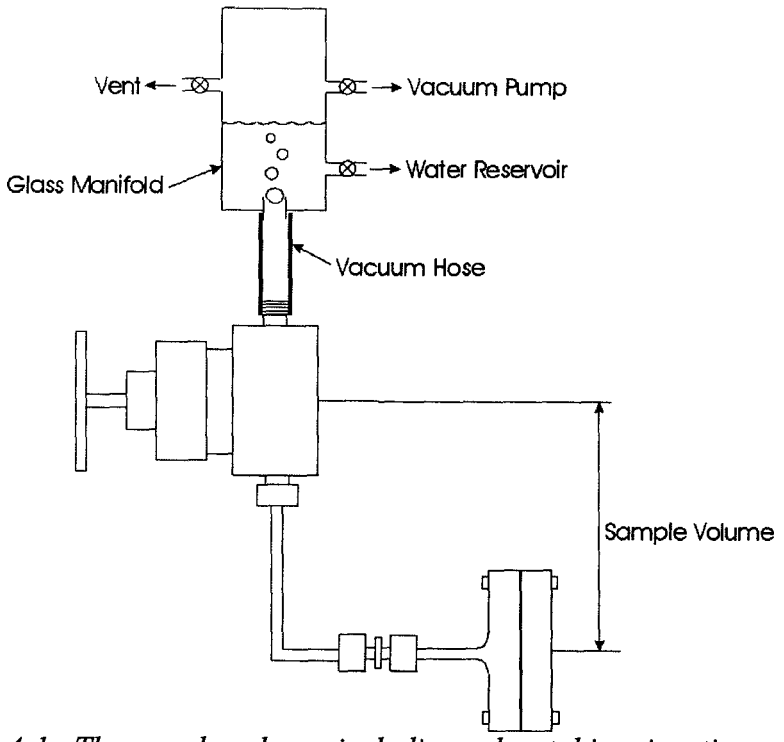

Figure 4-1. The sample volume, including valve, tubing, junction and sample cell was measured by filling with water, using a vacuum to eliminate air pockets.

Ideally, the reference cell volume could also be measured using this method. However, as each cell comprises numerous stainless steel fittings, valves and tubing made primarily of stainless steel the mass is too large for most sensitive laboratory balances. A Mettler PM1200 balance having a load capacity of 1200 grams with a sensitivity of 0.001 grams was sufficient to measure the mass of sample cell and water. The reference cell was too heavy to allow volume measurement using this method, and as a result, the volume was measured instead by gas displacement.

Volume measurement by gas displacement employs operation of the assembled adsorption measurement apparatus in the manner in which it is used to measure adsorption with the assumption that no adsorption takes place on the vessel walls. This measurement is often done using inert gases such as helium and argon to perform gas volume measurements. However, Malbrunot et al. found that this assumption can lead to significant error due to helium adsorption [Malbrunot et al., 1997]. As a result, hydrogen was used to measure the volume in this study with the understanding that while hydrogen may tend to adsorb more that inert gases, the adsorption should be similar for both volume calibration and sample testing.

In this method, the reference cell was pressurized to a known pressure and temperature, after which the sample cell valve was opened and the pressure and temperature again recorded. From prior knowledge of the volume of the sample cell, the ideal gas law was used to calculate the volume of the reference cell. To reduce error introduced by use of the ideal gas law, the volume measurements were taken at low pressures, where the gas behaves close to ideality. The measurements were repeated three times at 500 psi (34 atm) and three times at 1000 psi (68 atm), as summarized in Table 4-1.

	Trial Pressure (psi)	Volume (ml)
1	500	25.084
2	500	25.112
3	500	25.103
4	1000	24.449
5	1000	24.314
6	1000	24.298
	Average	24.726
	Standard Deviation	0.412

Table 4-1. Results summary of volume measurement of the reference cell.

4.1.2 Pressure Transducer Calibration

The transducer used to conduct pressure measurements in the apparatus is specified by the manufacturer to be linear within 0.1% of full scale capacity of 5000 psi, including hysteresis. To illustrate this accuracy, an absolute error of 5 psi in measuring the pressure of the reference cell, followed by 5 psi error in measuring the pressure of the sample cell after opening the sample cell valve results in an RMS error of approximately 0.26 wt. % for a sample size of 0.45 grams. This significant uncertainty is reduced by accounting for the non-linearity of the transducer. A deadweight calibrator translates fixed loads into a known oil pressure on the transducer and was used to measure this non-linearity, the results of which are shown in Figure 4-2. The deviation of the transducer was modeled using a power-series trendline, and corrected for in the Visual Basic analysis code.

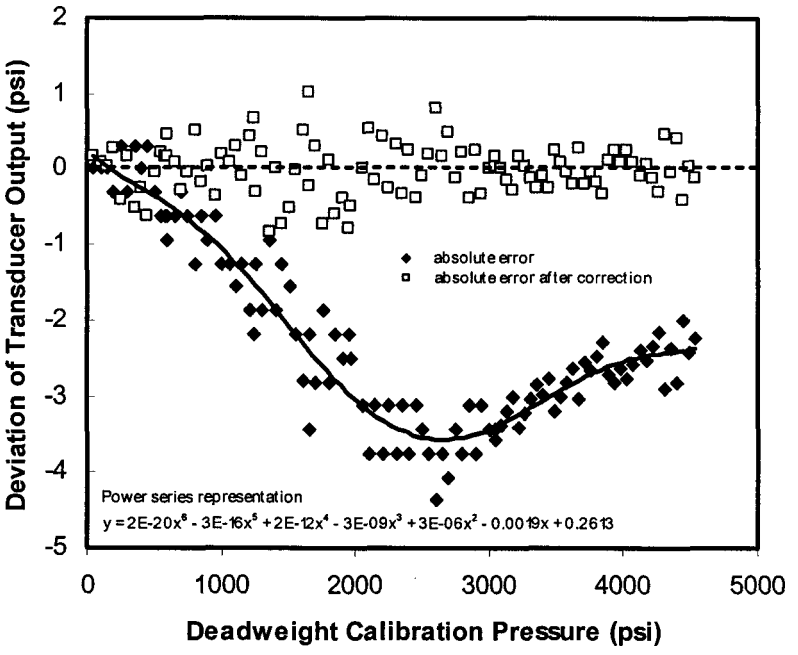

Figure 4-2. Non-linearity in the pressure transducer revealed by deadweight calibration.

4.1.3 Absorption on Standard Sample

Once the apparatus was constructed and the volume calibration complete, it was necessary to evaluate the system's ability to quantify the hydrogen uptake of a known sample. There are no readily available hydrogen *adsorbing* standards, as in many cases published data is questionable. As mentioned in Section 2.2.2, this is due to sensitivity to impurities, and subtle microstructural differences. A better calibration standard is a hydride-forming metal or alloy that adsorbs a known quantity irrespective of its morphology and presence of impurities. Lanthanum-nickel (La-Ni) is readily available, and its hydrogen absorption characteristics well known. It adsorbs only 1.5 wt. % [D.O.E. Hydride Database],

which is small enough to evaluate the resolution of the apparatus. An advantage of this particular hydride-forming material is that it forms the hydride phase at room temperatures, and relatively low hydrogen pressures only slightly above atmospheric with no activation. Other hydride materials often require high vacuum and thermal cycling to several hundred degrees Celsius, the purpose of which is to fracture any passivating surface layer by thermal expansion mismatch.

For calibration purposes, the La-Ni calibration sample was chosen to be less than 1 gram to be representative of the nanotube samples to be tested. The pressure versus time data collected is plotted in Figure 4-3. Although high pressure is not required to initiate the hydride forming reaction, for purposes of evaluating the apparatus, a mid-range pressure of 87 atm was used.

Upon initial opening of the sample cell valve, no adsorption occurs as a result of the thin passivating layer. After approximately 1 hour at 87 atm, the formation of the initial hydride phase is accompanied by a volume change which fractures the passivating layer, enabling the hydrogen to penetrate the sample and the hydride phase to form completely. Using the ideal gas law for simplicity, a pressure drop of 3.5 atm in a total volume of 34.7 ml equates to

$$\frac{PV}{RT} = \frac{(3.5atm)(0.034\ell)}{(0.0821\ell \cdot atm/mol \cdot K)(294K)} = 0.0049 \text{ moles or for a sample size of}$$

0.88338 grams, a wt. % adsorption of

$$\frac{(0.0045mol)(2.016g/mol)}{\left[0.88338g + (0.0045mol)(2.016g/mol)\right]}100 = 1.1 \text{ wt. \%}$$

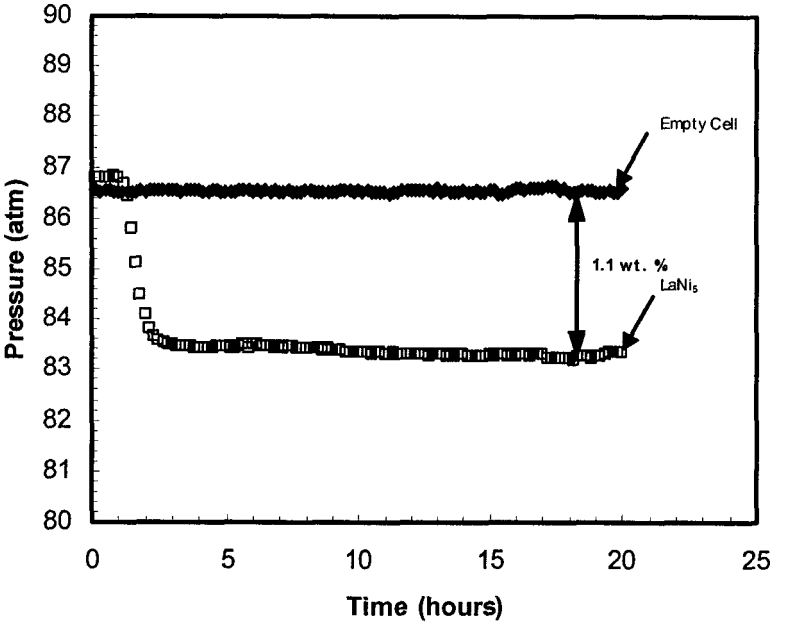

Figure 4-3. Pressure versus time data from Lanthanum-Nickel calibration. The pressure drop associated with the formation of the hydride phase corresponds to adsorption of 1.1 wt. % hydrogen. Sample size is 0.88338g.

There may be several reasons for this value differing from the literature value of 1.5 wt. % for a lanthanum-nickel alloy [D.O.E. Hydride Database]. It is not likely that it is due to miscalibration of the volume of the apparatus. The reason for this is that the measurements were done on the first sample cell and the standard deviation of the volume measurements on that cell is 0.48 ml. A difference in volume of 0.5 ml gives a difference of only 0.02 wt. % in adsorption at this pressure. A more probable explanation is that the sample of lanthanum-nickel alloy used in this test, having a -100 mesh size (roughly 149 μm) was too finely divided to ensure that the entire sample had hydrided. Some of the fine

pieces of the sample may have hydrided, while others did not due to variations in the shape or thickness of the passive layer. If the sample had been made up of larger pieces, it is probable that once the hydrogen had penetrated an alloy piece, the entire piece would be hydrided. Furthermore, the surface area of the finer particles is large and there is likely a significant quantity of surface oxide or hydroxide that contributes to the mass of the sample, but not the hydrogen uptake. In hindsight, larger particles would have been more effective at calibrating the quantitative capability of the adsorption measurement instrument. The low value of hydrogen uptake measured by this test therefore sets a limit to the accuracy of the system.

4.2 Investigations on Unpurified SWNT – Preliminary Results

A preliminary study of adsorption of hydrogen under high pressure was done on unpurified carbon nanotubes procured from Carbolex, Inc. (Lexington, KY). Transmission electron microscopy (TEM) was used to examine the nanotube samples, including geometry, and purity. In addition, electron dispersive x-ray analysis (EDX) was used to identify the presence of residual catalysts in the samples as received from the manufacturers. Adsorption of nitrogen at 77 K was used to determine the BET surface area, and pore structure before and after exposure at high pressure to look for irreversible changes to the sample morphology. RF bias-sputtering was used to deposit vanadium on the sample to assess the effect of metals on adsorption properties of nanotubes.

Scanning electron microscopy (SEM) and EDX were used to assess the uniformity of the deposit on the sample.

The TEM micrograph of Figure 4-4 depicts the sample received from Carbolex prior to testing or any modification. The material was produced using an electric arc, and is reported by the manufacturer to contain between 0.5-0.6 volume fraction of carbon nanotubes. No purification was done following the manufacturing process, and as a result, the material is expected to have significant leftover metal catalyst particles including yttrium and nickel.

The images shown are not representative of the entire sample, but rather were carefully selected to show nanotube bundles. This sample was largely comprised of a mixture of amorphous carbon, graphite, and residual catalysts, as seen in the lower left side of Figure 4-4a, and the right side of Figure 4-4b. The width of the bundles shown is between 10 and 20 nm, and they contain approximately 50-100 individual nanotubes.

Figure 4-5 shows EDX results on a section of bulk impurity. From the element maps of nickel and yttrium, the respective particle sizes for these impurities are 10-40 nm and < 1 nm. In several nanotube bundles, including that of Figure 4-4b, a nickel particle was observed enclosed within carbon at one end or at the junction of several bundles.

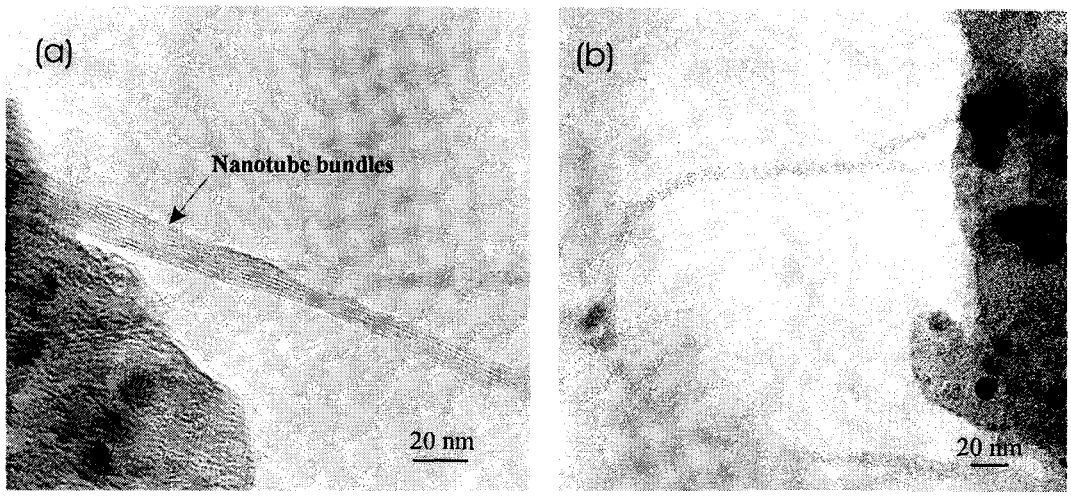

Figure 4-4. TEM micrographs of unpurified sample from Carbolex.

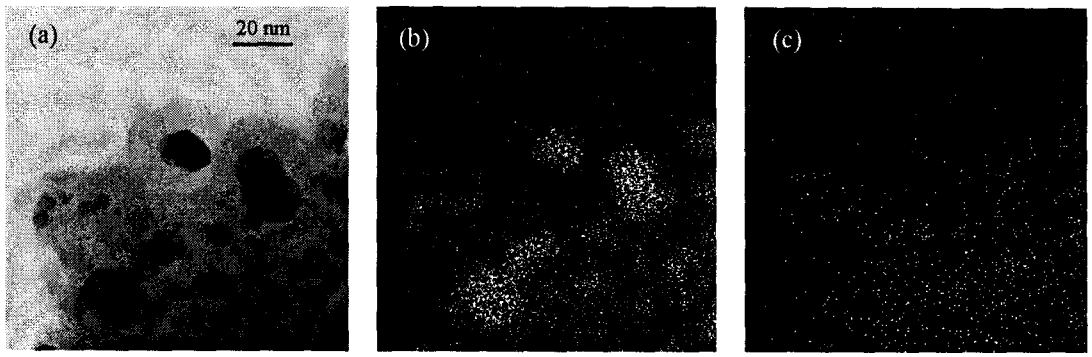

Figure 4-5. EDX analysis reveals distribution of impurities. (a) Transmission electron image, (b) Nickel x-ray map, (c) Yttrium x-ray map.

Hydrogen adsorption behavior was assessed on the newly constructed and calibrated volumetric adsorption apparatus shown in schematic in Figure 3-1. In this preliminary test, isotherms were obtained as described in Section 3.1 with several notable exceptions. The isotherms in this test were obtained by first applying high vacuum without heating for 12 hours, and then by applying increments of pressure and evaluating the pressure drop at each increment for a

period of 12 hours. The total adsorption at each pressure was therefore a summation of all preceding pressure increments. As a result, the error in each adsorption measurement is also cumulative and therefore the adsorption at high pressures may be deviated somewhat from the actual adsorption. Furthermore, in this measurement, to simplify calculation of adsorption, the sample cell was assumed to be entirely immersed in the dry ice bath. Consequently, the adsorption may deviate in magnitude from actuality. However, because each measurement was repeated using an empty sample cell, and the adsorption attributed to the difference between the two, the profile of the isotherm is expected to be accurate.

Since the apparatus had not been used for adsorption measurement prior to these tests, its behaviour was unfamiliar, and the level of uncertainty in the measurements was unknown. Therefore, these preliminary high pressure measurements were done with the sample at dry ice temperature. It was expected that the adsorption, and therefore the measured response would be higher in this regime than at room temperature.

The adsorption isotherm for the unpurified sample at the measured bath temperature of 200 K is plotted in Figure 4-6. The sample adsorbed very little (<0.6 wt. %) below 130 atm, beyond which a change occurred that allowed a much more rapid uptake of hydrogen.

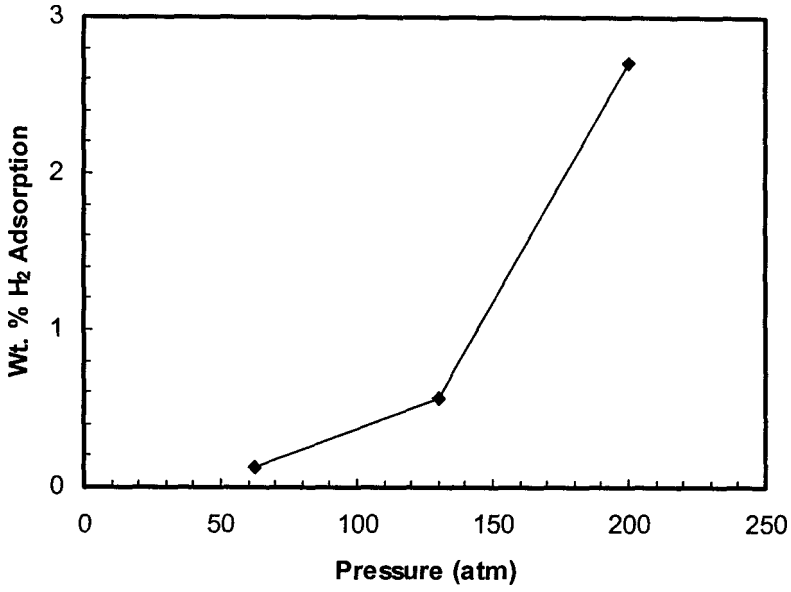

Figure 4-6. Preliminary result of high-pressure hydrogen adsorption on unpurified single-walled carbon nanotubes at 200K.

The isotherm shows an overall adsorption of 2.7 weight percent at a pressure of 200 atm and dry ice temperature (200K). Nearly 80 % of the total uptake occurred at a pressure higher than 130 atm, suggesting that some change in the mechanism of adsorption, or morphology of the sample may have occurred beyond this pressure.

The majority of adsorption most likely occurred on external sites on the carbon nanotubes because no attempt was made to remove the ends, or otherwise damage the nanotubes to allow a path to the interior either through chemical processing, or sonication, as done by other researchers [Pradhan et al., 2001; Ye et al, 1999]. The results are consistent with the possibility set forth by Ye et al.,

that above a certain pressure, the hydrogen gas has sufficient chemical potential to penetrate the bundles, overcome the cohesive force between the nanotubes and lead to separation of the bundles [Ye et al., 1999]. This change in structure would expose more surface area available to adsorption or potentially create channels of dimension suitable for enhanced adsorption between the individual tubes. In either case, expected isotherm profile would be similar to that observed in Figure 4-6. The explanation is consistent to both the present observation, and the earlier work by Ye et al., as shown when the two isotherms are plotted together in Figure 4-7.

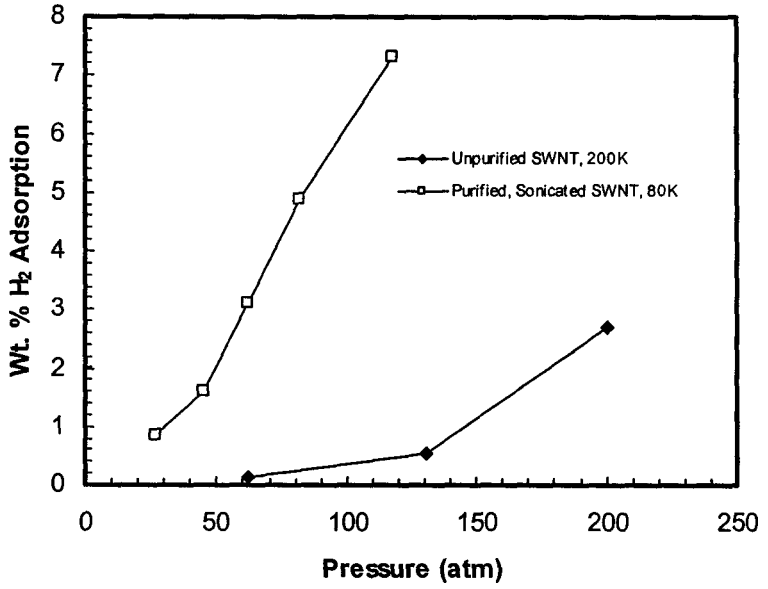

Figure 4-7. Comparison of the preliminary hydrogen adsorption isotherm on unpurified SWNT at 200 K with purified and sonicated SWNT at 80K [Ye et al., 1999].

To investigate the reports of Dillon et al., that the hydrogen adsorption of nanotubes may be increased by the presence of transition metals [Dillon et al., 2000], vanadium was deposited on the unpurified Carbolex nanotubes. Vanadium was deposited using RF bias sputtering (Randex, model 3140) in high purity argon. Deposition rate was monitored using an Inficon thickness monitor. Deposition was done in two stages separated by removal of the sample to atmosphere, physical agitation and repeated degassing. The morphology and composition of the modified samples was studied using SEM and high-resolution TEM in conjunction with EDX mapping.

Unfortunately, TEM revealed no information about the post-synthesis deposited vanadium suggesting that it is has not agglomerated and is atomically dispersed through the sample. This is further supported by a lack of EDX signal for vanadium by TEM as EDX is not highly surface sensitive. SEM, on the other hand, was able to detect a vanadium signal on some of the larger impurities present within the sample. The low magnification EDX element maps in Figure 4-8 contain a large amount of noise due to the high sensitivity required to detect the vanadium, but nevertheless reveal that vanadium is present. By inspection of the micrographs, the vanadium is not well dispersed throughout the sample, and localized regions of elevated concentration are indicated by arrows in Figure 4-8a. This finding was not unexpected, as sputtering deposits only on the surface of the top-most layer of the nanotubes that face the target.

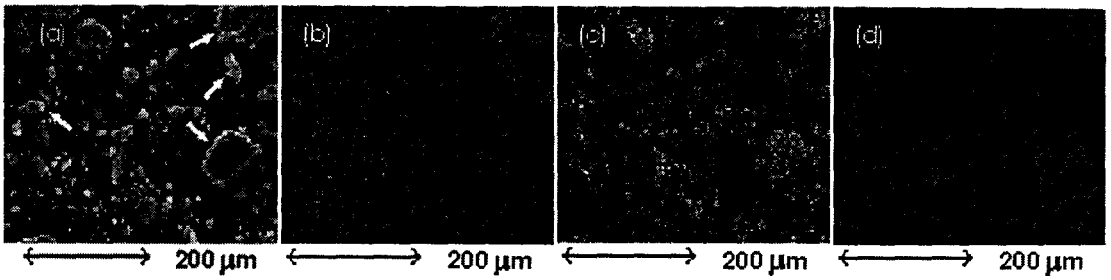

Figure 4-8. Low magnification EDX images showing local areas of high element concentration. (a) SEM image at 263x magnification; (b) through (d), element maps for the image in (a) of vanadium, nickel and yttrium, respectively.

The isotherm for the vanadium-modified sample is plotted in Figure 4-9 with the isotherm of the unmodified sample. At each pressure increment, these preliminary results indicate that the adsorption of the sample containing sputter-deposited vanadium exceeded that of the unpurified nanotube sample, reaching 3.9 weight percent at 200 atm. This observed increase may be due in part to partial removal of the amorphous carbon impurity from the surface of the nanotubes by ion bombardment that occurred as a result of the bias voltage applied to the substrate in the sputtering process.

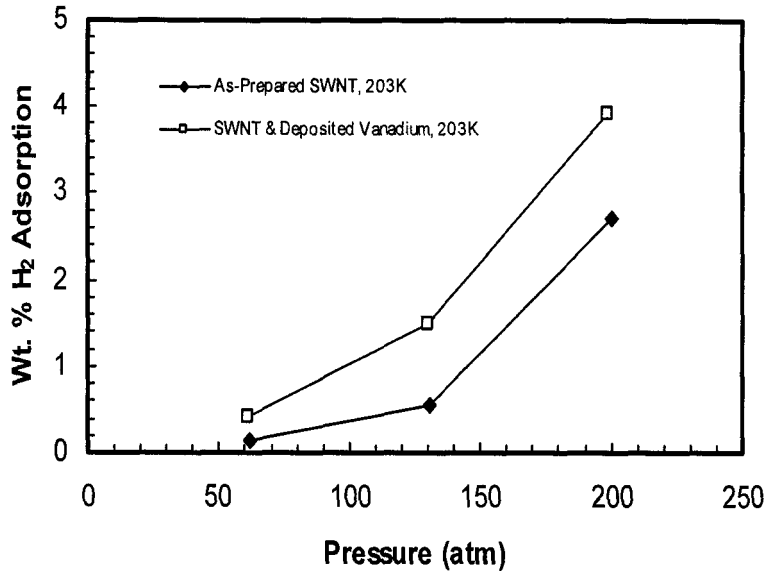

Figure 4-9. Wt. % hydrogen adsorption by unpurified SWNT, and SWNT with deposited vanadium at 200K.

The increased level of adsorption may also be due in part to a role played by the d-orbital electrons of the deposited vanadium in addition to that of the residual nickel and yttrium catalysts. Transition metals, including vanadium contain orbitals in the d-shell that are unfilled and as a result, these metals behave well as catalysts for dissociative chemisorption. It may be energetically favourable in this instance for dissociation of the hydrogen molecule to occur by each donating one electron to a d-orbital of the vanadium, and once dissociated, form a bond with the carbon. Vanadium would provide a larger contribution than the nickel in this regard considering the fine dispersion of the vanadium in comparison to the large nickel particles seen in Figure 4-5 as being upwards of 10 nm in diameter. Moreover, the nickel may require activation whereas the newly deposited vanadium does not.

An increase in adsorption due to the presence of vanadium is more pronounced at 130 atm than at 61 atm. Since before the vanadium was present, some morphology change was believed to occur above 130 atm, the increased adsorption at 130 atm suggests that the presence of the vanadium enables this transition to occur at a lower pressure. Between 130 atm and 200 atm, the isotherms of the two samples parallel each other, as is expected if in both cases, hydrogen adsorbs on newly exposed surface area. The increase at 200 atm, however, indicates that the vanadium may assist the transition to progress further towards completion than in the absence of vanadium. Alternatively, the increased adsorption at all pressures is expected if vanadium somehow assists in the adsorption of hydrogen itself.

Surface area and pore volume measurements taken before and after exposing the sample to high pressure hydrogen are tabulated in Table 4-2. Although an increase in the surface area of the sample after high pressure exposure is consistent with bundle separation, there is a decrease in the pore volume overall. This may suggest that some of the hydrogen did not completely desorb from the sample since the presence of residual hydrogen would shield the surface and prevent nitrogen from adsorbing. The results do indicate, however, that a larger proportion of the pore volume is composed of smaller pores, and a corresponding increase in surface area for micropores (<2 nm). Both observations are consistent with bundle separation. The large reduction in mesopore (>2 nm) surface area is unexpected and if the result of residual hydrogen, it is not clear

why hydrogen adsorbed on mesoporous surfaces would remain. The Kelvin equation (Equation 2.1) says that the vapour pressure of a fluid inside a small pore is lower than inside a larger pore. The expectation therefore is that if any hydrogen remains in the sample it would be adsorbed in the smaller micropores.

An alternative explanation for the decrease in mesopores is that a compressive force acts externally on the bundles. The compressive force may not affect the smaller micropores because the intermolecular repulsions at this range are too great for the force to overcome. On the other hand, there may be some flexibility in the tubes surrounding the mesopores, enabling an irreversible change. For example, a bundle containing a cluster of vacancies in the otherwise close-packed lattice would appear as a mesopore. The tubes surrounding the vacancy cluster would close together due to the external pressure, thereby eliminating the mesopore.

Sample	BET surface area (m^2/g)	Pore Volume (cm^3/g)	Micropore volume (cm^3/g)	Micropore surface area (m^2/g)	Mesopore surface area (m^2/g)
As-received	295.1	0.517	0.074	160.0	135.1
After testing	299.2	0.488	0.077	171.4	127.8

Table 4-2. Results of N_2 surface area and pore volume measurements on unpurified SWNT taken at 77K before and after exposing samples to high pressure.

The nitrogen adsorption isotherms at 77 K before and after testing are shown in Figure 4-10. The shape is consistent with Type II in the BET classification, and is virtually identical before and after.

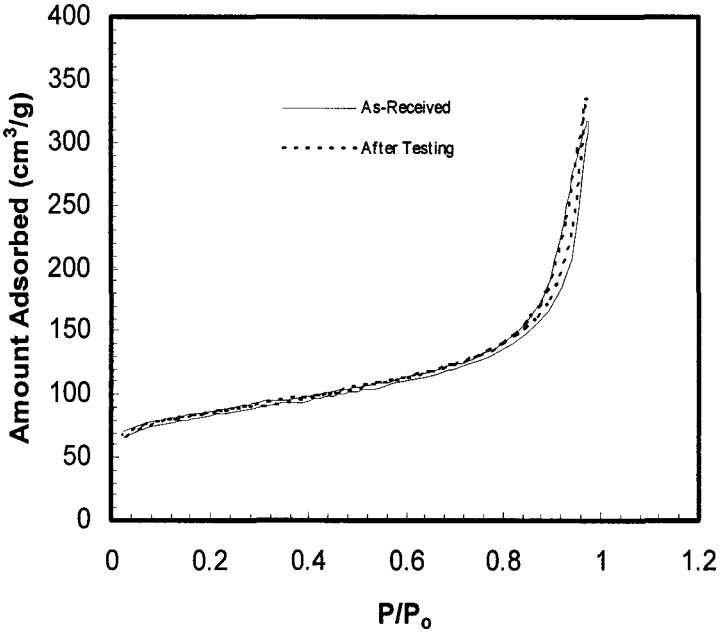

Figure 4-10. N_2 isotherms at 77 K before and after exposure of unpurified SWNT to high-pressure hydrogen.

In summary, a kink was observed in the high-pressure hydrogen adsorption isotherm on SWNT at 200 K. The kink may be due to a separation of the tubes within tube bundles to expose new surface area, as proposed previously by Ye et al. [Ye et al., 1999]. Irreversible changes in morphology of the sample are limited to an increase in the microporous surface area, and an unexplained drop in mesoporous surface area. The adsorption of SWNT in the presence of sputter-deposited vanadium is increased over the entire pressure range studied. The increase may occur because vanadium facilitates the opening of the tube bundles, or facilitates the adsorption of hydrogen.

Following this initial survey of adsorption properties of unpurified SWNT, the measurements were repeated. The experienced gained in the previous operation of the instrument resulted in the establishment of procedures and timing for consistent accumulation of data. The adsorption measurements were again obtained cumulatively, and taken at dry ice temperature with 12 hours of equilibration time allowed at each pressure. The same empty-cell calibration curves used in the preliminary study were used in this instance. Because the adsorption at each step is taken as the difference in pressure between the sample run and the calibration run, any unusual behaviour or inconsistencies present in the empty-cell calibration would be reflected in the outcome of the sample adsorption determination. This fact becomes significant in results reported in later sections.

The isotherm obtained in the repeated measurement is shown in Figure 4-11 along with the preliminary results. Note that for comparison purposes the isotherms of the preliminary results were recalculated using all of the steps listed in Section 3.1. Inclusion of the temperature transition above the dry ice bath instead of assuming the entire sample cell is immersed in the bath is the principle cause for the suppression of the isotherm to lower levels of adsorption.

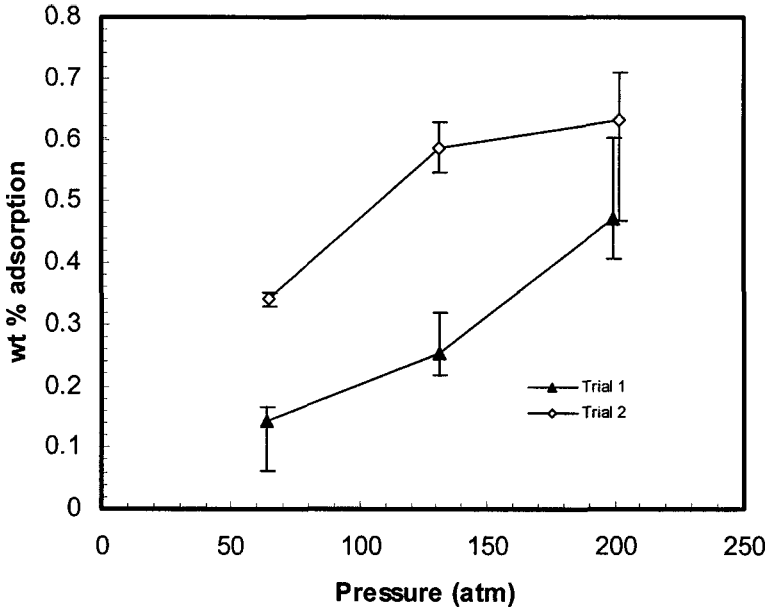

Figure 4-11. Additional trial and recalculation of hydrogen adsorption on unpurified SWNT.

The error bars shown in Figure 4-11 represent the uncertainty in the visual inspection step described in Section 3.1. The increasing size of the uncertainty with pressure reflects the fact that these measurements were cumulative. Therefore, the uncertainty of any given point is the summation of all previous points.

Although the recalculation of the initial trial preserves the kink in the isotherm, the new isotherm does not display a similar profile. The reason for this is not clear. It may be due to the packing of the sample within the sample cell. In the initial trial, the sample was loosely placed in the sample cell. In the subsequent trial, the sample was hand-packed into the sample cell using a metal

probe in an effort to test a larger mass of sample, thereby reducing the error of the measurement. Alternatively, the new isotherm may indicate that the kink found in the results of the preliminary work was erroneous. More careful and non-cumulative adsorption measurements are necessary to confirm or refute these observations.

4.2.1 Desorption of Unpurified SWNT

Desorption measurements were taken following the highest pressure step, by setting the reference cell to a pressure lower than the sample cell. When the sample cell valve is opened, the pressure equilibrates within the two volumes with the addition of any gas released by the sample at the new lower pressure. The desorption isotherm is shown in Figure 4-12. Again the vertical error bars reflect the uncertainty in the visual inspection of the calculated desorption. The considerable breadth of the uncertainty at lower pressures highlights the need to take isolated measurements, rather than cumulative ones.

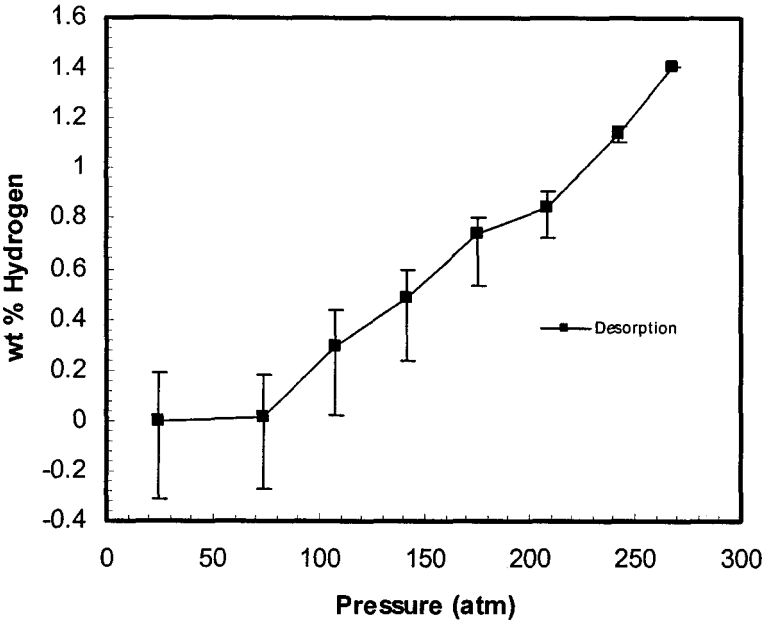

Figure 4-12. Desorption behaviour of unpurified SWNT from 265 atm at 200K.

The level of adsorption at 265 atm was arbitrarily selected to give nil adsorption at the lowest step. Ideally, the start point should be taken as that measured by adsorption. However, extrapolating the adsorption isotherm of trial 2 in Figure 4-11 forecasts a total adsorption of 0.727 % at 265 atm. Clearly, this is inconsistent with the desorption results in Figure 4-12, and suggests that more gas is released by the sample than stored. A similar discrepancy may have been experienced by researchers Ahn et al., and be the reason why only desorption data was reported in their publication [Ahn et al., 1998]. There are both advantages and disadvantages to taking desorption instead of adsorption as a measure of the true storage. For example, the presence of leaks can be mistaken for adsorption

events in adsorption, whereas in desorption it would have the opposite effect. On the other hand, some hysteresis is likely to be present, in which case desorption would not proceed to completion and heating and/or vacuum would be required to be release the remaining adsorbed hydrogen.

4.3 Investigations on Purified SWNT

Careful measurements of adsorption of hydrogen under high pressure were done on a sample of SWNT produced by a relatively new method referred to as High Pressure Carbon Monoxide or HiPco. This patented production method was developed by the Smalley group at Rice University and uses a gas phase catalytic reaction between carbon monoxide and an industrial gas at temperatures and pressures common in industrial chemical plants. Nanotubes produced by this method are relatively pure in the as-prepared state compared to other production methods.

A purified sample of HiPco SWNT were obtained from Carbon Nanotechnologies Inc. (Houston, Texas) and reported by the manufacturer to contain approximately 90 wt. % SWNT with the remainder being primarily residual catalyst. The TEM micrographs of the sample in Figure 4-13 are typical of the entire sample, and in contrast to the Carbolex nanotubes studied previously, show that these nanotubes are almost entirely free of graphite and other carbon species. EDX reveals that the residual metal in the sample is iron, and is dispersed throughout the sample as very regular particles having a diameter of 3

to 4 nm. As in the case of the SWNT studied previously, the CNI nanotubes are bundled, having 10-100 nanotubes per bundle. The ropes of bundled tubes appear to be continuous, branching and joining each other such that there is no clearly defined rope end.

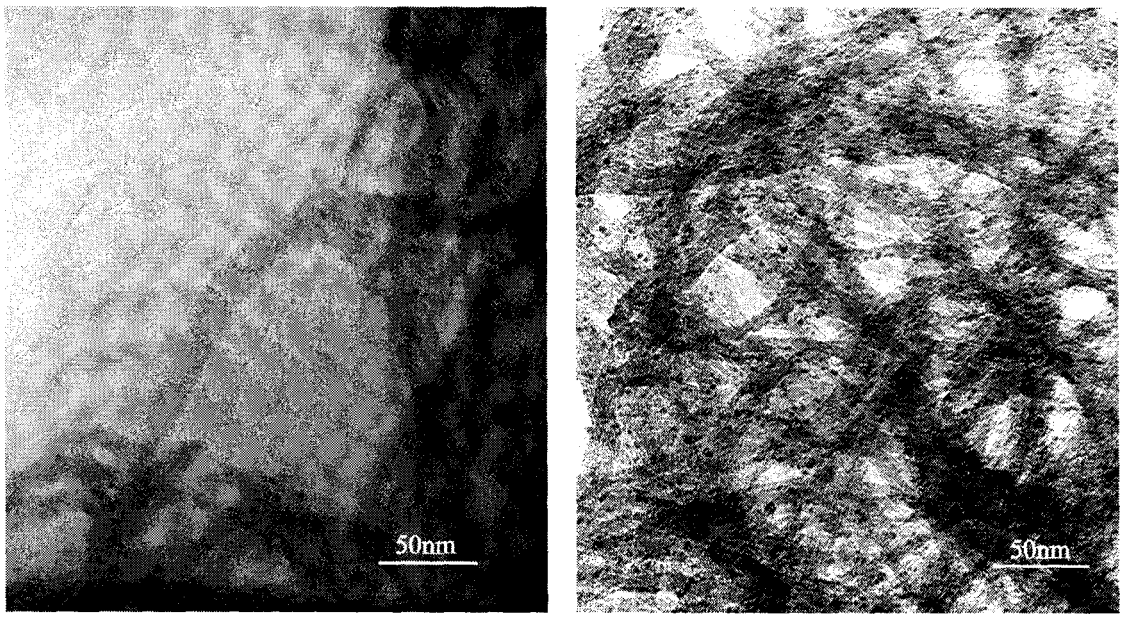

Figure 4-13. TEM micrographs of purified sample from CNI.

Adsorption measurements were carried out as described in Section 3.1 and are shown in Figure 4-14. The solid portion of the line connects measurements that were obtained after degassing the sample overnight. These data points were therefore taken non-cumulatively, in contrast to the measurements taken previously. However, because the maximum test pressure is limited by the volume ratio of the reference and sample cells, the highest pressure measurement,

indicated by a dashed line was cumulative. In other words, following the highest pressure isolated data point, the sample cell was sealed, and the reference cell was then filled to the highest pressure attainable. This new dose of gas was exposed to the sample cell and allowed to equilibrate to take the reading. The calculated adsorption from this step was then added to the previous. As a result, as in the case of the cumulative measurements taken in the previous section, the final data point has greater uncertainty than the isolated measurements.

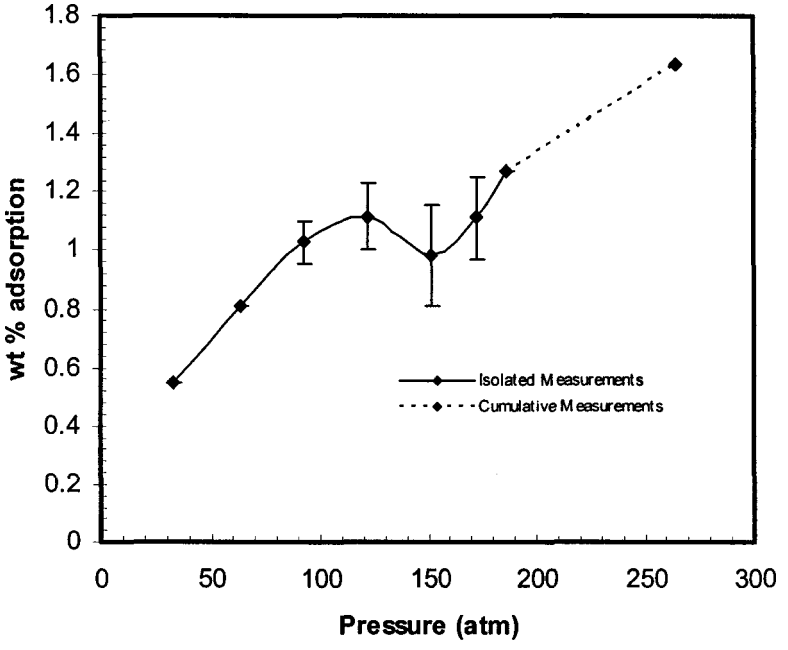

Figure 4-14. High-pressure hydrogen adsorption isotherm on purified SWNT at 200K. Vertical bars show spread of data when repeat measurements were taken, and the data points in these instances are average values.

Because the isolated data points were taken after degassing the sample under vacuum and heating for 12 hours, these data points could be repeated randomly. Data points surrounding the apparent negative slope on the isotherm in Figure 4-14 were repeated several times, and the vertical bars therefore depict the scatter in repeat measurements.

Depicted in Figure 4-15 is a plot of the apparent adsorption observed in the empty-cell calibration run. As mentioned in Section 3.1, it is possible to calculate the level of adsorption from the difference in mole number of a dose of gas of known pressure, volume and temperature before and after exposure to the sample. In contrast to calculating the difference in mole number between a sample run and an empty-cell run, this method is subject to systematic errors that vary with pressure and are consistent between repeat measurements. The apparent adsorption curve depicted in Figure 4-15 demonstrates some of this error. Clearly, it is not sensible to express this data as a weight percent adsorption since there is no sample. However, for the benefit of comparison, the apparent mass of hydrogen adsorbed was normalized by the mass of the sample in Figure 4-14.

Figure 4-16 provides a schematic example to clarify what is meant by "apparent empty-cell adsorption" and how it affects the measured adsorption. The figure shows pressure versus time for a typical experimental run. After setting the reference cell pressure and equilibrating for temperature fluctuation, the sample cell valve is opened, and the dose of gas is introduced to the sample

cell. If there is no sample, the mole number in the combined volume should be the same as in the reference cell volume, assuming negligible adsorption on the walls of the instrument. This mole number equates to the theoretical pressure shown in the figure. However, due for the most part to leaks, the actual pressure of the empty cell is consistently below this calculated theoretical pressure. The "sample pressure" shown in Figure 4-16 is the final pressure of the combined volumes when a sample is present. It is lower than the empty-cell pressure because some of the gas is adsorbed by the sample.

As can be seen from the shape of Figure 4-15, some of the "dip" in the isotherm of Figure 4-14 may be due to the "bump" in the calibration curve, since each point in the former is the result of subtracting the corresponding point in the latter. Note that although it may be tempting to correct the isotherm of Figure 4-14 by adding the "apparent adsorption" of the empty cell, to do so is erroneous because the leaks that led to this apparent adsorption also occur when the sample is present. If the apparent adsorption is indeed due to leaks, it is expected that it would increase monotonically with pressure. The "bump" therefore is likely the result of some unaccounted experimental inconsistency.

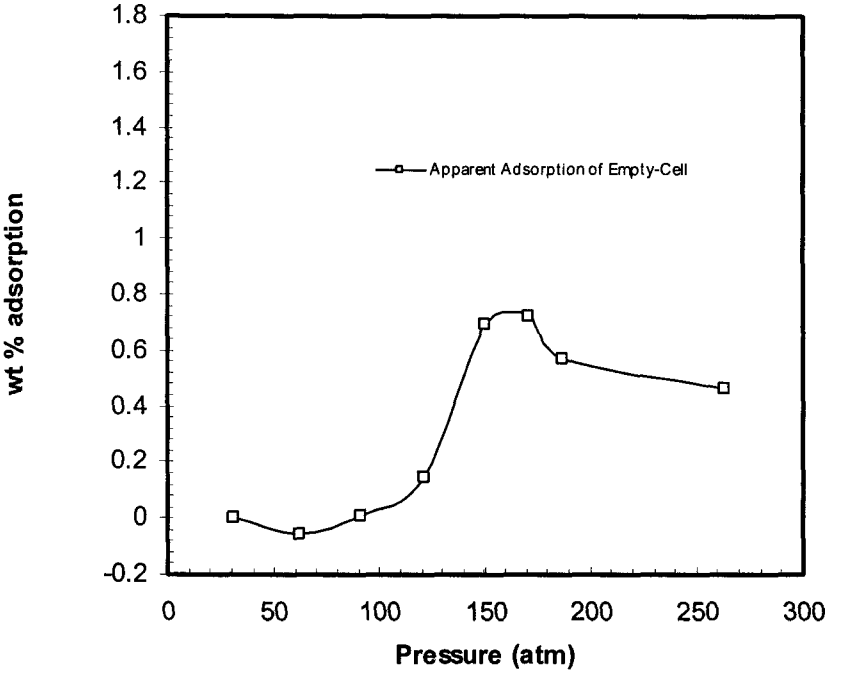

Figure 4-15. Apparent adsorption of empty sample cell at 200 K.

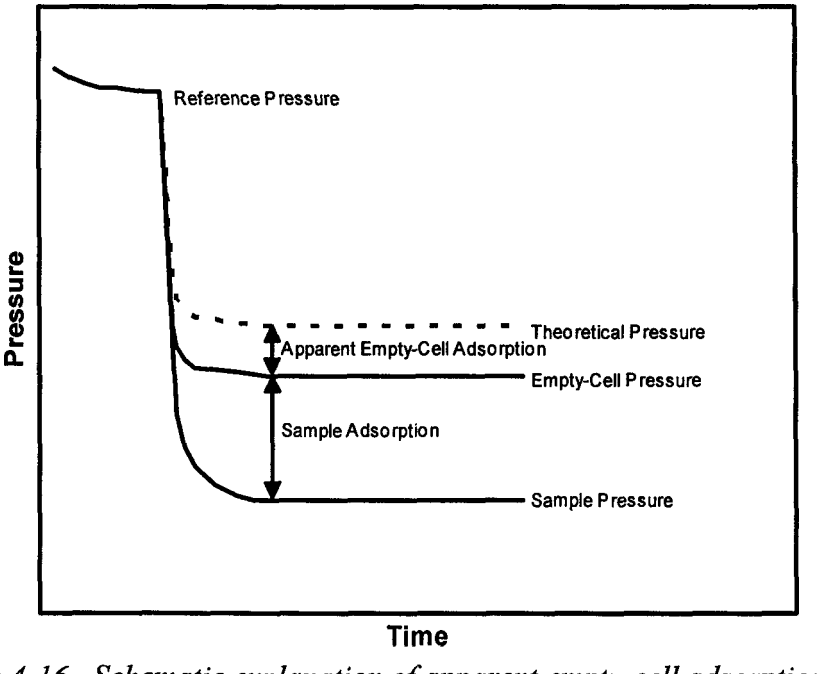

Figure 4-16. Schematic explanation of apparent empty-cell adsorption.

Following the adsorption measurement at 264 atm and 200 K, the instrument was vented, and the sample removed. Along with an as-received sample, the purified SWNT were studied using BET surface area and pore structure to identify any irreversible effects of high pressure on the sample morphology.

Sample	BET surface area (m^2/g)	Pore Volume (cm^3/g)	Micropore volume (cm^3/g)	Micropore surface area (m^2/g)	Mesopore surface area (m^2/g)
As-received	820.4	1.408	0.171	357.0	463.4
After testing	774.8	1.195	0.171	356.4	418.4

Table 4-3. Results of N_2 surface area and pore volume measurements on purified SWNT taken at 77K before and after exposing samples to high pressure.

In contrast to the unpurified sample studied previously, the purified SWNT sample experienced a significant decrease in overall surface area. However, as noted for the unpurified sample, there is also an unexplained decrease in the surface area of mesopores. Although there is again an increase in the proportion of the total pore volume that is made up of the micropores, the fact that the micropore volume remains unchanged suggests that this increase is not due to an increase in the number of micropores, which would be consistent with bundle separation. Instead, it appears to be due to a decrease in the number of the larger mesopores, a fact confirmed by the large reduction in mesoporous surface area. It is not clear how the number of mesopores is decreasing, since as

previously noted, if the decrease is due to residual hydrogen, it is expected that the hydrogen would remain in micropores, rather than mesopores. It is possible that the decrease in mesopore volume occurs as a result of the compressive force of the hydrostatic pressure. The nitrogen adsorption isotherm at 77 K before and after exposure of the sample to high-pressure hydrogen is shown in Figure 4-17. The shape of the isotherm remains unchanged; however, the isotherm measured after testing is shifted to a slightly higher level of adsorption.

Compared to the N_2 isotherm for the unpurified sample, depicted in Figure 4-10, there is a much higher level of adsorption on the purified sample, largely due to the higher surface area relative to the unpurified sample. In addition, there is a slightly larger hysteresis on the purified sample. This suggests that the purified sample contains a greater number of surface structures capable of trapping or condensing adsorbed molecules. This is expected, since unpurified sample contains amorphous carbon and other impurities that block adsorbing gases from accessing the nanotube bundles where these surface features likely exist. It is also possible that during the purification process, some of the nanotubes were damaged, exposing the interiors to adsorbing gases.

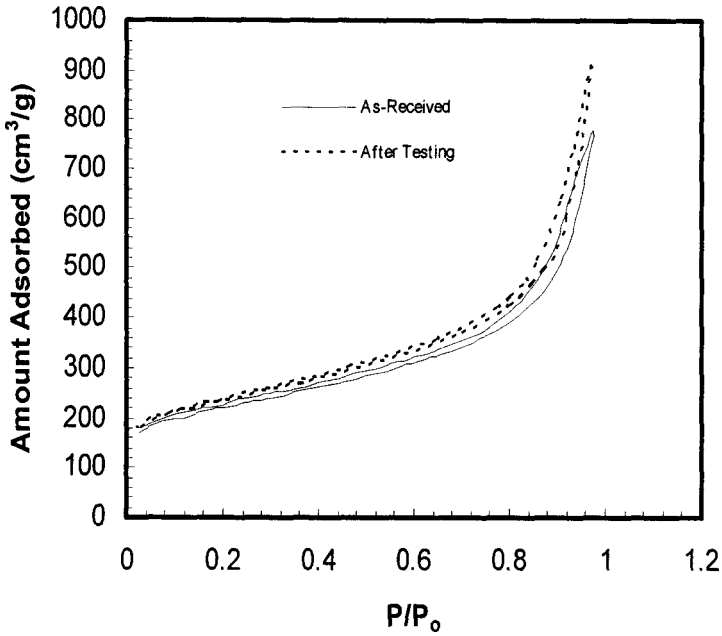

Figure 4-17. N_2 isotherms at 77 K before and after exposure of purified SWNT to high-pressure hydrogen.

To test whether hydrogen remains adsorbed onto the sample, the purified sample was tested three times to a pressure of 92 atm after different conditioning procedures. Prior to the initial test, the sample was degassed under low vacuum and 523 K for 12 hours. Prior to the second test, the sample was degassed under high vacuum, without heating, and prior to the third test, the sample was degassed under high vacuum, and 523 K. The results of the three tests are shown in Table 4-4.

Test Number	Sample Conditioning	Adsorption at 92 atm (wt. %)
1	Low Vacuum (10^{-3} Torr), 523 K	1.1
2	High Vacuum (10^{-5} Torr), 294 K	0.84
3	High Vacuum (10^{-5} Torr), 523 K	0.96

Table 4-4. Adsorption of purified SWNT at 200 K and 92 atm after different conditioning pre-treatments.

This experiment indicates that there is probably some adsorbed hydrogen remaining on the sample after degassing. The first test, following degassing under low vacuum, and 523 K gave the highest adsorption. Subsequently, the sample was exposed to high vacuum at room temperature- a treatment that appears to be ineffective at degassing the sample. The final test, using high vacuum, and heat treatment to 523 K was more effective at degassing the sample, but failed to return the sample to the condition prior to testing.

4.3.1 Desorption of Purified SWNT

Desorption measurements were also done on the purified sample. To be consistent with adsorption, these measurements were isolated, rather than cumulative. Instead of degassing the sample for 12 hours following each measurement, the sample cell was returned to a pressure of 238 atm (3500 psi) for 12 hours following each measurement. The results of desorption from the purified sample at 200 K are depicted in Figure 4-18. In this instance, the zero point was arbitrarily set such that the point of greatest desorption results in complete degassing of the sample. It is more probable, however, that some hydrogen will remain on the sample.

The desorption curve shows an unusual bump at a pressure slightly lower than the dip that was observed on the adsorption curve. However, in contrast to the previous finding, the apparent desorption of the empty-cell does not have a

corresponding feature at this pressure, as shown in Figure 4-19. The apparent empty-cell desorption is comparatively low in this case. As a result, the error in the measured sample adsorption from this source is probably overshadowed by errors introduced in correcting the transition zone temperature above the dry ice bath. (See Figure 3-6).

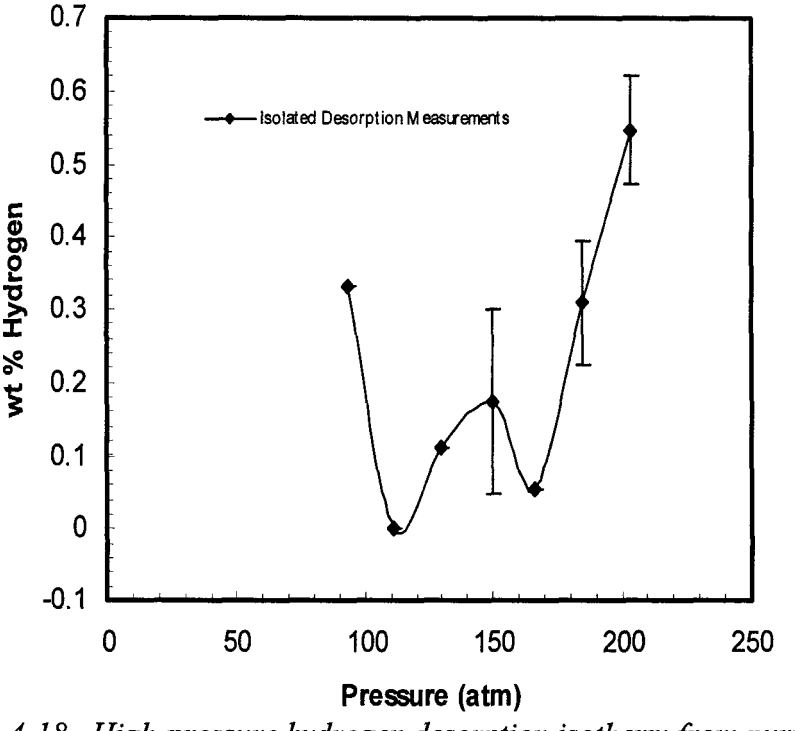

Figure 4-18. High-pressure hydrogen desorption isotherm from purified SWNT. Isolated data points were obtained by one-step pressure measurements following equilibration at 238 atm. Vertical bars show spread of data when repeat measurements were taken, and the data points in these instances are average values.

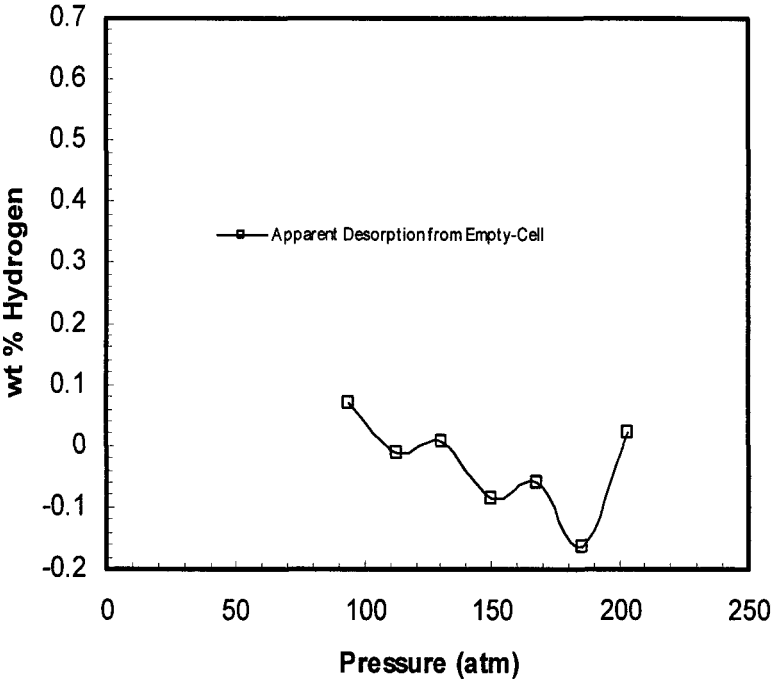

Figure 4-19. Apparent desorption of empty sample cell at 200 K.

The desorption curve also indicates that a larger amount of adsorbed gas remains on the sample when the pressure is reduced to 93 atm than remains when it is reduced by a smaller amount. As the apparent desorption curve of Figure 4-19 indicates a somewhat monotonic relationship with pressure below 200 atm, this unusual behaviour can not be easily attributed to instrumental effects. Without further confirmation, it is not possible to accept this observation, nor eliminate it as an isolated event.

4.3.2 Room Temperature Adsorption on SWNT

Adsorption measurements on the purified SWNT from CNI at room temperature give the isotherm in Figure 4-20, and desorption measurements give that in Figure 4-21.

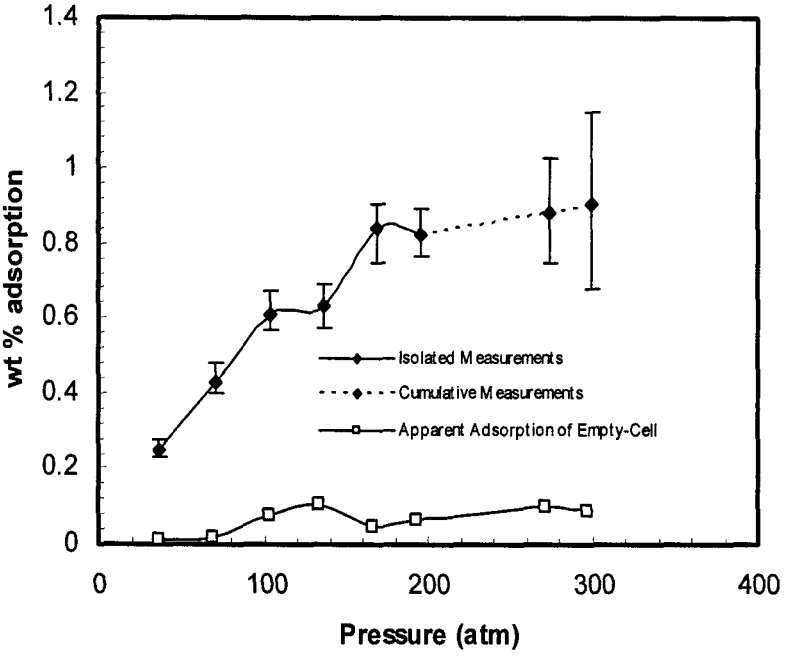

Figure 4-20. High-pressure hydrogen adsorption isotherm on purified SWNT at 294K. Vertical bars show the uncertainty in the visual inspection step at each data point. The lower curve is the apparent adsorption by the empty sample cell in the calibration run.

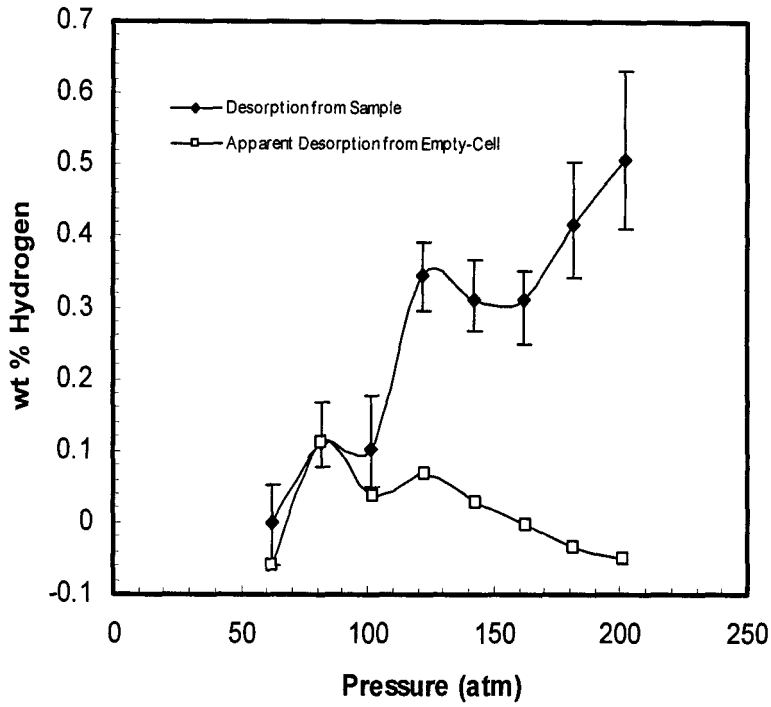

Figure 4-21. High-pressure hydrogen desorption isotherm from purified SWNT at 294 K. Data points were obtained by one-step pressure measurements following equilibration at 238 atm. Vertical bars show the uncertainty in the visual inspection step at each data point. The lower curve is the apparent desorption from the empty sample cell in the calibration run.

The room temperature isotherm on purified SWNT is particularly informative as it addresses one of the questions raised by Tibbetts et al. that a plateau of adsorption has not been observed for these materials [Tibbetts et al., 2001]. Figure 4-20 shows a plateau developing above 200 atm, which suggests the possibility that saturation of the sample at this temperature is being approached. It is not surprising that other researchers have not found this plateau, as it is at a pressure exceeding the experimental observations of previous works. The plateau is more clearly defined in Figure 4-22 where a smooth line is drawn

through the experimental findings and appears to be at a level of 0.91 wt. %. The isotherm is similar in shape, though lower in magnitude to that of Darkrim et al. on activated carbon, also shown in Figure 4-22 [Darkrim et al., 1999].

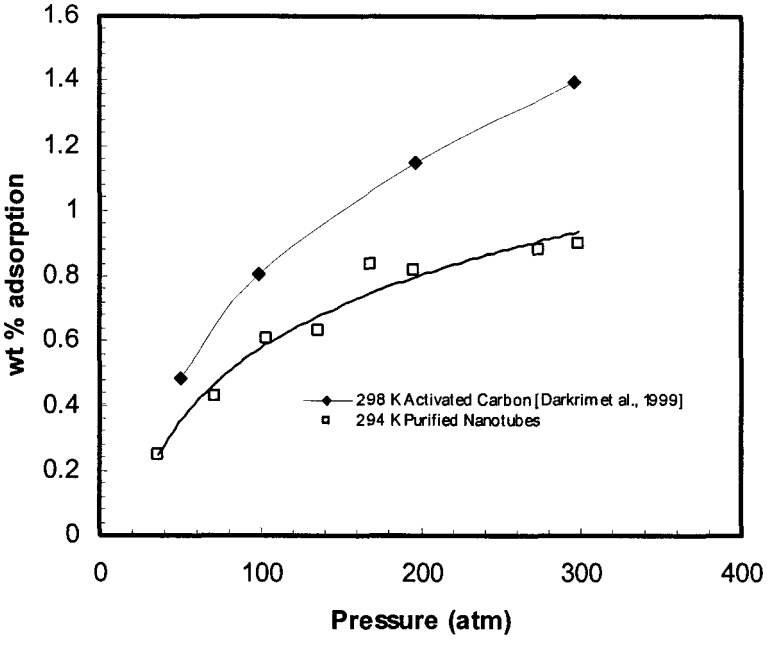

Figure 4-22. Adsorption isotherm on purified SWNT at 294 K compared to that of high surface area activated carbon [Darkrim et al., 1999].

The activated carbons studied by Darkrim et al. reportedly have a surface area of 2800 m^2/g, which is much larger than 800 m^2/g measured for the purified SWNT used in this study, and this difference may partially explain the higher adsorption observed in the previous work. The plateau on activated carbon found by this previous investigation corresponds to an adsorption of 1.5 wt. % or an adsorption to surface area ratio of 0.53 wt.%/1000 m^2/g. In contrast, the adsorption measured on SWNT in this study corresponds to 1.14 wt.%/1000 m^2/g

at room temperature, a value that compares well with the 1.5 wt.%/1000 m^2/g reported by Züttel et al. from electrochemical measurement [Züttel et al, 2002]. This finding indicates that the adsorption of hydrogen by SWNT bundles may differ somehow from adsorption by activated carbon. A possible explanation for this is that the unique convex surface of the nanotubes imparts some enhanced attraction to adsorbed molecules. This is not unreasonable if it is considered that within the small diameter of the nanotube, the electrons making up the pi bonds between adjacent carbons will have a tendency to repel each other. The net effect over the circumference of the nanotube would be to generate a slightly negative external cloud. This cloud would then interact with the permanent dipole of the adsorbing hydrogen species, enhancing adsorption. Although this would only affect the first adsorbed layer, beyond which the effect would be shielded, it may be sufficient to improve the fraction of monolayer coverage.

The observed adsorption capacity of nanotube bundles may be better understood with the assistance of a model, which is presented in the next section.

4.4 Model

The geometrical model of hydrogen adsorption on SWNT introduced in Section 2.2.1.1 assumed that the packing of hydrogen molecules in an adsorbed layer is similar to that of liquid hydrogen. Neutron scattering measurements of hydrogen adsorbed on graphite have suggested that the structure of the adsorbed layer is more complex than assumed by this simple model [Nielsen et al., 1979].

At low levels of coverage, the adsorbed molecules tend to prefer sites above the center of the hexagonal ring of carbon atoms, as opposed to sites directly above carbon atoms. In addition, at low levels of coverage, the molecules tend to spread out over the surface, foregoing adjacent carbon rings to accommodate the large kinetic diameter of 2.4 Å. They instead adopt the commensurate $\sqrt{3} \times \sqrt{3}$ structure shown in Figure 4-23a, having a hydrogen to carbon atom ratio of 1:3, or 2.8 wt. %. At higher levels of coverage, the denser incommensurate structure shown in Figure 4-23b is preferred. If the equivalent diameter of the hydrogen molecules in the latter structure is assumed to be similar to that in liquid hydrogen, then a monolayer of the incommensurate adsorbed structure gives 4.8 wt. % storage, as noted previously.

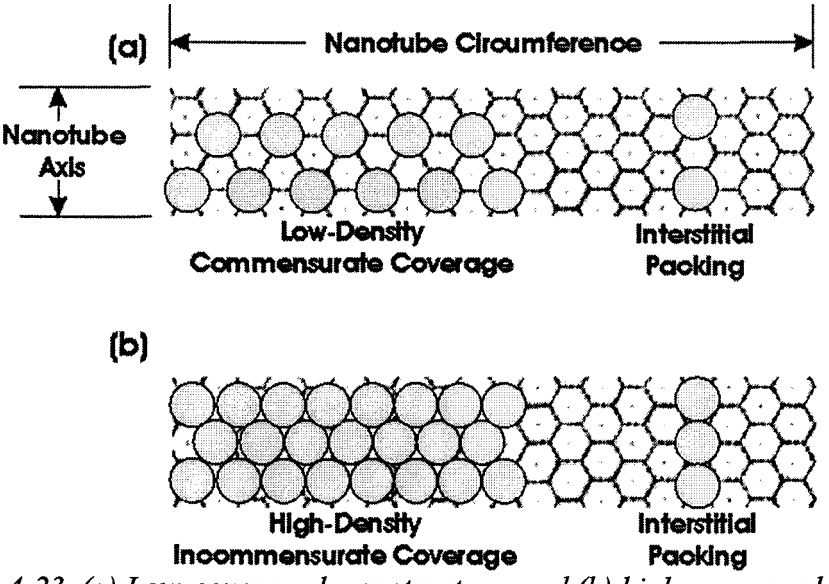

Figure 4-23. (a) Low-coverage layer structure, and (b) high-coverage layer structure.

As illustrated by Figure 2-7, when nanotubes assemble into close-packed bundles, the interstitial channels formed may be similar to the interior of the nanotubes in the sense that the potential of adjacent walls may overlap, leading to increased adsorption in this region. For the typical nanotube diameter of 13.8 Å, the lattice of the close-packed bundle is estimated at 17.2 Å. As a result, the interstitial space between the tubes is only able to accommodate one hydrogen molecule. Furthermore, the bundling of the nanotubes significantly reduces the surface area available for adsorption.

Figure 4-24 is an idealized scale drawing of bundled nanotubes with physisorbed hydrogen. Although it is possible for hydrogen molecules to fit within the interstitial of the bundle, it is not probable that it will fill to completion given that the tight spacing of the tubes requires access only from the bundle end. The extreme length of nanotube bundles then will limit the extent to which hydrogen will be able to diffuse through the channels. As mentioned previously, researchers have suggested that it may be possible for tubes to separate from one another under the influence of high pressure gas, the effect of which is to allow access of adsorbing gases within the bundle, thereby increasing the level of adsorption [Ye et al., 1999]. For this to occur, however, gas must be able to initially penetrate the bundle. Furthermore, because the bundles are very long and twisted, the separation of the tubes would require strain energy in excess of the cohesive force of the bundle. For separation to occur, the bundle would have to untwist, or the nanotubes would have to stretch or shear along the length. A

processing step aimed at shortening the length of the bundles may be beneficial in this regard.

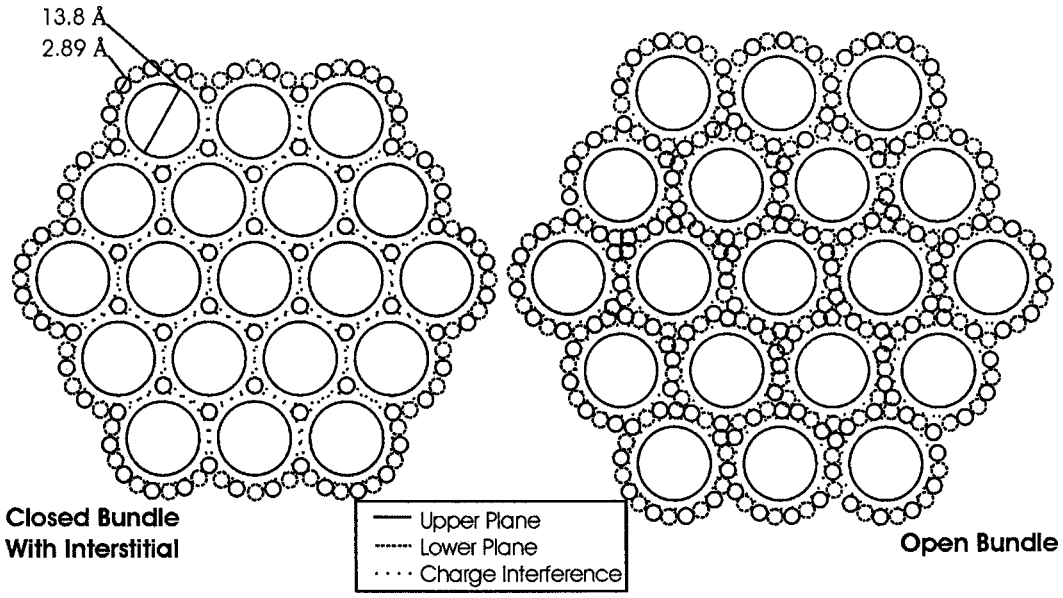

Figure 4-24. Scaled drawing of hydrogen adsorption on open and closed bundles.

Estimates of the level of adsorption expected on bundles compared with the number of tubes can be made based on the scale drawing in Figure 4-24, by counting the number of adsorbed molecules. Initially, if the adsorbed layer is assumed to take on the commensurate $\sqrt{3} \times \sqrt{3}$ surface structure, then a unit length of tube would have the coverage shown in Figure 4-23a. Were interstitial adsorption to occur, and take on a similar structure, the adsorbed molecules would form a low density one-dimensional stack like that shown in Figure 4-23a. Figure 4-24 also shows a possible geometry of a bundle in which separation of the tubes

has occurred to allow a single layer of adsorbed species to form between them. The estimates of three possibilities including low coverage adsorption with and without interstitial adsorption, and with bundle separation are shown in Figure 4-25a.

Adsorption on a bundle when the incommensurate high-density surface structure forms can be estimated based on the exposed surface area and assuming a density similar to that of liquid hydrogen. In this case, the one-dimensional interstitial would also be more close packed and have the structure shown in Figure 4-23b. If the bundles were to separate in the manner assumed for the previous case, then the adsorption can be calculated based on the overall volume of the bundle, and the volume available to hydrogen. The result of this calculation is shown in Figure 4-25b.

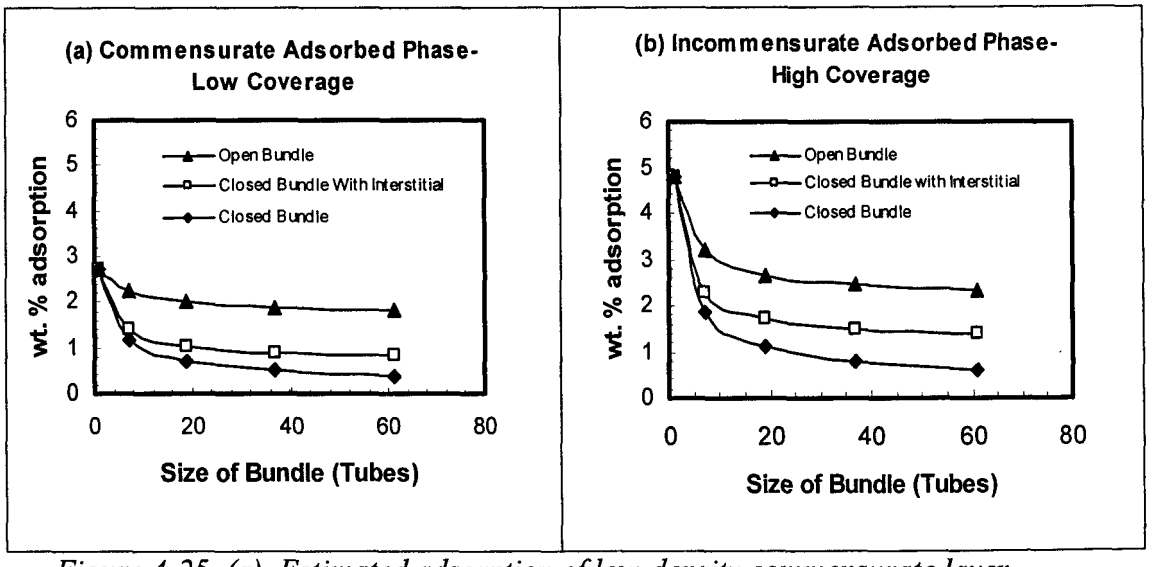

Figure 4-25. (a) Estimated adsorption of low-density commensurate layer, and (b) estimated adsorption of high-density commensurate layer.

An important consideration has been left out of this model, and also frequently in the literature [Lee and Lee, 2000] as noted by Simonyan and Johnson [Simonyan and Johnson, 2002]. The latter authors explained that the chemisorption model developed by Lee and Lee had neglected to consider that the volume taken up by the adsorbent reduces the usefulness of its presence at a given density of hydrogen, and this must be taken into consideration when calculating overall adsorption. Furthermore, Menon pointed out that the amount of adsorbing gas in the adsorbed surface layer takes up volume that otherwise would be filled with a given amount of pressurized gas [Menon, 1968]. This difference is typically referred to as excess adsorption as opposed to absolute adsorption. Note that experimental measurements consider the volume taken up by the sample, but generally neglect the volume taken by the adsorbed gas. An appropriate calculation of excess adsorption taking these considerations into account is [Rzepka et al., 1998],

$$wt\%(excess) = \frac{m_{H_2} - m^o_{H_2}}{m_C + (m_{H_2} - m^o_{H_2})} x100 \qquad 4.1$$

where m_{H_2} is the mass of hydrogen in the adsorbed surface layer, m_C is the mass of adsorbent, and $m^{\circ}_{H_2}$ is given by

$$m^o_{H_2} = \rho_{H_2}(V_C + V_{H,ads})$$

where ρ_{H2} is the density of hydrogen, V_C is the volume occupied by the adsorbent, and $V_{H,ads}$ is the volume of adsorbed surface layer. The excess adsorption therefore depends on pressure through the density and it is easy to observe that although the amount of gas adsorbed by a surface must reach a limit, the density will not. The density of gas increases with pressure, and consequently there must be some pressure beyond which the presence of the adsorbent is a detriment rather than a benefit. Gordon et al. referred to this as the breakeven pressure [Gordon and Saeger, 1999]. Likewise, as density increases with decreasing temperature, there must also be a breakeven temperature below which the presence of the adsorbent becomes a detriment.

The effect of considering hydrogen density on the previous calculations can be demonstrated by reconsidering the case for high-density incommensurate hydrogen structure on a closed bundle without interstitial adsorption. This case is selected since based on previous arguments, interstitial adsorption, and open bundles are improbable. Evaluating versus pressure at temperatures of 200 K and 298 K using interpolation of published data for hydrogen density [Woolley et al., 1948], upper limits for single layer adsorption on bundled nanotubes are plotted in Figure 4-26.

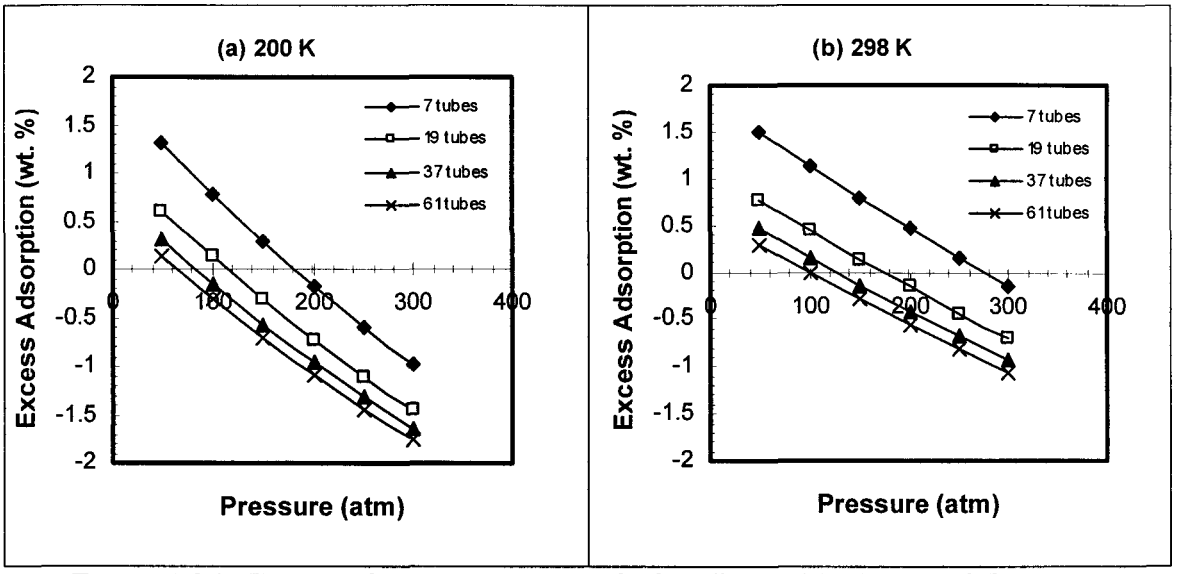

Figure 4-26. Excess adsorption on nanotube bundles at (a) 200 K and (b) 298K.

Figure 4-26 shows that the use of pressure is more effective at 298 K, than at 200 K because of the lower density of the gas at higher temperature. For a typical bundle size of 50 to 60 tubes, the breakeven pressure is approximately 60 atm at 200 K and 100 atm at 298 K. Consider then that if is not possible for bundles to separate, then above these breakeven pressures it is not possible to achieve a useful level of storage on bundled tubes even with a complete monolayer.

The model shows that for an average bundle size of 50-60 nanotubes that the purified sample contained, the expected adsorption capacity of closed bundles without interstitial is 0.38 wt. % and 0.61 wt. % for low density and high density coverage, respectively. An observed adsorption of 0.91 wt. % is inconsistent with this model, especially since a complete monolayer is unlikely to form at a

temperature far exceeding the triple point of hydrogen at 33 K. One possible explanation is that the bundles do not exist in the ideal geometry used to generate this model. Figure 4-27 is a micrograph taken at a bend in a nanotube bundle by Carbon Nanotechnologies Incorporated, the manufacturers of the purified SWNT used in this study. From the unique perspective shown it is clear that defects in the hexagonal lattice exist and that the bundle does not have a circular cross-section as assumed by the model. These features combined contribute to additional adsorption sites unaccounted for by the model and may explain the high adsorption observed.

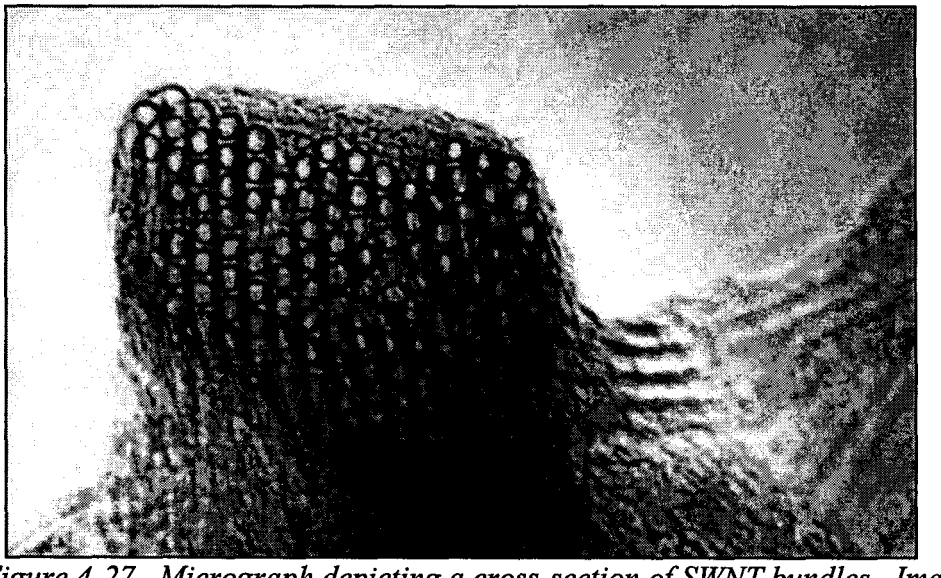

Figure 4-27. Micrograph depicting a cross-section of SWNT bundles. Image courtesy of CNI, no dimensions provided.

temperature far exceeding the triple point of hydrogen at 33 K. One possible explanation is that the bundles do not exist in the ideal geometry used to generate this model. Figure 4-27 is a micrograph taken at a bend in a nanotube bundle by Carbon Nanotechnologies Incorporated, the manufacturers of the purified SWNT used in this study. From the unique perspective shown it is clear that defects in the hexagonal lattice exist and that the bundle does not have a circular cross-section as assumed by the model. These features combined contribute to additional adsorption sites unaccounted for by the model and may explain the high adsorption observed.

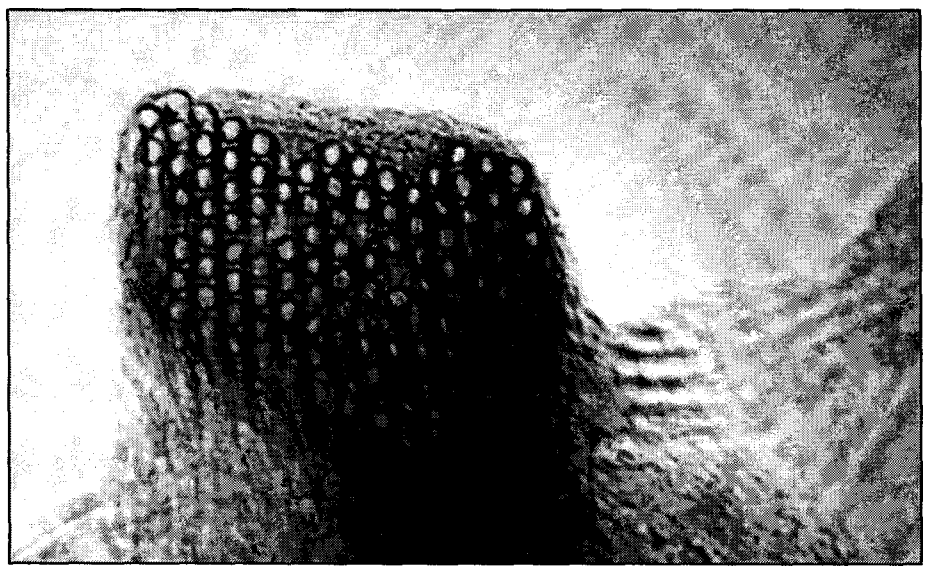

Figure 4-27. Micrograph depicting a cross-section of SWNT bundles. Image courtesy of CNI, no dimensions provided.

4.5 Additional Analysis

An interesting observation of the 200 K isotherm is the peak at 125 atm, followed by the valley at 150 atm, as shown in Figure 4-14. Because the volumetric adsorption instrument accounts for the volume taken up by the sample, a decrease in adsorption at higher pressure is unexpected and unusual. It is possible that the apparent fluctuation in the isotherm is the result of scatter in the experimental data, or as shown in Figure 4-15, due to an experimental inconsistency. However, there appears to be a similar feature, smaller in magnitude, at a slightly lower pressure at 294 K that is not easily accounted for by experimental inconsistency. The simplest explanation for a plateau or even a decline in adsorption with pressure is that the sample was not completely degassed between measurements. Therefore, available adsorption sites remained covered following lower pressure measurements. This explanation seems to be supported by the data in Table 4-4 that shows evidence of incomplete degassing. However, this explanation is ruled out by random repetition of selected pressure points, a procedure that was employed in measurement of the 200 K isotherm. Repeated measurements were not consistently lower than initial measurements despite using the same degassing procedure prior to each measurement.

Alternative explanations include a change in the morphology of the sample under the influence of high pressure, or a change in the interaction between the adsorbing gas and the sample with pressure. An example of the latter is if the gas chemisorbs above a certain pressure. Because the nanotube surface is

convex, if the adsorbed layer is farther from the surface, then the layer itself has a larger area than if it is held closely. A chemisorbed layer is predicted to be at a distance of 1.1 Å [Chan et al., 2001], whereas a physisorbed layer is expected to be at a distance of 3.4 Å [Dresselhaus et al., 2001]. A chemisorbed layer therefore has a smaller area than a physisorbed layer. Furthermore, chemisorption is likely to be site specific, since bonding electrons are required and are not evenly distributed over the surface. Considering these facts, if a chemisorption reaction is triggered by the pressure of the adsorbing gas, it is possible that the level of adsorption may decrease beyond a certain pressure. Evidence exists to the contrary, however, as if chemisorption occurs beyond a pressure of 125 atm, it is unlikely that the degassing method used would be effective in removing the chemisorbed species. Repeat measurements at pressures below the transition pressure, following measurements at higher pressure should indicate lower adsorption as the chemisorption sites are already filled. Table 4-5 lists the sequence in which measurements were taken to obtain the isotherm in Figure 4-14, and shows that a repeat measurement at a pressure of 122/123 atm following an excursion to higher pressures is actually higher than that measured previously. In addition, repeat measurement at a pressure of 151/152 atm indicates higher adsorption than previously. On the other hand, a repeat measurement at 92/93 atm does show lower adsorption. Therefore, the data does not unambiguously rule out the possibility of a physisorption to chemisorption transition as the source of the fluctuation in the isotherm. To do so would require *in situ* investigation of

parameters sensitive to carbon-hydrogen chemical bonds, including ultra-violet photoelectron spectroscopy (UPS), or Fourier transform infrared spectroscopy (FTIR). These and other techniques are difficult to achieve at high pressure because they require the sample to be visible from outside the system and were not attempted here.

Measurement Order	Pressure (atm)	Adsorption (wt. %)
1	33	0.55
2	63	0.81
3	93	1.1
4	123	1.0
5	151	0.81
6	175	1.25
7	92	0.956
8	122	1.23
9	152	0.915

Table 4-5. Sequence of randomly repeated measurements.

Another consequence of chemisorption is that there should be a large increase in the energy of adsorption above and below the transition pressure. This can be evaluated using the Langmuir model. From Section 2.1.3, the Langmuir isotherm behaves as Equation 2.8,

$$\theta = \frac{bP}{1+bP} \qquad 2.8$$

If the fractional coverage, θ is expressed as a ratio of the number of moles adsorbed, n to the number of moles comprising a monolayer of coverage, n_m, then Equation 2.8 can be rearranged to yield a straight line relationship with pressure,

$$\frac{p}{n} = \frac{1}{bn_m} + \frac{p}{n_m} \qquad 4.2$$

Figure 4-28 is a plot of P/n versus P, which has a slope of $1/n_m$ and an intercept of $1/bn_m$. We know from Section 2.1.3 that the variable b has an Arrhenius temperature dependence according to Equation 2.9. If the mechanism of adsorption were to change beyond a certain pressure, it is expected that the enthalpy of adsorption given by Equation 2.9 would also change. In turn, this would lead to a change in the slope of Figure 4-28. This is clearly not the case, as the slope above and below the suspected transition pressure at both temperatures is the same.

Solving Equation 2.9 for the activation energy yields a value of 1.9 kJ/mol. Bénard and Chahine calculated a value of 4.32 kJ/mol for hydrogen adsorption on activated carbons [Bénard and Chahine, 2001]. The lower value observed in this instance implies that hydrogen is more weakly held on the surface of SWNT bundles, and contradicts the explanation that the convex surface of the nanotubes produces a stronger attraction field for the hydrogen molecule.

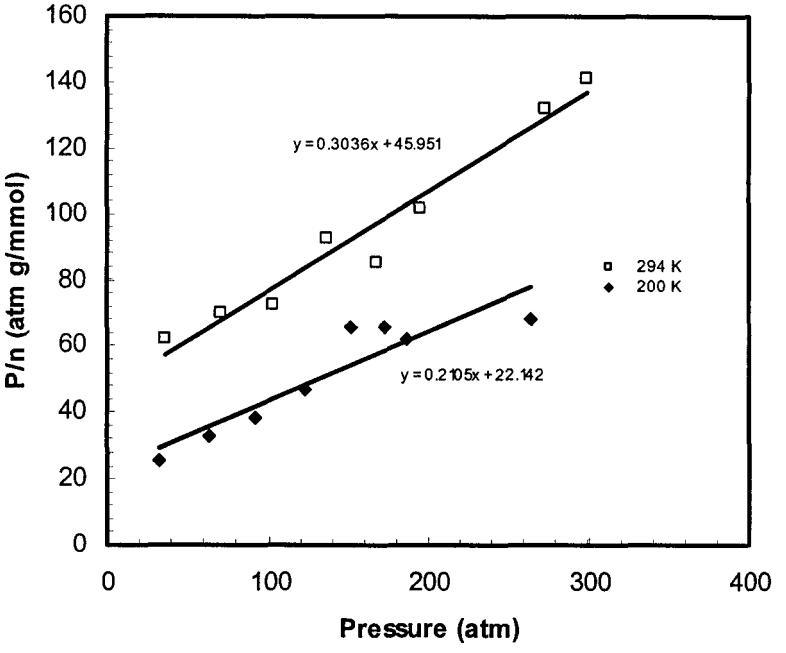

Figure 4-28. Langmuir model of adsorption on purified SWNT.

The isosteric heat of adsorption can be calculated using the Clausius-Clapeyron equation (Equation 2.10) from Figure 4-29. Figure 4-29 is a plot of the natural logarithm of the pressure with the inverse of temperature at different levels of adsorption. Unfortunately this equation can not be used to calculate the energy of adsorption in the proximity of the suspected transition pressure because there is no overlap of adsorption and it is therefore not possible to plot an isostere. Nevertheless, for lower pressures at which there is overlap, the slope of the lines in Figure 4-29 gives the heat of adsorption to be between 3.9 and 5.0 kJ/mol. In the absence of a change in morphology of the sample, the heat of adsorption at low levels of coverage is expected to represent the upper limit since as coverage

approaches saturation, adsorbate-adsorbate repulsions will result in weaker adsorption.

The low values of the heat of adsorption are indicative of very weak physisorption, and contradict the findings of Dillon et al. who measured heat of adsorption as high as 19.6 kJ/mol on SWNT [Dillon et al., 1997] and Pradhan et al. who measured 12.1 kJ/mol on SWNT [Pradhan et al., 2001]. On the other hand, the value compares quite well with a number of other studies including Johansson et al., who observed a heat of adsorption of 4.2 kJ/mol on short multiwall nanotubes (nanobarrels) [Johansson et al., 2002], and Bénard and Chahine who observed 4-6 kJ/mol for the isosteric heat of adsorption on activated carbon [Bénard and Chahine, 2001]. In addition, the value obtained here agrees well with an early report of heat of adsorption of hydrogen on planar graphite of 4 kJ/mol [Pace and Siebert, 1959].

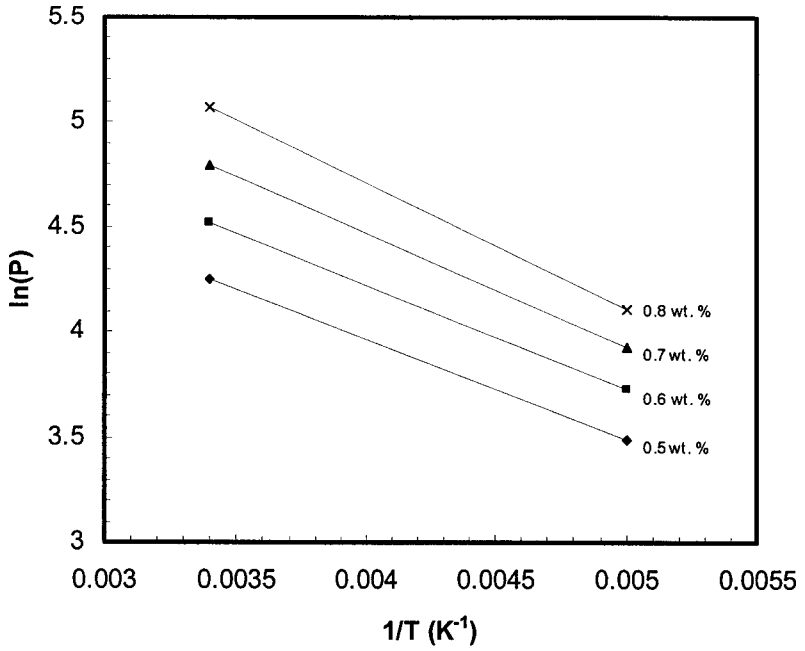

Figure 4-29. Adsorption isosteres on purified SWNT.

Another possible explanation for the unusual fluctuation in the two isotherms of the purified sample is that the sample undergoes some structural change to allow more or less adsorption. As mentioned in Section 2.2.2.1, changes in the morphology of the sample are not previously unreported and have been observed under a number of circumstances. In this instance, an intermediate plateau would be possible if saturation of available adsorption sites occurred at a pressure of 125 to 150 atm beyond which a sample transition occurred that produced additional sites. As mentioned previously, a proposal suggested by Ye et al. is that the energy of hydrogen at elevated pressure may be sufficient to overcome the cohesive energy of nanotube bundles and enable penetration of

adsorbing molecules into the interior of the bundles. As the model of the previous section shows, were a transition of this sort to occur to an extent sufficient for monolayer adsorption throughout the bundle, it could provide an increase in maximum monolayer adsorption of between 300 and 400%.

In the case of Ye et al., the nanotube bundles were sonicated in acid prior to being tested and as a result may have been cut or otherwise altered to enable the hydrogen to penetrate the bundle. In the present study, however, the samples were not modified, and the purified sample contains bundles that are very long in length, as shown in Figure 4-13. Therefore a plausible scenario in the present case is that hydrogen is unable to penetrate the very tight spacing of the nanotube bundles, shown to scale in Figure 4-24. Instead the pressure acts only on the outside of the bundles, compressing them, and thereby making it increasingly difficult for separation to occur. The possibility of morphological changes is further addressed in the following section.

4.6 *In Situ* Resistance Measurements at High Pressure

A novel experiment was devised to test for a change in morphology of the sample. A bulk of sample was found to be conductive with a measurable resistance. It was reasoned that if the bundles making up the sample were to separate the resistance of bundles parallel to the conduction path would not change because the overall area of conductor would remain the same. On the other hand, bundles oriented perpendicular would increase the resistance if they

were to open. Overall, the combined resistance of a bulk sample composed of a mixture of bundles of various orientations should increase significantly with pressure.

The measured resistance of the sample was found to be sensitive to minor changes in room temperature at a rate of -0.4 Ω/K. This increase in conductivity with temperature indicates that some of the nanotubes in the sample may be semiconducting. Nanotubes are known to be semiconducting or metallic depending on the orientation of the carbons relative to a single graphite plane. In reference to the various orientations shown in Figure 1-5, nanotubes having a zigzag orientation are typically found to be 2/3 metallic, and 1/3 semiconducting. Armchair nanotubes, on the other hand, and nanotubes oriented at an angle to the graphite plane are found to be 1/3 metallic, and 2/3 semiconducting [Collins and Avouris, 2000]. The orientations of the nanotubes are randomly distributed, and therefore the sample of purified nanotubes used in this study is likely a mixture of semiconducting and metallic nanotubes.

The resistance of purified SWNT was measured at different hydrogen pressures by enclosing electrodes within a modified sample cell, as discussed in Section 3.3. Following 12 hour degassing of the sample at a temperature of 353 K, and high vacuum, the sample was pressurized to 170 atm. The sample was held at this pressure to equilibrate, after which the measured resistance was found to be 13.289 ± 0.001 ohms. The pressure was then decreased by 17 atm steps

until vacuum was reached. At each step the pressure was held for 3 hours to allow the resistance to stabilize. The results of this test are shown in Figure 4-30.

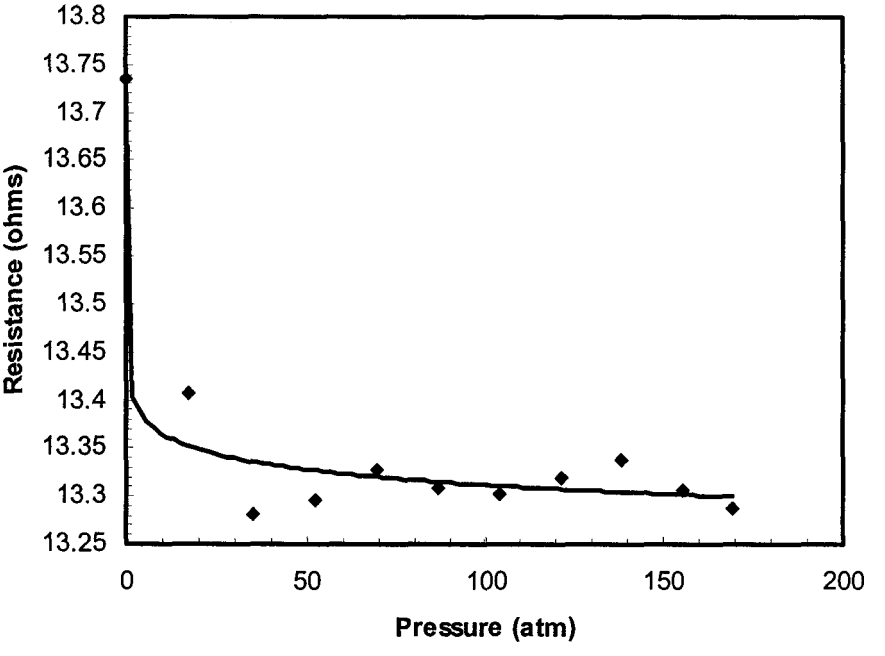

Figure 4-30. The resistance of SWNT at various hydrogen pressures.

The resistance of the sample at various pressures, shown in Figure 4-30 has been adjusted to account for minor changes in room temperature and therefore isolate the dependence on pressure. Although a small fluctuation does occur at a pressure between 125 and 150 atm, another occurs at 70 atm, and again at lower pressures. The fluctuation at 140 atm has a magnitude of only 0.25%, and is not significant enough to be indicative of a change in sample morphology. Furthermore a resistance increase as a result of opening of the nanotube bundles,

would be maintained and possible even increase at higher pressures as more and more bundles open. This is not observed on the data shown in Figure 4-30.

While it fails to reveal any opening of the nanotube bundles as a result of high pressure, the resistance data of Figure 4-30 provides for an alternative possibility. As the pressure is reduced from 35 atm to vacuum, there is a large increase in the resistance which is consistent with a decrease in the packing density of the SWNT. This result therefore supports the previous supposition that the bundles may actually be compressed as a result of the high pressure. If the hydrogen molecules are unable to penetrate the bundles initially, then the gas pressure will act only on the outside of the bundles, causing them to be compressed.

5.0 Conclusions

To resolve the controversy over hydrogen storage of SWNT bundles, a new volumetric adsorption measurement instrument was designed and constructed. It is capable of measuring adsorption up to 300 atm, and over a broad range of temperatures. An electrical probe within the sample cell of this system allows the *in situ* observation of sample morphology using resistance measurements.

The best hydrogen storage observed on bundles of SWNT was 1.6 wt. % at 264 atm and 200 K. At room temperature, the highest measured hydrogen storage was 0.9 wt. % at a pressure of 300 atm. While the room temperature isotherm appears to yield a plateau at a pressure above 160 atm, the 200 K isotherm appears to be incomplete, and higher adsorption may be possible at higher pressures. The room temperature adsorption on purified SWNT bundles equates to an adsorption to surface area ratio of 1.14 wt. %/1000 m^2/g which is intermediate between that of activated carbon and that of SWNT as measured by electrochemical means.

Contrary to the findings of Ye et al. [Ye et al., 1999], resistance measurements of purified SWNT bundles revealed that purified bundles of SWNT do not separate under high pressure. Instead, the bundles were found to compress

under the action of external pressure, leading to an increase in conductivity with pressure.

A model based on geometric considerations indicates that bundle separation would significantly improve the storage level were it possible. The model also reveals that because the nanotubes spacing within the bundle is so tight, adsorption within interstitial channels provides a negligible contribution if it occurs at all.

When the gas displaced by the sample volume is taken into consideration, the model indicates that a sample containing closed bundles is a detriment to the overall level of storage at high pressure. Above a breakeven pressure of 60 atm at 200 K or 100 atm at 298 K, a saturated monolayer is insufficient to recover the storage lost due to the volume taken up by the sample.

The isosteric heat of adsorption on SWNT bundles was found to be between 3.9 and 5.0 kJ/mol at low levels of adsorption, and the activation energy for adsorption determined by the Langmuir model was found to be 1.9 kJ/mol. This weak dependence of adsorption on temperature is indicative of physisorption. It implies that hydrogen is held to the external surface of SWNT bundles by an attraction similar to that of planar graphite and activated carbons.

Overall, without further modification the SWNT bundles examined in this study are insufficient hydrogen adsorbers to achieve the D.O.E. goal of 6.5 wt. % for an effective hydrogen storage system at reasonable conditions of pressure and temperature.

6.0 References

Ahn, C.C.; Ye, Y.; Ratnakumar, B.V.; Witham, C.; Bowman Jr., R.C.; Fultz, B., (1998), *Appl. Phys. Lett.*, **73**, 3378.

Bai, X.D.; Zhong, D.; Zhang, G.Y.; Ma, X.C.; Liu, S.; Wang, E.G.; Chen, Y.; Shaw, D.T., (2001), *Appl. Phys. Lett.*, **79**, 1552.

Bénard, P.; Chahine, R., (2001), *Langmuir*, **17**, 1950.

Bethune, D.S.; Kiang, C.H., (1993), *Nature*, **363**, 605.

Cao, A.; Zhu, H.; Zhang, X.; Li, X.; Ruan, D.; Xu, C.; Wei, B.; Liang, J.; Wu, D., (2001), *Chem. Phys. Lett.*, **342**, 510.

Chambers, A.; Park, C.; Baker, T.K.; Rodriguez, N.M., (1998), *Phys. Chem. B*, **102**, 4253.

Chan, S.P.; Chen, G.; Gong, X.G.; Liu, Z-F. (2001), *Phys. Rev. Lett.*, **87**, 205502.

Chen, Y.; Shaw, D.T.; Bai, X.D.; Wang, E.G.; Lund, C.; Lu, W.H.; Chung, D.D.L., (2001), *Appl. Phys. Lett.*, **78**, 2128.

Chen, P.; Wu, X.; Lin, J.; Tan, K.L., (1999), *Science*, **285**, 91.

Collins, P.G.; Avouris, P., (2000), "Nanotubes for Electronics", *Scientific American*, December 2000.

Darkrim, F.L.; Malbrunot, P.; Tartaglia, G.P., (2002), *Int. J. Hyd. Ener.*, **27**, 193.

Darkrim, F.; Vermesse, J.; Malbrunot, P.; Levesque, D., (1999), *J. Chem. Phys.*, **110**, 4020.

Dillon, A.C.; Jones, K.M.; Bekkedahl; T.A.; Kiang, C.H., Bethune, D.S., Heben M.J., (1997), *Nature*, **386**, 377.

Dillon, A.C.; Gennett, T.; Alleman, J.L.; Jones, K.M.; Parilla, P.A.; Heben, M.J., (2000), *Proceedings of the 2000 DOE/NREL Hydrogen Program Review*, May 2000.

Dresselhaus, M.S.; Williams, K.A.; Eklund, P.C., (1999), *MRS Bulletin*, November 1999, 46.

Gaskell, D.R. (1981), *Introduction to Metallurgical Thermodynamics, 2nd Ed.*, Hemisphere Publishing Corporation, New York.

Gregg, S.J.; Sing, K.S.W., (1982), *Adsorption, Surface Area and Porosity, 2nd Ed.*, Academic Press, New York.

Gordon, P.A.; Saeger, R.B., (1999) *Ind. Eng. Chem. Res.*, **38**, 4647.

Gu, C.; Gao, G-H.; Yu, Y-X.; Mao, Z-Q., (2001), *Int. J. Hyd. Ener.*, **26**, 691.

Hirscher, M.; Becher, M.; Haluska, M.; Dettlaff-Welikowska, Quintel, A.; Duesberg, G.S.; Choi, Y.-M.; Downes, P.; Hulman, M.; Roth, S.; Stepanek, I.; Bernier, P., (2001), *Appl. Phys. A*, **72**, 129.

Hwang, J.Y.; Lee, S.H.; Sim, K.S.; Kim, J.W., (2002), *Syn. Metals*, **126**, 81.

Iijima, S., (1991), *Nature*, **354**, 56.

Iijima, S.; Ichihasi, T., (1993), *Nature*, **363**, 603.

Jensen, C.M.; Zidan, R.; Mariels, N.; Hee, A.; Hagen, C., (1999), *Int. J. Hyd. Ener.*, **24**, 461.

Johansson, E.; Hjörvarsson, T.; Ekström, T.; Jacob, (2002), M.; *J. Alloys and Comp.*, **330-332**, 670.

Kiyobayashi, T.; Takeshita, H.T.; Tanaka, H.; Takeichi, N.; Züttel, A.; Schlapback, L.; Kuriyama, N., (2002), *J. Alloys and Comp.*, **330-332**, 666.

Krätschmer, W.; Lamb, L.D., Fostiropoulos, K.; Huffman, D.R., (1990), *Nature*, **347**, 354.

Kuznetsova, A.; Mawhimney, D.B.; Naumenko, V.; Yates Jr., J.T.; Liu, J.; Smalley, R.E., (2000), *Chem. Phys. Lett.*, **321**, 292.

Larminie, J.; Dicks, A., (2000), *Fuel Cell Systems Explained*, John Wiley and Sons, New York.

Lee, S.M.; An, K.H.; Kim, W.S.; Lee, Y.H.; Dark, Y.S.; Seifert, G.; Frauenheim, T., (2001), *Syn. Metals*, **121**, 1189.

Lee, S.M.; Lee, Y.H., (2000), *Appl. Phys. Lett.*, **76**, 2877.

Lueking, A.; Yang, R.T., (2002), *J. Catal.*, **206**, 165.

Liu, C.; Fan, Y.Y.; Liu, M.; Cong, H.T.; Cheng, H.M.; Dresselhaus, M.S., (1999), *Science*, **286**, 1127.

Malbrunot, P.; Vidal, D.; Vermesse, J.; Chahine, R.; Bose, T.K., (1997), *Langmuir*, **13**, 539.

Masel, R.I., (1996), *Principles of Adsorption and Reaction on Solid Surfaces*, John Wiley and Sons, New York.

Menon, P.G., (1968), *Chem. Rev.*, **68**, 277.

Nielsen, M.; McTague, J.P.; Passell, L. in *Phase Transitions in Surface Films*, edited by J.G. Dash and J. Ruvalds, Plenum Press, New York, 1979.

Nijkamp, M.G.; Raaymakers, J.E.M.J.; van Dillen, A.J.; de Jong, K.P., (2001), *Appl. Phys. A*, **72**, 619.

Pace, E.L.; Siebert, A.R., (1959), *J. Phys. Chem.*, **63**, 1398.

Pradhan, B.K.; Harutyunan, A.; Stojkovic, D.; Zhang, P.; Cole, M.W.; Crespi, V.; Goto, H.; Fujiwara, J.; Eklund, P.C., (2001), *Mater. Res. Soc. Symp. Proc.*; **706**, Z10.3.1.

Robens, E.; Czanderna, W.; Poulis, A., (1980), *Powder Metallurgy International*, **12**, 201.

Rzepka, M.; Lamp, P.; de la Casa-Lillo, M.A., (1998), *J. Phys. Chem. B*, **102**, 10894.

Smalley, R.E.; Colbert, D.T., (1995), Transcribed Address to the Robert A. Welch Foundation 39th Conference on Chemical Research: Nanophase Chemistry, Houston, TX, 1995.

Simonyan, V.V.; Johnson, J.K., (2002), *J. Alloys and Comp.*, **330-332**, 659.

Tibbetts, G.G.; Meisner, G.P.; Olk, C.H., (2001) *Carbon*, **39**, 2291.

Wang, Q; Johnson, J.K., (1999), *J. Phys. Chem. B*, **103**, 277.

Woolley, H.W.; Scott, R.B.; Brickwedde, F.G., (1948), *J. Research NBS*, **41**, 379.

Yang, F.H.; Yang, R.T., (2002) *Carbon*, **40**, 437.

Yang, R.T., (1999), *Carbon*, **38**, 623.

Zaluska, A.; Zaluski, L.; Strom-Olsen, J.O., (1999), *J. Alloys & Comp.*, **288**, 217.

Zandonella, C., (2001), *Nature*, **410**, 734.

Zhu, H.; Cao, A.; Li, X.; Xu, C.; Mao, Z.; Ruan, D.; Liang, J.; Wu, D., (2001), *Appl. Surf. Sci.*, **178**, 50.

Züttel, A.; Sudan, P.; Mauron, Ph.; Kiyobayashi, T.; Emmenegger, Ch.; Schlapbach, L., (2002), *Int. J. Hyd. Ener.*, **27**, 203.